École polytechnique de Louvain

Design of a large-scale experimental test of high-rise concrete wall reinforced with fiber reinforced polymers

Authors: **Mathilde Vandenberghe, Florie Tinant**
Supervisors: **João Saraiva Esteves Pacheco De Almeida, Ryan Hoult**
Readers: **Christophe Bayart, Catherine Doneux, Gabriele Balconi**
Academic year 2022–2023
Master [120] in Civil Engineering

Abstract

Reinforced concrete (RC) walls are employed in countless buildings, from mid-rise to high-rise. One of the major challenges in the field of construction nowadays is to make concrete usage more environmentally friendly and to extend the lifetime of buildings. One solution to these issues is the utilization of GFRP (Glass Fiber Reinforced Polymer) as reinforcement. However, despite its resistance to corrosion, this polymer is significantly underutilized in the industry. The lack of understanding of the seismic behavior of FRP is one of the main obstacles. Unlike steel, GFRP exhibits an elastic behavior and a lack of ductility, making it susceptible to brittle failure.

In the existing literature, experimental tests have mostly been conducted on rectangular walls. This study aims to advance knowledge on the subject by preparing an experimental test on an I-shaped wall reinforced with GFRP. The I-shaped wall was designed using various numerical models and following the next generation of Eurocode 2. The experimental setup has also been thoughtfully devised to preemptively address potential issues during the experiment's execution.

Acknowledgements

First and foremost, it is appropriate to express our sincere gratitude to everyone who has played a part, whether directly or indirectly, in the realization of this thesis.

Firstly, Prof. João Saraiva Esteves Pacheco De Almeida and Dr. Ryan Hoult deserve our gratitude for enabling us to work on this challenging project, even though it didn't lead us to the lab as we had hoped. It has been an incredibly enriching experience that taught us to adapt to new situations. We sincerely appreciate your availability and guidance, and we're grateful for your enthusiastic encouragement to consistently strive for excellence.

We would like to sincerely thank Christophe Bayart for sharing his expertise about the LEMSC, for answering quickly and completely all our questions about the experimental setup, and for helping in every step of the 3D modeling of the future experiment. What's more, we thank him as well as Catherine Doneux and Gabriele Balconi who generously agreed to be the readers for this thesis. We wish you an enjoyable reading experience.

We also extend our gratitude to all our fellow students who shared this journey with us. Your support, encouragement, and exchange of knowledge have been crucial in keeping us on track. Special thanks to Basile Payen, whose significant assistance greatly aided our understanding of the Seismostruct software. We'd also like to thank Louis Sartenaer and Mathieu Deridder, with whom we would have liked to share more of this experience.

Last but not least, we would like to thank our families, friends, and roommates for the support they have given us throughout this year and since the beginning of our studies. Thank you for reading this report over and over again until the end, and for showing an interest in a field that is so far removed from your own. Finally, thank you for cheering us up in times of doubt, your support has been invaluable.

Contents

List of abbreviations

ACI	American Concrete Institute
AFGC	Association Française de Génie Civil
AFRP	Aramid Fibre Reinforced Polymers
ALR	Axial Load Ratio
AR-glass	Alkali-Resistance glass
CFRP	Carbon Fibre Reinforced Polymers
CNR	Italian National Research Council
CSA	Canadian Standards Association
CTE	Coefficient of thermal expansion
DFOS	Distributed Fibre Optic Sensing
DIC	Digital Image Correlation
E-glass	Electrical glass
EC2	Eurocode 2
FIB	International Federation for Structural Concrete
FRP	Fiber Reinforced Polymers
GFRP	Glass Fiber Reinforced Polymers
JSCE	Japan Society of Civil Engineers
LEMSC	Laboratoire Essais Mécaniques, Structures et génie Civil
LVDTs	Linear Variable Differential Transformers

NAC	Natural Aggregate Concrete
PAN	Polyacrylonitrile
RC	Reinforced Concrete
S-glass	High-Strength glass
SLS	Serviceability Limit State
SMA	SubMiniature version A (connector)
SSC	Seawater Sea-sand concrete
Td	Decomposition temperature
Tg	Glass transition temperature
UV	Ultraviolet

Chapter 1

Introduction

1.1 Motivation

Reinforced concrete (RC) walls are employed in countless buildings, from mid-rise to high-rise. They are used all over the world, mainly to support lateral loads such as wind or seismic events. Conventional reinforced concrete shear walls have already proved their effectiveness in this context. However, the reinforced concrete (RC) sector is currently confronted with pressing challenges that must be addressed promptly in order to attain a future that is both more sustainable and resilient.

One of the problems is the high consumption of raw materials (such as sand or clay), which degrades the flora and fauna in these areas and, through its use, releases a significant amount of CO2. Furthermore, concrete's prolonged contact with aggressive substances like chlorides throughout its lifetime can lead to the corrosion of the reinforcing steel, resulting in a notable decrease in the longevity of reinforced concrete structures. This is further exacerbated by the use of road salt in winter.

To address the issues linked to deterioration caused by corrosion, some solutions exist, such as the use of corrosion inhibitors. Nowadays, the most effective method is the use of (Glass) Fibre-Reinforced Polymers, denoted GFRP as reinforcement instead of steel. In fact, GFRP bars are only slightly sensitive to chloride attack.

The use of FRP bars in different types of structures has already proved its applicability in many buildings thanks to its good performance. However, its installation is slowed down firstly by its high production cost, even though this is counterbalanced by its low maintenance cost compared with steel.

Another point of concern is the difference in behaviour between steel and FRP. Steel has an elastoplastic behaviour which allows it to deform significantly before breaking. This ductility is an advantage in the design because the deformation and the cracks created without too much loss of strength allow users to be warned about the state of the structure before it collapses. On the contrary, FRPs have linear elastic behaviour, which means there is no sign of failure. For the design of FRP-reinforced concrete structures, it will be seen that it is preferable to use an over-reinforced design to take advantage of the plastic behaviour of concrete before failure.

This behaviour of FRP-RC structures raises the question of the possibility that this type of structure could be present in regions where seismic events are highly prevalent. Unfortunately, this subject is still largely unstudied. Design codes and standards do not provide for seismic design and even do not recommend the use of FRP for now.

However, a new generation of Eurocode 2 will soon be published, which should include guidelines for the design of concrete walls (and other RC members) with FRP reinforcement. This publication is intended to broaden the use of FRP reinforcements and pave the way for new studies on the subject. It is along these lines that the present project is being conducted.

1.2 Objectives

This study aims to conduct an experimental test in order to improve the comprehension of the seismic behaviour of Glass Fiber Reinforced Polymer (GFRP) used as reinforcement within a wall. Existing literature has largely focused on walls with rectangular configurations. This research distinguishes itself from earlier literature through the choice of an I-shaped wall.

The main objectives of this thesis are as follows:

- To review various existing codes to develop an analytical design procedure for structures with Fiber Reinforced Polymer (FRP) reinforcements.
- To develop numerical models to predict the behaviour of FRP-reinforced concrete walls.
- To ensure the reliability of our numerical model and analytical procedure by testing them on various existing case studies.
- To design an I-shaped FRP-reinforced concrete shear wall using the upcoming generation of Eurocode 2, notably.
- To prepare the future experimental test of the I-shaped wall in the LEMSC by developing a loading protocol, a test setup and determining the instrumentation.

1.3 Thesis structure

This work is composed of 7 main parts :

- **Part 1 Introduction** aims to provide an explanation of the motivations, objectives and structure of the document.
- **Part 2 Overview of FRP-reinforced concrete structures. Seismic response** is a state-of-the-art review of FRPs and the structures that comprise them. It will describe the components as well as the manufacture of FRP bars and their physical and mechanical properties. It will discuss the design principles and structural behaviour of these structures, including under fire and seismic conditions.
- **Part 3 Numerical modelling** will introduce and compare the different numerical modelling methods. It will also present two existing studies on the seismic behaviour of GFRP-reinforced concrete structures on which the chosen modelling method will be tested and approved.
- **Part 4 Design methods following the codes** will present the guidelines from the new generation of Eurocode 2 and other codes for designing an FRP-reinforced structure. These guidelines will then be applied to the two studies presented in Part 3.
- **Part 5 I-shaped wall design** will present all the characteristics of the case-study structures, such as their geometry and properties. It will then focus on the verification of its design using the guidelines presented in Part 4 and the numerical modelling chosen in Part 3.
- **Part 6 Experimental programme at LEMSC** will discuss the test setup at LEMSC of the I-shaped wall presented in part 5, its loading protocol and the instrumentation that will be used to collect the data.
- **Part 7 Conclusions and future developments** will finally summarise the general findings of this work and discuss the elements which require further investigation in the future in order to develop the knowledge of FRP-reinforced concrete structure.

Finally, plenty of external files have been produced for the sake of this work using different software programs: SeismoStruct, Response-2000, Excel and SolidWorks. All files are available on the following Drive:

`https://drive.google.com/drive/folders/1ORh15RcR3DMTAsCNg5QFsMNed23D3jVN?usp=sharing`

Chapter 2

Overview of FRP-reinforced concrete structures. Seismic response

The aim of this chapter is to provide an overview of the FRP material, from its composition and manufacture to its properties. It will also address the design of FRP-reinforced concrete structures by discussing its structural behaviour, existing codes and durability. Finally, the behaviour of these structures subjected to a seismic event will be covered, focusing on columns and walls.

2.1 Material, geometry, manufacturing

2.1.1 Introduction to FRP rebars

FRP rebars consist of fibers impregnated in a resin matrix. The fibers have a structural role that influences the strength and stiffness of the rebars, while the matrix (resin) mainly binds the fibers together. The resin also serves to protect and transfer the loads to the fibers. It, therefore, influences the fracture mechanism and fracture toughness [2, 15].

Most commonly, FRP rebars are produced using a pultrusion process. FRP reinforcements can also contain a surface deformation pattern and take the form of a bar, cable, or profile.

The different types of fiber and resin as well as their properties will be presented in the next subsection. It will be primarily based on a report published by the FIB [2] and on a book written by Nanni & al [15]. The existing geometries will also be examined in relation to the manufacturing process.

2.1.2 Types of fibers

There are 4 types of fiber commonly used for FRP reinforcing bars: glass, aramid, basalt, and carbon fiber. The properties and advantages of these different fibers are described below.

Glass fiber (GFRP)

Glass fiber is the most commonly used. There are different types of glass as E-glass (electrical), S-glass (high-strength), and AR-glass (alkali-resistance). E-glass is very popular in the reinforced plastic fiber industry because of its electrical insulation and high mechanical properties, but also its low cost compared to other glass fibers. S-glass has higher tensile strength and modulus, but its cost inhibits its use over E-glass. AR-glass has a high resistance to corrosion due to alkali attacks in cement matrices. Currently, no fiber sizes that are compatible with commonly used thermoset resins are available.
Glass fiber has good electrical and thermal insulation properties. Its tensile strength is considered constant for the temperatures to which it is subjected during use but decreases with sustained loads and chemical corrosion.

Carbon fiber (CFRP)

The carbon fibers that are the most used in civil engineering applications are produced by the thermal decomposition of polyacrylonitrile (PAN). These fibers are presented on the market in long continuous tows. They have a relatively high tensile strength and modulus and are stable to temperature. Carbon fibers are also resistant to aggressive environmental factors such as alkali or acid attacks. It has a high fatigue strength and is brittle. The fibers are not easily wetted by the resins, so it is necessary to size them before their incorporation into the matrix. On top of that, they are about 10 times more expensive than glass fibers.

Aramid fiber (AFRP)

Aramid is an organic aromatic polyamide fiber with the lowest density and highest tensile strength-to-weight ratio of current reinforcement fibers. Indeed, the tensile strength is higher and the modulus is approximately 50% higher compared to glass fiber. These fibers are produced by different industries but the most common is Kevlar with three types: Kevlar 29, 49, and 149. Aramid fibers, like other fibers, have a brittle behavior in tension. However, it is ductile in compression with high plasticity in bending. As a result, these fibers have a high impact resistance, which is not the case for glass or carbon fibers. Aramids also have good insulating properties but are sensitive to ultraviolet light, moisture, and high temperatures. The good mechanical properties of this fiber are counterbalanced by its high cost, which limits its use.

Basalt fiber (BFRP)

Basalt fibers are produced in the same way as E-glass but require less energy. In addition, basalt rock is available worldwide. They are mechanically advantageous as they are slightly stronger and have a higher modulus than E-glass. They are also non-toxic and non-corrosive, which makes them good for the environment. They have good fire resistance and insulation properties. This is important to note they have a high bio solubility (ability to dissolve in contact with biological fluids), which is now a requirement of international guidelines. Finally, they are much cheaper than carbon fibers. So, for all these advantages, researchers are exploring the possibility of using these fibers for FRP rebars.

2.1.3 Types of matrices

There are two types of matrices: thermoplastic and thermosetting resins. The main difference is that, once cured, thermoplastic resin is able to return to its original shape or reshape, unlike thermoset resin. The most commonly used matrices are the thermoset ones, of which there are three main types: epoxy, polyester, and vinyl ester. The properties of these three resins will be described in this section.

Epoxies

Epoxy is a resin compatible with glass, carbon, aramid, and basalt fibers. When mixed with other resins, specific characteristics can be achieved. The most common use is in the creation of high-performance composites. The advantages of this resin are high mechanical properties, high corrosion resistance, good electrical properties and it is not much affected by heat and water. In addition, it is easy to process and has minimal shrinkage during curing. However, epoxy resins also have some disadvantages. It is expensive (its cost is proportional to its performance) and has a long curing time. Furthermore, it is limited in the pultrusion industry.

Polyesters

There is a wide variety of polyester with different flexibility depending on the type of diacid. This kind of resin is characterized by a combination of good mechanical, electrical, and chemical properties. Less expensive than epoxy, easy to put in place, and stable are its advantages. The properties of polyesters can be chemically modified to achieve desired characteristics such as heat or corrosion resistance. Glass fiber and polyester resin structures have been around for more than 30 years, and today they are still in good condition, with only a small loss of strength and discoloration. However, due to their poor chemical resistance, they are not recommended for use in the manufacture of FRP rebars. Another negative point is the large volume shrinkage, but this can be reduced by incorporating a thermoplastic component.

Vinyl esters

Due to their properties, vinyl esters are the ones most commonly used for the manufacture of FRP composites. They are more flexible than polyesters due to their chemical structure. In fact, they are a mixture of the good properties of epoxies and polyesters. In particular, they have good chemical resistance and tensile strength like epoxies and fast curing and viscosity like polyesters. In addition, they are alkali-resistant and they also have good wet-out and adhesion with glass fibers. Unfortunately, they are somewhat inferior to epoxies in some respects: a higher volumetric shrinkage and moderate adhesive strength.

2.1.4 Manufacturing by pultrusion

The most commonly used production process for FRP rebars is pultrusion. This is a continuous laminating process that combines the fibers and matrices discussed above. This highly automated process produces constant cross-section profiles such as rebars [1].

Figure 2.1 illustrates the pultrusion manufacturing process. Initially, the fibers of glass, carbon, or aramid are positioned in the form of rovings. The material is first spread for uniform wetting and then pulled to define the desired shape and size. Then the fibers are impregnated with a resin matrix (polyester, vinyl ester, or epoxy) and covered with a coating of sand and helicoidal wraps. The materials are then fed into the heated pultrusion die where they are cured. The temperature is precisely controlled and the heat allows the resin to harden. Once the bar has solidified, it is allowed to cool and then pulled from the oven at a constant speed. Finally, the profile is cut to the desired length [15].

The pultrusion process takes varying amounts of time depending on the dimensions of the final reinforcement. In general, production reaches 0.91m per minute [15].

If curved reinforcement bars are required, the manufacturing process is different. Once the resin has solidified, bending the bar becomes impossible because the fibers cannot reorient themselves in the resin matrix. Therefore, the bending has to be done during the manufacturing of the rebars by injecting the resin into a mold where there are already reinforcing

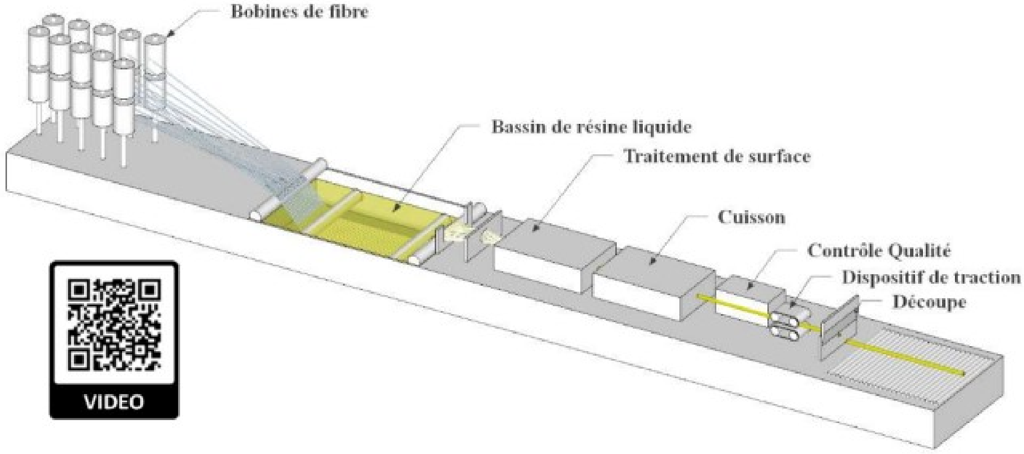

Figure 2.1: Diagram of the pultrusion process [7]

fibers [9].

2.1.5 Geometry

An important feature of the reinforcements is the surface deformation pattern. This finish has a major influence on the bond between the FRP rebars and the concrete. There are different types depending on the manufacturer featured in Figure 2.2: (a) sand coating, (b) externally wound fibers (often with a sand coating), and (c) surface-formed deformations or ribs [9].

Figure 2.2: FRP rebars with different types of surface finishes: a) sand coating b) sand coating with exterior wound fibers ribs c) ribs and d) ribs [9]

Figure 2.3 shows the bar sizes available. These are similar to those for steel reinforcement. There are twelve standard sizes ranging from 6 mm to 60 mm in diameter. GFRP rebars are generally produced in diameters between 6 mm and 36 mm. Smaller diameters are also available from some suppliers in the form of coils. The rebars are available in lengths from

10 to 14 m. Finally, some profiles do not have a round cross-section but are rectangular or braided.

Bar size designation		Nominal diameter, mm	Area, mm^2
Standard	Metric conversion		
No. 2	No. 6	6.4	31.6
No. 3	No. 10	9.5	71
No. 4	No. 13	12.7	129
No. 5	No. 16	15.9	199
No. 6	No. 19	19.1	284
No. 7	No. 22	22.2	387
No. 8	No. 25	25.4	510
No. 9	No. 29	28.7	645
No. 10	No. 32	32.3	819
No. 11	No. 36	35.8	1006
No. 14	No. 43	43.0	1452
No. 18	No. 57	57.3	2581

Figure 2.3: ASTM standard reinforcing bars [19]

2.2 Mechanical and physical properties

2.2.1 Mechanical behaviour

Tensile behaviour

The behavior of FRP reinforcing bars is characterized by a linear elastic stress-strain curve until failure (Figure 2.5). Unlike steel (Figure 2.4), FRP rebars do not have plastic behavior prior to failure, which makes them brittle and not ductile. The tensile strength of these rebars is higher than for steel, while the elastic modulus and ultimate strain are lower than in the case of steel [9, 14, 15, 19].

The tensile strength of FRP rebars is influenced by several parameters:

- Fiber-volume fraction: the ratio between the volume of the fibers and the total volume of the bar [14, 19]
- Manufacturing process, quality control method, rate of (resin) curing [14, 19]
- Diameter: due to shear lag, the fibers close to the center and those facing outwards from the section do not experience the same stresses. Therefore, as the diameter increases, the strength decreases [14, 15, 19]

- Bending of FRP rebars: it reduces their tensile strength by up to 50% [9]

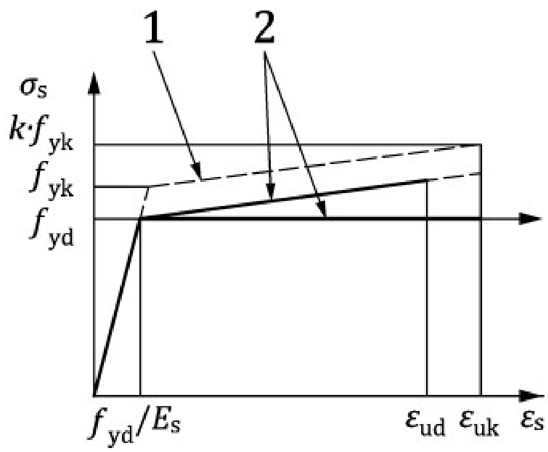

Figure 2.4: Stress-strain diagrams for carbon reinforcing steel for tension and compression (1: nominal diagram for reference 2: design diagrams) [6]

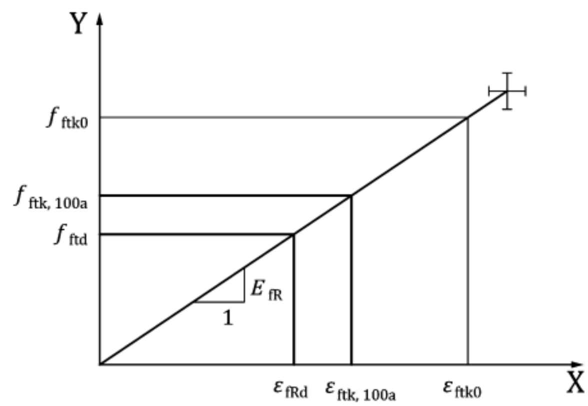

Figure 2.5: Stress-strain diagram for FRP reinforcement [6]

Figure 2.6 shows the usual tensile properties of FRP and steel rebars such as tensile strength and elastic modulus.

Material / Properties	Steel	GFRP	CFRP	AFRP
Nominal yield stress, MPa	276–517	N/A	N/A	N/A
Tensile strength, MPa	483–690	483–1600	600–3690	1720–2540
Elastic modulus, GPa	200.0	35.0–51.0	120.0–580.0	41.0–125.0
Yield strain, %	1.4–2.5	N/A	N/A	N/A
Rupture strain, %	6.0–12.0	1.2–3.1	0.5–1.7	1.9–4.4

Figure 2.6: Usual tensile properties of reinforcing FRP and steel rebars [19]

Compressive behaviour

The compressive strength of FRP rebars is usually not considered in the design calculations. Indeed, studies have shown that this strength is much lower than the tensile strength. The rebars can exhibit different modes of failure such as transverse tensile failure, fiber micro buckling, or shear failure depending on the fiber type, resin, and fiber-volume fraction. Compressive strength values of the order of 50%, 80%, and 20% of the tensile strength can be obtained for GFRP, AFRP, and CFRP rebars respectively [9, 15, 19].

On the other hand, the values for the compressive modulus of elasticity correspond to about 80%, 85%, and 100% of the tensile modulus for GFRP, CFRP, and AFRP rebars respectively [15, 19].

Due to the anisotropy of the material, it is not easy to characterize the compression behavior of FRP rebars. Moreover, there are no standards that include a characterization method. Therefore, the properties of these rebars have to be provided by the producer. For these and other reasons, design guides and codes do not recommend the use of FRP rebars as compression reinforcements [14, 15, 19].

2.2.2 Physical properties

Density

The density of FRP rebars varies between 1,25 and 2,1 g/cm^3 (see Figure 2.7), which is approximately $\frac{1}{6}$ to $\frac{1}{4}$ the density of steel. This has the advantage of reducing transport costs and facilitating on-site handling compared to steel [9, 15, 19].

Steel	GFRP	CFRP	AFRP
7.90	1.25–2.10	1.50–1.60	1.25–1.40

Figure 2.7: Typical density of FRP rebars [g/cm^3] [19]

Coefficient of thermal expansion (CTE)

As FRP reinforcements are anisotropic, their thermal coefficient of expansion is not the same in all directions [7]. It depends on the type of fibers, matrix, and volume fraction of the fibers [15, 19]. The CTE in the longitudinal direction depends mainly on the properties of the fibers. It can be seen from Figure 2.8 that CFRP and AFRP rebars have a negative coefficient, which means that they contract under the effect of heat [19]. In contrast, GFRP rebars have a positive coefficient of thermal expansion of the same order of magnitude as concrete. The transverse CTE depends mainly on the properties of the matrix. Here, the values in the Figure 2.8 show that FRP rebars have a larger coefficient than concrete and therefore, under the effect of heat, can induce cracks in concrete [9].

Direction	CTE × 10^{-6}/°C			
	Steel	GFRP	CFRP	AFRP
Longitudinal, α_L	11.7	6.0–10.0	(−9.0)–(0.0)	(−6.0)–(−2.0)
Transverse, α_T	11.7	21.0–23.0	74.0–104.0	60.0–80.0

Figure 2.8: Typical coefficient of thermal expansion for reinforcing bars [19]

2.3 Structural behaviour and design principles

Steel-reinforced concrete structures are commonplace in this world. For decades, they have been studied and tested to characterize their behavior on many different structures. This is not the case for FRP-reinforced concrete structures. Today, it is known that steel has an elastoplastic behavior that allows it to deform significantly before breaking. This ductility of steel is an advantage to be taken into account in the design. Indeed, the deformation of the steel and the cracks created without too much loss of strength allow users to be warned of the state of the structure before it collapses. On the contrary, since FRPs have linear elastic behavior, there are no warning signs of failure. This characteristic must be taken into account when designing FRP-RC structures. In this section, the difference in design between conventional steel-reinforced concrete structures and FRP-RC structures will be discussed mainly based on the work of Firmo & al [9].

2.3.1 Bending

Studies on the subject have shown that similar design principles can be applied to FRP-RC structures as to conventional steel-reinforced concrete structures structures. Thus, standard sectional analysis can be used for the bending of beams.

Here are the following hypotheses for the flexural design of FRP-RC structures [9, 14]:

- **H1** Plain section remains plain after deformation. The strain is proportional to the distance from the neutral axis (Bernoulli-Euler assumption).
- **H2** There is a perfect bond between the concrete and the rebars such that they incur the same deformation.
- **H3** The tensile strength of the concrete is neglected.

Three modes of rupture can occur (i) FRP tensile rupture, (ii) concrete crushing, or (iii) both simultaneously. So, the flexural strength of FRP-RC elements can be established by [9]:

- failure mode

- strain compatibility
- internal force equilibrium
- considering the linear elastic behavior up to a failure of the FRP reinforcement

Note also that the contribution of FRP rebars under compression to the flexural strength depends heavily on the lateral confinement, and therefore it is on the safe side to not consider it for design purposes.

In the case of tensile rupture of the FRP reinforcement, the failure is sudden and therefore brittle, unlike steel which is ductile. However, some warning signs can be observed such as cracking and large deflection due to the high failure strain and low modulus of elasticity of the FRP rebars. In the case of concrete crushing failure, since concrete has a non-linear behavior, the structure shows a plastic behavior before failure. Since this phenomenon is preferable, it is advisable to design the structure so that it is over-reinforced. In addition, the deformation capacity of concrete in compression can be enhanced by increasing the confinement, which further improves the "pseudo-ductile" behavior of the structure.

Often, service requirements are the determining design factor for FRP-RC flexural members. GFRP reinforcement, which is most commonly used, has a modulus of elasticity between 3 and 6 times smaller than steel. This low stiffness leads to higher deflections in the elements than when steel is used. In fact, the amount of reinforcement required generally results in a higher strength than that required for the ultimate flexural state. Thus, the lack of ductility and few signs of failure mentioned above are covered by this SLS design.

In service, this low stiffness of FRP reinforcement can cause larger cracks. These are generally allowed due to the resistance of the reinforcement to electrochemical corrosion. Code limits on crack openings are primarily for aesthetic reasons and to maintain the shear strength of the concrete.

Another point of attention is the sensitivity of FRP rebars to creep failure. They can fail under the effect of quite small sustained stresses. For this reason, codes recommend limiting the maximum allowable stress under service loading.

As a conclusion of the previous paragraphs, it can be observed that the bending elements in FRP-RC are sized by the SLS requirements. In fact, most of the cross-sections are over-reinforced. As a result, the failure mode of the elements is crushing of the concrete and the tensile strength of the FRP reinforcement is not fully used.

2.3.2 Shear

Even after years of research, the shear behavior of steel-RC structures remains a topic of debate. Similarly, the shear behavior of FRP-RC elements is also under discussion, although it has been much less studied. The following paragraph will be dedicated to the design recommended by the current codes.

The shear behavior of reinforced concrete elements depends on four internal loading mechanisms [9]:

- Shear strength derived from the undamaged compression region
- Contribution from the interlocking of aggregates formed within fractured areas
- dowel action furnished by the longitudinal reinforcement within fractured zones
- shear resistance from the added shear reinforcement

The behavior is therefore influenced by the characteristics of the concrete, but also by the bond and the properties of the reinforcement, such as ductility and modulus of elasticity.

The characteristics of the longitudinal reinforcement influence the depth of the neutral axis and thus the contribution of the uncracked concrete. Due to the low axial stiffness of FRP reinforcement, the corresponding neutral axis depth is generally lower than in the case of steel reinforcement. However, as explained in the section on bending behavior, the design of FRP-RC structures is generally governed by the service requirements. Thus, the depth of the neutral axis is often increased by the very high ratio of longitudinal reinforcement required.

The second mechanism (contribution of the aggregate interlock developed throughout cracked zones) influencing shear depends on the crack opening in the concrete. As mentioned in the previous section, the cracks are larger when using FRP than when using steel due to the lower modulus of elasticity which results in large deformations. Due to these large crack openings, this mechanism has little effect on the shear strength of the element.

The third mechanism related to dowel action in cracked sections depends on the bending and transverse shear properties of the reinforcing bars at these locations. Again, FRP rebars have low stiffness, as well as low shear strength. In addition, they are anisotropic. Therefore, the shear strength of this mechanism is the lowest of the 4 and can be neglected.

When the shear demand is greater than the combined shear strength of the four mechanisms, then transverse reinforcement should be incorporated. A point of attention is the loss of strength of bent FRP rebars. These strength reductions can be as much as 50% regularly and depend on the diameter and radius of curvature of the bar. This limited strength must therefore be taken into account when designing a transverse reinforcement supplement.

In conclusion, it is observed that the shear resistance is provided by both the concrete and transverse reinforcement shear resistances as long as the cracks are well controlled. Therefore, equations similar to those for conventional steel-reinforced concrete structures can be used, taking into account the reduced stiffness and strength of the bent FRP reinforcement.

2.4 Design guidelines and codes

Several codes have been developed since the 1990s for the design of FRP-RC structures. The guidelines and equations are based on those for the design of much more studied conventional steel-reinforced concrete structures. These standards are adapted to the characteristics and properties of FRP. Given the current limited knowledge of the behavior of structures with FRP, the provisions are very conservative. FRP rebars have not been widely adopted for designing lateral load-resisting elements like RC walls in earthquake scenarios due to the absence of a well-established methodology that ensures sufficient ductility and energy absorption during seismic events [4]. Such critical topics still need to be studied in more depth in order to optimize the design and extend the use of FRPs.

Table 2.9 below lists the codes and guidelines for the design of FRP-RC structures that are the most widely used, disseminated, or published by organizations such as the Japan Society of Civil Engineers (JSCE), the International Federation for Structural Concrete (FIB), the Italian National Research Council (CNR), the American Concrete Institute (ACI) and the Canadian Standards Association (CSA) [9]. The codes mentioned may have evolved since their first publication as a result of ongoing research, the versions quoted are the latest at the time of the paper publication [9]. Also, a future version of Eurocode 2 is currently being developed. This version will include an annex concerning the design of concrete structures reinforced with FRP rebars.

Guideline/code	Organization /publisher	Year*
Recommendation for Design and Construction of Concrete Structures Using Continuous Fiber Reinforcing Materials [27]	JSCE	1997
Guide for the Design and Construction of Concrete Structures Reinforced with Fiber-Reinforced Polymer Bar – CNR-DT203/2006 [28]	CNR	2007
FRP Reinforcement for RC Structures - Bulletin 40 [10]	FIB	2007
Design and Construction of Building Components with Fibre-Reinforced Polymers – CSA-S806:12 [29]	CSA	2012
Guide for the Design and Construction of Structural Concrete Reinforced with FRP Bars – ACI 440.1R-15 [4]	ACI	2015
Informative Annex in the next generation of EN 1992-1-1	CEN	-

*Note: year of publication of the current version of the document.

Figure 2.9: Design guidelines and codes for FRP-reinforced concrete structures [9]

2.5 Critical topics

In this section, the behavior of FRP reinforcement and FRP-RC structures in critical situations will be studied. It will mainly focus on the fire behavior as well as the durability of these structures. This section is mainly based on the work of Firmo & al [9], on the book of Nanni & al [15], on the report of FIB [2] and on the AFGC guide [7].

2.5.1 Fire

Fire resistance is an important issue for FRP-RC structures to check because of the sensitivity of GFRP to high temperatures. Fire resistance calculations for steel-reinforced concrete structures can also be applied when using FRP. Indeed, research has shown that FRP elements can achieve the same fire safety requirements or even comparable fire resistance as steel elements. However, to use similar equations, it is necessary to take into account the degradation of the reinforcement and of the concrete/reinforcement interface due to the temperature.

The increase in temperature causes greater effects on GFRP rebars than on steel rebars. These effects have been observed to be more significant when the temperature reaches the glass transition temperature (Tg) of the resin, which is generally between 93°C and 120°C for GFRP rebars. Near this temperature, the matrix softens and is no longer able to transfer the stresses from the concrete to the fibers due to the loss of adhesion between the reinforcement and the concrete. The compressive and transverse shear strengths, which are mainly dependent on this fiber/matrix interaction, are strongly reduced and become zero well before the resin decomposition temperature (Td, which is between 250°C and 400°C).

When the Tg temperature is exceeded, the bar can still support loads because it still has a high tensile strength and modulus of elasticity up to high temperatures. Indeed, the stiffness and tensile strength depend mainly on the fibers which have a decomposition temperature (1070°C for glass fibers) much higher than that of the resin.

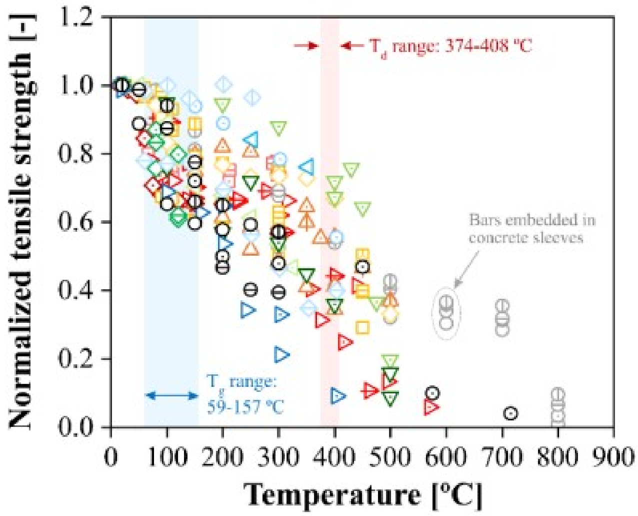

Figure 2.10: Normalized tensile strength of GFRP rebars as a function of temperature [9]

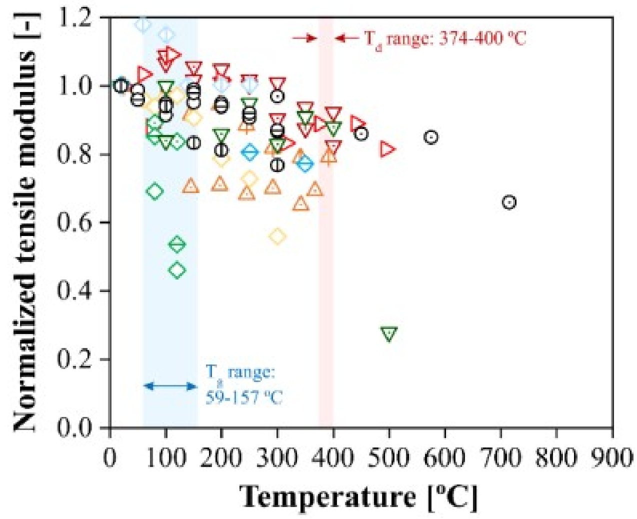

Figure 2.11: Normalized tensile modulus of GFRP rebars as a function of temperature [9]

The tensile modulus, which depends exclusively on the fibers, can retain up to 70% of its value at temperatures up to 700°C as can be seen in Figure 2.11. The tensile strength depends mainly on the fibers but also to some extent on the fiber-matrix interaction. In fact, it can be seen in Figure 2.10 that it decreases much faster and can already lose 40% of its value near Tg.

Although the tensile strength of the rebars is not strongly influenced by the softening of the matrix, it is mainly the bond between the rebars and the concrete that suffers. The anchorage capacity of the reinforcement can be affected by the inability to transfer tangential stresses from the concrete to the fibers. Many parameters influence the bond of the rebars and little is known about its behaviour at elevated temperatures. Despite this, it would appear that the two important factors are the temperature Tg and the surface condition of the rebars.

It is difficult to define the behavior of rebars at high temperatures as the degree and rate of degradation are influenced by different factors:

- Material properties (fibers and matrix)
- Bar geometry (surface finish, cross-section)

- External factors linked to heating and loading history, as well as environmental exposure

The effects of temperature on the strength of FRP rebars are increasingly being studied and the knowledge gained points to the possibility of using FRP reinforcements even in cases where fire safety is a particular concern. However, in practice, the use of FRP reinforcements is low as there are few guidelines for fire design. At the moment, only the Canadian standard CAN/CSA S806-12 and the American guide ACI 440.1R-15 offer recommendations, but these are limited and not very detailed compared to those for the use of steel reinforcements.

For example, for the concrete cover, the Canadian standard specifies a minimum of 50 mm to guarantee 60 min of fire exposure. However, it is possible to increase the fire resistance to 180 min with a lower cover if the reinforcing bars are well anchored in cold zones of the structure.

This brings us to the last sensitive point, the ends of the reinforcement. If these approach the Tg temperature, there will be risks of detachment in the anchorage areas which may cause the structure to collapse. However, if continuous reinforcement is placed throughout the element and the ends are protected from the heat rise, the design guides indicate that the risk of failure of the structure is low and that it can withstand a fire exposure of 60 min to more than 180 min. In order to protect the anchorage areas, it is preferable to extend the rebars into cooler areas such as the connections between slabs and beams or above columns. Also, curved GFRP reinforcement is a good solution to improve the anchorage capacity at high temperatures.

In conclusion, the fire resistance of GFRP-RC structures is influenced by the following parameters:

- Anchoring conditions for reinforcement
- Degradation of the mechanical properties of reinforcement due to fire
- Reinforcement-concrete bonding
- Concrete cover

2.5.2 Durability

In order to measure the durability of FRPs, several methods can be used to predict or at least extrapolate the actual behavior of structures over their lifetime. These techniques expose the reinforcement to more severe stresses than the structure will actually be subjected to and this allows extrapolation of long-term strength estimates. The parameters studied are tensile strength, modulus of elasticity, and adhesion, for example.

Today, the major problem is the lack of general and internationally recognized test methods. In addition, the manufacturing methods and the different categories of FRP (including fibers and resins) are variable for each producer. The results of the research are therefore often diverse, which does not allow for the existence of a general standard that can be used by engineers. However, there are a few points that are often verified.

In order to study the durability of FRP composite reinforcements, three elements must be considered [2]:

- The fibers
- The matrix/resin
- The interface between fibers and matrix

The following paragraphs will present the effects of chlorides, alkali, sustained stress, ultraviolet radiation, and carbonation on these three elements.

Effects of chlorides

One of the advantages of FRP is that it can be used in a saline environment, for example when using road salt or when exposed to seawater where the steel would corrode. The numerous studies on the effect of chlorides on FRP rebars do not allow any conclusions to be drawn. Indeed, the results obtained are very scattered as it is difficult to distinguish between chloride attack, alkali attack on the fibers, or degradation due to humidity. In general, studies have shown that CFRP rebars are very little affected, whereas GFRP and AFRP rebars can lose up to 50% of their strength and stiffness. Finally, even if the effect of chloride on FRP rebars cannot be fully demonstrated, it is still observed that saline solutions are slightly more aggressive than freshwater [2].

Effects of alkali

The performance of FRP reinforcements is also affected by an alkaline environment (such as concrete containing alkaline aggregates or the presence of alkaline chemicals). Indeed, it has been observed that FRP rebars are affected more quickly in these alkaline environments than in concrete. The FIB [2] suggests that the higher mobility of OH- ions compared with concrete is responsible for this greater degradation. It would also appear that carbon fibers are more resistant than aramid and even more than glass fibers. It should be noted, however, that the amplitude of degradation varies according to the manufacturer and therefore the fibers, resins, and manufacturing processes used.

As the studies progressed, several observations were made [2]:

- Significant degradation of GFRP rebars after exposure to alkaline solutions at high temperature.
- AFRP rebars are less affected by an alkaline environment than GFRP rebars. Nevertheless, significant degradation is observed when they are subjected to the combination of an alkaline solution and a high tensile stress.
- Vinyl ester resins are more resistant to alkalis than polyester resins.
- CFRP rebars with a good choice of fibers and resins do not seem to be considerably damaged by alkalis.

Effect of sustained stress

The durability of a material also depends on its creep failure. Indeed, an FRP bar can fail in the long term when subjected to tensile stresses lower than the ultimate tensile stress in the short term. Of the FRPs, CFRPs have the best creep resistance, while GFRPs and AFRPs have relatively low resistance.

The time to failure is proportional to the sustained load. Thus, one can use the results obtained for high loads to extrapolate to values for a large duration such as the lifetime of the structure.

Other parameters than stresses can influence creep failure such as the environment. For example, an immersed glass fiber can only withstand 50% of its ultimate load over a period of 100 years, whereas if it is dry, it can withstand 70% of its strength over the same period. Likewise, the presence of alkalis, for example, can cause failure very early on.

There are many studies on the subject with more or less different results. In general, however, the results show that the critical stresses for creep are on average 35% for GFRP, 45% for AFRP, and 75% for CFRP [7, 15].

Finally, given the constant evolution in terms of manufacturing and material quality, some FRP rebars may have better characteristics. Therefore, when designing, it is possible to use less restrictive values if these are supported by test results. There is therefore an increasing need to determine generalized test methods for characterizing the creep resistance of a material that can be used internationally.

Ultraviolet radiation

Ultraviolet (UV) light can also degrade FRP rebars in the long term. Indeed, UV light is known to deteriorate polymeric materials and FRP rebars can be subject to this phenomenon during storage or if the FRP is used as external reinforcement. However, when the reinforcements are integrated into the concrete, there is no longer any risk as the concrete provides protection against UV exposure. Numerous field and laboratory tests were conducted with UV exposure and in each case, the tensile strength was measured before and after the test. One of the results was that CFRP did not suffer any loss of strength due to UV, whereas AFRP and GFRP lost respectively 13% and 8% of their strength [15].

Carbonation

The EUROCRETE project carried out studies on the influence of carbonated concrete on FRP reinforcements. Although the results were very scattered, no degradation of the reinforcement due to carbonation was found because carbonation involves a reduction in pH, which in turn reduces the alkali in the water in the concrete interstices. By preventing alkali from degrading the fibers, the durability of FRP in reinforced concrete is even improved.

2.6 Seismic response of GFRP-RC structures

This section will deal with the seismic behavior of structures reinforced with FRP rebars. It will only cover existing studies that have used GFRP rebars, as these are the ones most commonly used in construction today. Because of their low cost compared with AFRP and CFRP and their good technical properties, they are generally preferred.

2.6.1 Introduction to seismic behavior

Even today, FRP reinforcement is only rarely used in construction, and one of the reasons for this is due to seismicity. As already known, FRP rebars are not ductile like steel, but brittle. This behavior of FRP-RC structures raises the question of the possibility of the presence of this type of structure in regions where the seismic character is important. Unfortunately, as this subject is still largely unstudied, design codes and standards do not provide for seismic design and even do not recommend the use of FRP.

2.6.2 Seismic response of GFRP-RC columns

Despite the limited number of studies on the subject, it is possible to draw several conclusions from those that do exist concerning seismic behavior. This section is based on the work of Firmo & al [9].

As mentioned above, it is advisable to design over-reinforced sections to allow failure by crushing the concrete and thus avoid brittle failure of the FRP rebars in tension. Under static loads, some studies have shown semi-ductile failures.

For cyclic loading, the hysteretic model remains relatively similar to the one for conventional steel-reinforced concrete structures, but in the case of FRP rebars, the unloading branches point toward the origin.

Studies carried out on FRP-RC columns have shown significant elastic deformation when the amount of transverse FRP reinforcement is large enough to confine the concrete sufficiently. A significant ratio between the lateral displacement imposed and the height of the columns without any ductility was observed. This noticed elastic deformation could be sufficient to comply with the seismic drift limits of the construction codes.

On the other hand, as shown by some studies, it is possible to increase the elastic deformation of columns by spacing the stirrups to ensure concrete confinement. By increasing this elastic capacity, residual deformations are minimized when the structure is subjected to a seismic event. These FRP-RC structures then have a re-centering capacity that limits repairs and therefore costs.

When it comes to joints between beams and columns, studies of GFRP-RC joints have revealed a certain lack of ductility and poor energy dissipation. To remedy this, there are hybrid steel-FRP-RC joints with better characteristics. However, the use of steel makes this solution corrodible. Another hybrid joint was therefore studied: a joint comprising an SMA-FRP shape memory alloy reinforcement. This has adequate energy dissipation capacity, but its use is hampered by the cost of SMA.

As mentioned previously, FRP-RC structures can reach semi-ductile failure and therefore dissipate inelastic energy. Some studies have shown that this energy dissipated in the case of rectangular FRP-RC columns would be more or less half of the energy obtained if the column were made of conventional steel-reinforced concrete structures.

Finally, given the conclusions of the various studies, it would be suggested to use an elastic approach with sufficient deformations to satisfy the limits of the construction codes. This approach would then be appropriate for seismic design.

2.6.3 Seismic response of GFRP-RC walls

As this thesis is concerned with the seismic response of a GFRP-RC wall, it is also appropriate to discuss existing studies concerning walls. This thesis is focusing particularly on two papers on which our numerical and analytical predictions will be checked (Chapters 3 & 4).

Mohamed & al (2013)

This first study is entitled "Experimental Investigation of Concrete Shear Walls Reinforced with Glass fiber-Reinforced Bars under Lateral Cyclic Loading" [13].

- **Objectives and motivation**
  In everyday life, buildings are subject to lateral forces such as wind and earthquakes. Conventional reinforced concrete shear walls have already proved their effectiveness in this context. However, as already introduced in this chapter, it is advisable to try to replace steel with GFRP reinforcements. Indeed, steel is sensitive to corrosion and this is aggravated by the use of de-icing salt, which is not the case with GFRP. The many uses of GFRP in different structures have already demonstrated its applicability. Despite the still high cost of production, the much lower maintenance costs compared with steel maintain the advantage of its use. If steel is to be replaced by GFRP, its behavior in a structure such as a shear wall needs to be studied. The aim of this study was therefore to check whether the strengths and deformations could meet the criteria for use. To meet the criteria, the walls tested had to [13]:
  - reach their flexural capacity
  - avoid all brittle failures
  - meet drift and energy dissipation requirements
  - show no significant loss of resistance to wind and/or seismic loads simulated in cyclic load tests
- **Summary of the experimental Program**
  The experimental program consisted of the study of 4 reinforced concrete shear walls, one reinforced in steel (ST15) and three reinforced with GFRP (G10, G12, and G15) subjected to quasi-static loading. The four walls were designed in compliance with the regulations to avoid sliding and shear failure. The walls were 3500mm high and 200mm wide with lengths of 1000mm, 1200mm, and 1500mm respectively for G10, G12, and G15. These are medium-rise walls since their aspect ratio lies between 2 and 4.

Figures 2.12a and 2.12b show the geometry of the GFRP-reinforced concrete shear walls, a description of their reinforcement, and the test setup.

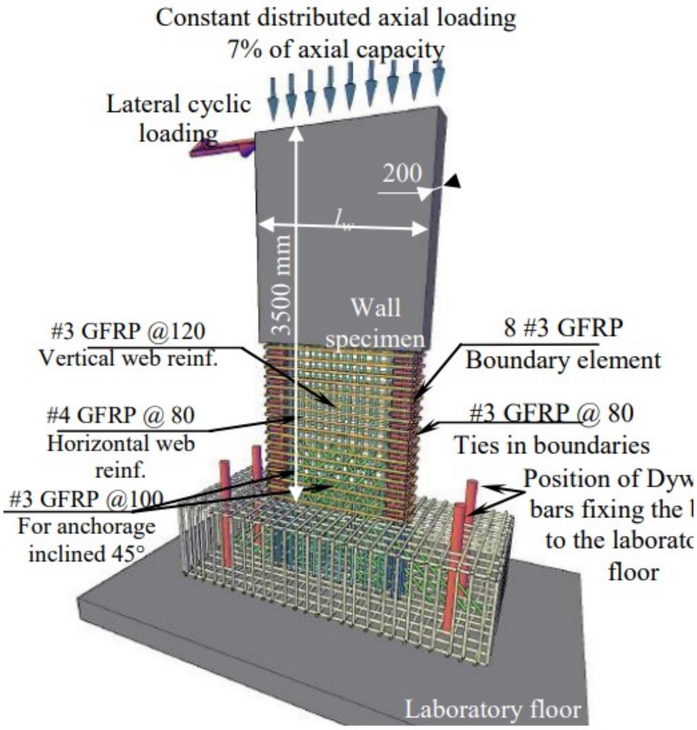

(a) Concrete dimensions and reinforcement details

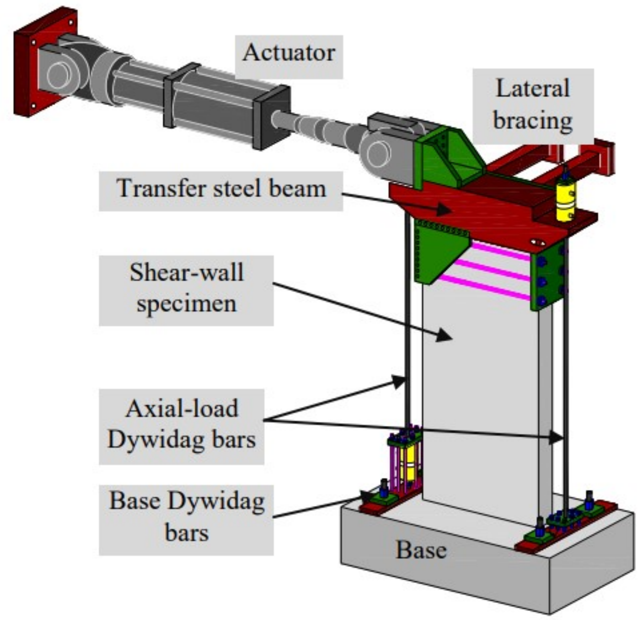

(b) Test setup

Figure 2.12: Experimental program: geometry and test setup [13]

- **Results**

  As previously stated, the aim of this study was to validate the use of GFRP as a reinforcement in shear walls subjected to lateral loads such as an earthquake. Here are some of the conclusions drawn from the results [13]:

  – All specimens reached their flexural strength without any indication of early shear or anchorage failure.

  – GFRP-reinforced walls experienced cover splitting at higher drift levels than the steel-reinforced ones.

  – The GFRP-reinforced walls exhibited elastic behavior, featuring repositioned cracks and reversible deformation up to a lateral drift of 2%.

  – When accounting for the minimal residual force of GFRP, they attained satisfactory levels of dissipated energy in comparison to the steel-reinforced one.

  – The most significant benefit of GFRP reinforcement is the absence of permanent deformation up to 80% of the ultimate capacity.

This study showed that GFRP reinforcements are capable of maintaining good strength and properties such as sufficient energy dissipation and deformation capacity to be used in shear walls. This result encourages the development of guidelines and design criteria for GFRP-reinforced shear walls.

Zhang & al (2019)

This second study is entitled "Structural behavior of seawater sea-sand concrete shear wall reinforced with GFRP bars" [23].

- **Objectives and motivation**

  It is common knowledge that conventional concrete has a significant impact on the environment, mainly due to the need for raw materials. In some regions, such as coastal areas, raw materials are scarce and each project requires imports, which cost money and pollute even more. In these regions, it would be highly advantageous to be able to use their natural resources: sea sand and seawater.

  Today, the use of seawater sea-sand concrete (SSC) is still limited, mainly because this concrete amplifies the corrosion on steel rebars. Several methods exist to counter this problem, including the use of corrosion inhibitors. However, an alternative method appears to be more effective: the use of FRP reinforcement to replace the steel.

  There are few studies on shear walls combining the use of FRP as reinforcement and SSC as concrete. The aim of this study was therefore to characterize the behavior of an SSC shear wall reinforced with GFRP. In order to be able to extend the use of this type of structure, the ones tested had to show the bearing capacity and deformability necessary to meet the requirements.

- **Summary of the experimental program**

  The experimental program consisted of the study of 3 reinforced concrete shear walls. The first wall (SNW) is reinforced with steel rebars and the concrete used is natural aggregate concrete (NAC). The second (GNW) uses the same conventional concrete (NAC) but with GFRP reinforcements. Finally, the third wall (GSW) is composed of SSC concrete and GFRP reinforcements. The three walls have been designed in compliance with regulations to avoid sliding and shear failure and to favor flexural behavior. The walls were 2400 mm high, 120 mm wide, and 800 mm long. These are high-rise walls since their aspect ratio is 3,7.

  Figures 2.13a and 2.13b show the geometry of the GFRP-reinforced concrete shear wall, a description of the test setup, and the instrumentation.

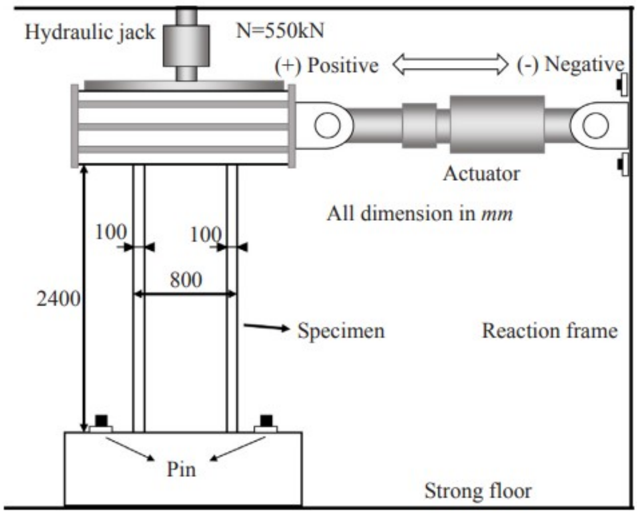

(a) Test setup

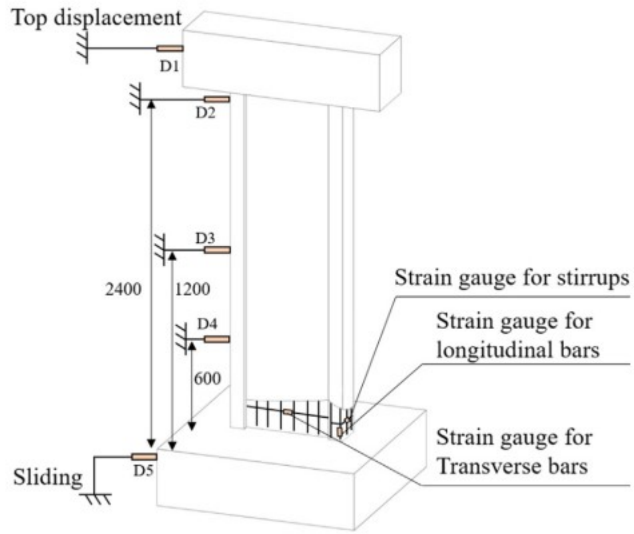

(b) Instrumentation

Figure 2.13: Experimental program: instrumentation and test setup [23]

- **Results**

  The aim of this study was to determine whether structures such as SSC shear walls reinforced with GFRP rebars could meet the criteria for seismic behavior. The results obtained seem quite convincing and encourage further development of these structures. Below are some of the conclusions drawn from this paper [15]:

  - The substitution of traditional concrete with seawater sea-sand concrete in shear walls exerts minimal impact on the short-term structural behavior. Nevertheless, further investigation into the long-term behavior is warranted.
  - Substituting steel reinforcement with GFRP rebars in SSC shear walls demonstrates satisfactory load capacity and deformation capabilities while maintaining the same reinforcement ratio.
  - Utilizing GFRP rebars reduces energy dissipation within the shear wall, and the GNW and GSW specimens display a brittle failure mode.
  - GFRP-reinforced shear walls exhibit reduced residual deformation, suggesting that the incorporation of GFRP rebars might offer a means to manage structural residual deformations.

Chapter 3

Numerical modelling

This chapter aims to establish a numerical model using Seismostruct and Response 2000 in order to predict the behavior of FRP-reinforced concrete shear walls under lateral loading. In Seismostruct, various types of numerical models will be examined to determine the most suitable one. Ultimately, the two articles highlighted in the section 2.6.3 and revisited at the beginning of this chapter will serve to validate our model and enhance our confidence in the outcomes.

3.1 Details of the tested walls from Mohamed & al (2013) [13] and Zhang & al (2019)[23]

3.1.1 Mohamed & al (2013): G10, G12, G15

The three walls that will be presented in the rest of this section correspond to the GFRP walls studied and tested by N. Mohamed & al (2013) [13].

Geometry

All walls are 200mm thick and 3500 mm high. The difference between the three units is their length: 1000 mm for G10, 1200 mm for G12, and 1500 mm for G15. They then have a shear wall aspect ratio of 3,5, 2,9, and 2,3 respectively.

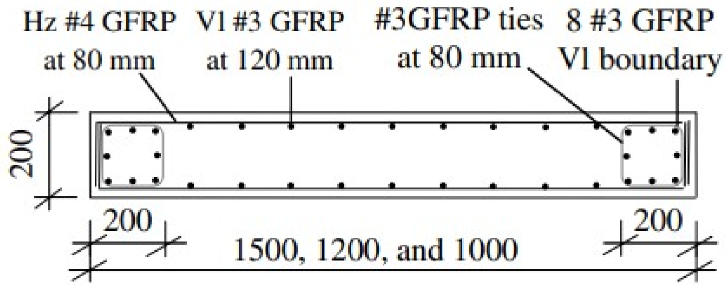

Figure 3.1: Cross section and reinforcement detailing of walls G10,G12 and G15 [13]

For longitudinal reinforcement, in the web, there are 10mm diameter GFRP bars spaced at 120mm on both sides. These same bars are also found in the boundary elements with 8 bars on each side of the wall. For horizontal reinforcement, there are rectangular stirrups #3 placed in the boundary elements of 10mm diameter spaced at 80mm. And finally, there are horizontal reinforcement bars #4 in GFRP of 13mm diameter also spaced at 80mm. These reinforcements are detailed in Figures 3.1 and 3.2.

Material properties

The two tables below 3.1 and 3.2 give the mechanical properties of concrete and GFRP rebars of the tested walls. For the diagonal elements of the beam-truss model, the tensile strength of the concrete is assumed to be zero.

Concrete Mechanical properties					
		G10	G12	G15	
Compressive concrete strength	f_c	40,2	39,8	39,9	MPa
Tensile concrete strength	f_t	3,5			MPa
Modulus of elasticity	E_c	29,8			GPa
Strain at peak stress	ϵ_c	0,2			%

Table 3.1: Mechanical properties of the concrete

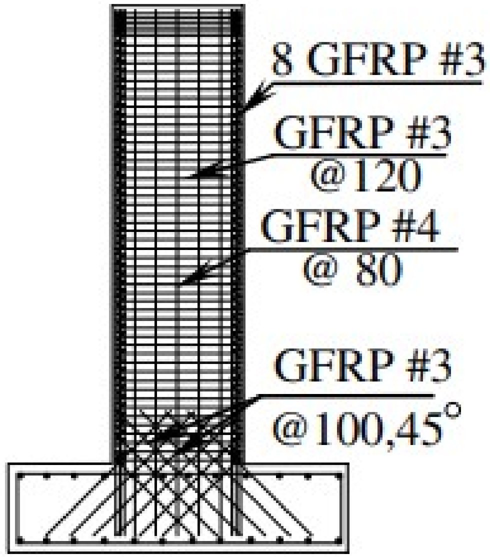

(a) Elevation view of G10 [13]

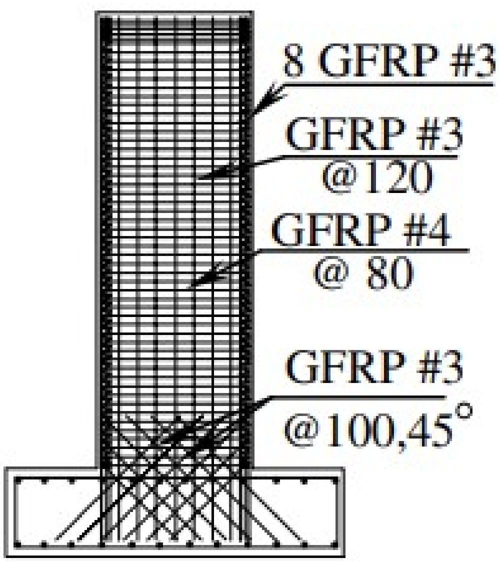

(b) Elevation view of G12 [13]

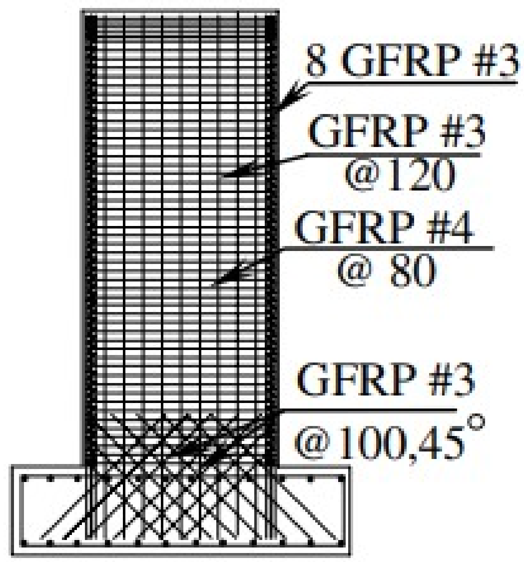

(c) Elevation view of G15 [13]

Figure 3.2: Elevation views of the walls reinforcements [13]

GFRP Mechanical properties					
		Rebar ϕ 10	Rebar ϕ 13	Spiral ties	
Area	A_f	71,3	126,7	71,3	mm^2
Tensile strength	f_{fu}	1412	1392	962	MPa
Modulus of elasticity	E_f	66,9	69,6	52	GPa
Ultimate strain	ϵ_{fu}	2,11	2	1,85	%

Table 3.2: Mechanical properties of the GFRP

3.1.2 Zhang & al (2019): GNW

The wall presented in this section corresponds to the one studied and tested by Q. Zhang & al (2019) [23].

Geometry

The dimensions of the wall are a height of 2400 mm, a length of 800 mm, and a width of 100 mm. The wall, therefore, has an aspect ratio of 3,7.

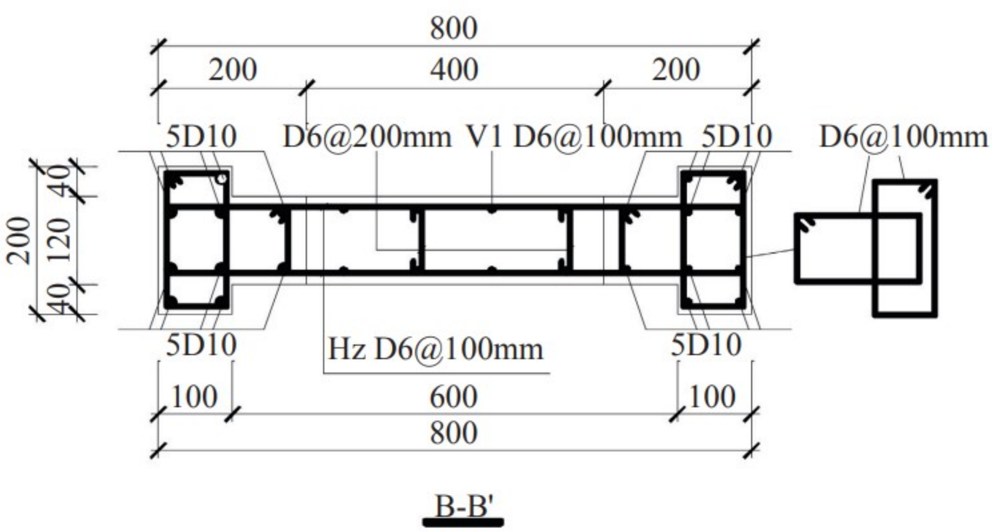

Figure 3.3: Cross section and reinforcement detailing of wall GNW [23]

For the longitudinal reinforcements, there are 5 GFRP bars in the ends with a diameter of 10 mm on each side. In the web, the vertical elements are 6 mm in diameter and spaced at 100 mm intervals. For horizontal reinforcement, there are 6 mm diameter stirrups placed every 100 mm at the ends. There are also transversal bars of 6 mm diameter spaced every 100 mm in the web and some others spaced every 200 mm. Figures 3.3 and 3.4 represent the reinforcements in the section and in the elevations.

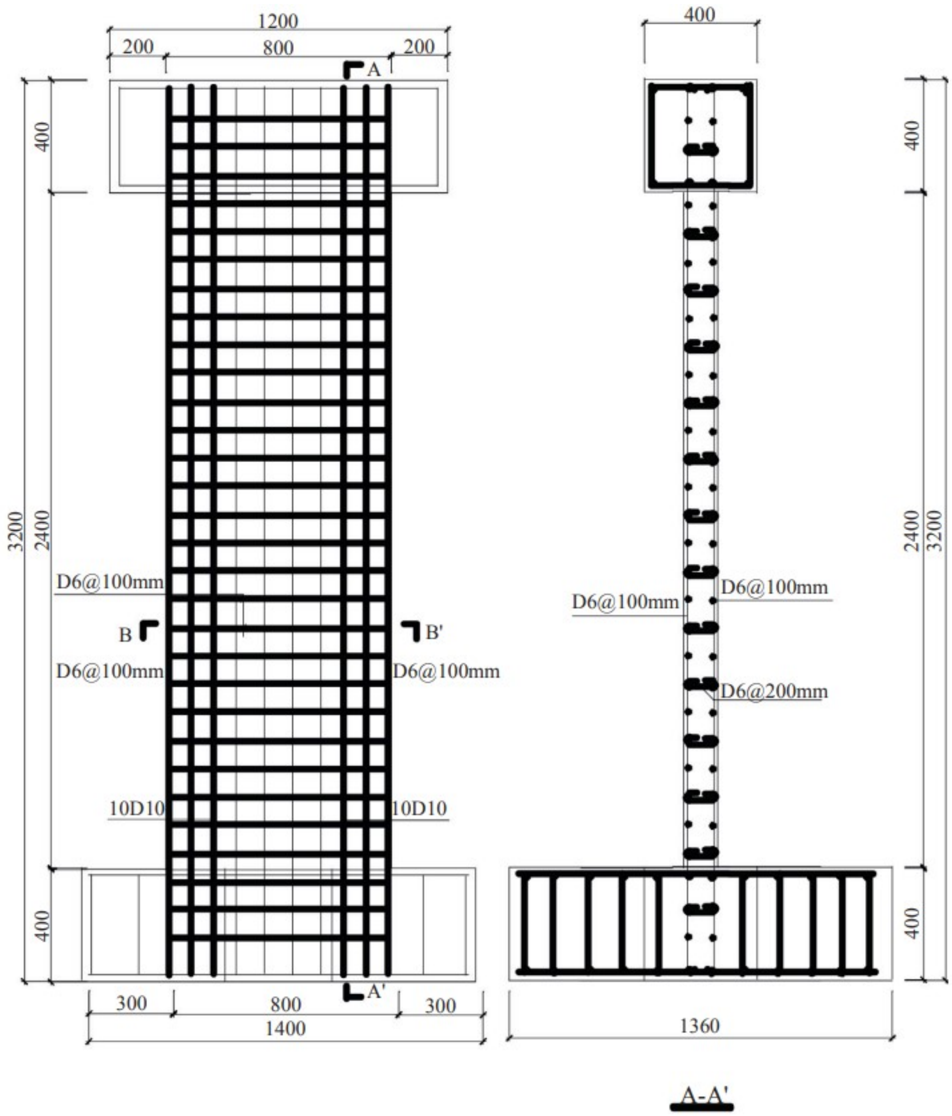

Figure 3.4: Elevation of the wall GNW [23]

Material properties

The two tables below 3.3 and 3.4 give the mechanical properties of concrete and GFRP bars. For the diagonal elements of the beam-truss model, the tensile strength of the concrete is assumed to be zero.

Concrete Mechanical properties			
		GNW	
Compressive concrete strength	f_c	25,9	MPa
Tensile concrete strength	f_t	2,8	MPa
Modulus of elasticity	E_c	23,9	GPa
Strain at peak stress	ϵ_c	0,2	%

Table 3.3: Mechanical properties of the concrete

GFRP Mechanical properties				
		Rebar ϕ 6	Rebar ϕ 10	
Area	A_f	28,3	78,5	mm^2
Tensile strength	f_{fu}	1191,3	794,9	MPa
Modulus of elasticity	E_f	50,3	45,8	GPa
Ultimate strain	ϵ_{fu}	2,2	1,8	%

Table 3.4: Mechanical properties of the GFRP

3.2 Modelling approaches chosen on Seismostruct

This section presents different numerical models to represent our FRP-RC walls. Each model is made up of nodes and links between them to form walls. These models are applied on the G10 wall and compared with the force-displacement curve. Lastly, the selected model will be employed for all walls in section 3.4.

3.2.1 Stick model

This first one-dimensional model represents the wall with a single element. A simple wall is therefore modeled with two nodes at its upper and lower ends and a vertical element that makes the connection. A reinforced concrete wall element with a rectangular cross-section is used. The forces are then simply applied to the top node of the structure.

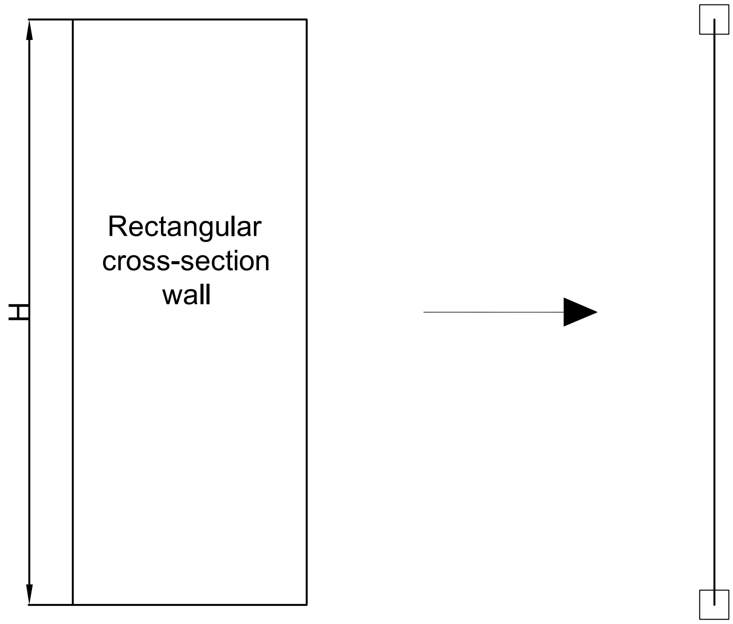

Figure 3.5: Stick model of a rectangular cross-section wall like G10

As an advantage, this model is simple and time efficient. A disadvantage is that it does not simulate the distribution of internal lateral forces well when dealing with a non-planar wall [5]. This will not be a problem for the examples discussed later in this chapter, as all the walls have a rectangular cross-section.

3.2.2 Wide-column model

The wide-column model consists of separating the wall into different pieces along its height, which are modeled by vertical elements placed in the center of the cross-section. The different parts are connected by horizontal rigid links to allow the structure to deform uniformly. Figure 3.6 shows an example of this model for a simple wall with a rectangular cross-section.

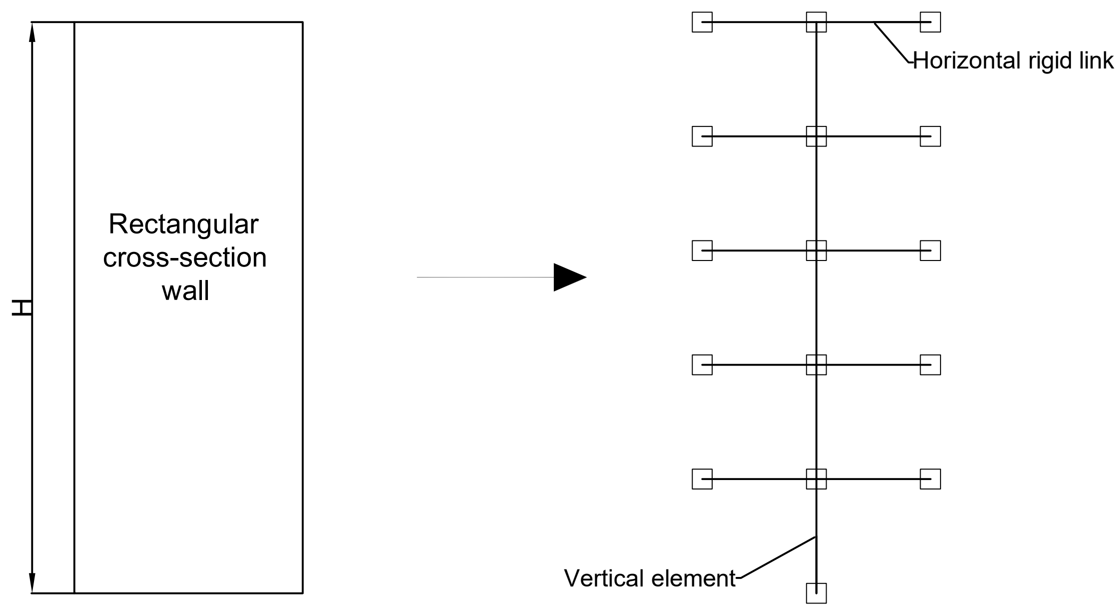

Figure 3.6: Wide-Column model of a rectangular cross-section wall like G10

This model concentrates the shear forces at the rigid links, which introduces a parasitic moment. This moment increases the displacements of the model, which then appears more flexible [16]. The spacing between the rigid links has an influence on these parasitic moments that one aims to limit. There are various guidelines: B. Stafford-Smith and al [21], for example, suggest limiting the spacing between rigid links to 1/5 of the height of the wall.

The main disadvantage of this type of model is the great freedom left to the designer when it comes to design choices such as the number of wall subdivisions, the space between the rigid links, and the characteristics of the latter [16].

3.2.3 Beam-truss model

The third model called the beam-truss model involves the use of beam elements and truss elements. The wall section is divided into several parts where the vertical and horizontal elements are beam elements and the diagonals are non-linear truss elements. The beam elements take into account the concrete and GFRP reinforcement included in each section. However, as the diagonals are used to model the compressive behavior of concrete, the truss elements only include concrete in tensile strength. This beam-truss model permits the simulation of the flexure-shear interaction for the planar RC walls. Figure 3.7 shows the grid of the beam-truss model.

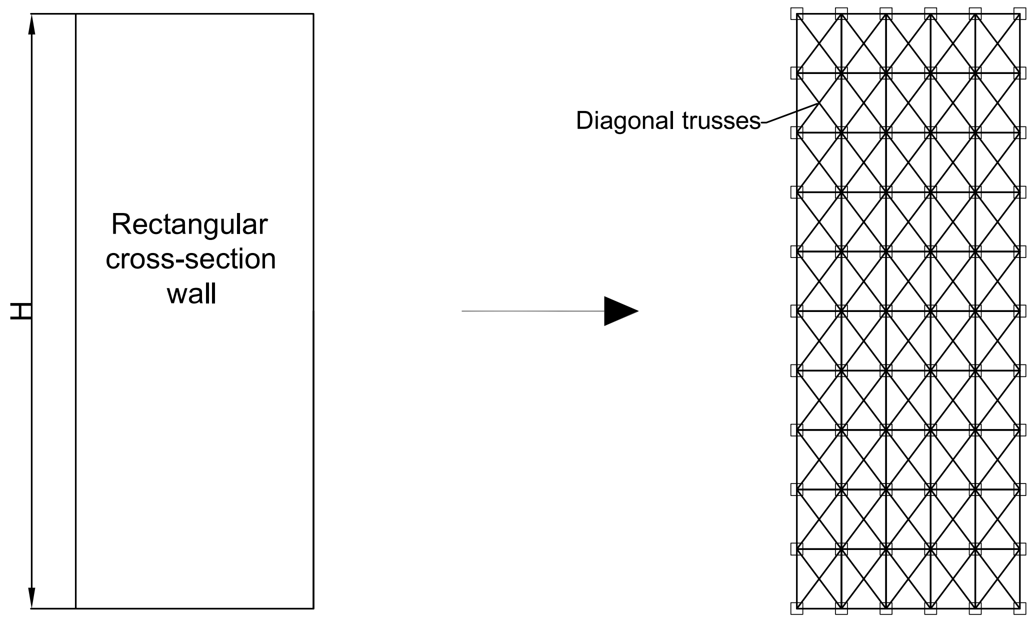

Figure 3.7: Beam-Truss model of a rectangular cross-section wall like G10

There are different rules governing the subdivision of the wall, in particular concerning the angle of the diagonals. Y. Lu & al [11] have proposed a formula to evaluate this angle, taking into account the shear force capacity and the reinforcements:

$$45^\circ \leq \theta_d = \tan^{-1}\left(\frac{V_{max}}{f_{y,t}\rho_t t_w d}\right) \leq 65^\circ \tag{3.1}$$

In this expression, V_{max} is the maximum shear force capacity, $f_{y,t}$ is the yield strength of the transverse reinforcement, ρ_t is the transverse reinforcement ratio, t_w is the thickness of the wall, d is the distance between the two outer vertical elements. The value of V_{max} can be found in the results of the experiment. If this data is not available, proceeding by iteration is needed, imposing an initial θ value. Using this angle θ, the effective width (b_{eff}) of the truss diagonal elements using the formula can be found:

$$b_{eff} = asin(\theta_d) \tag{3.2}$$

3.2.4 Comparison

Figure 3.8 shows the comparison of pushover analysis results for the 3 models presented earlier: stick model, wide-column model, and beam-truss model.

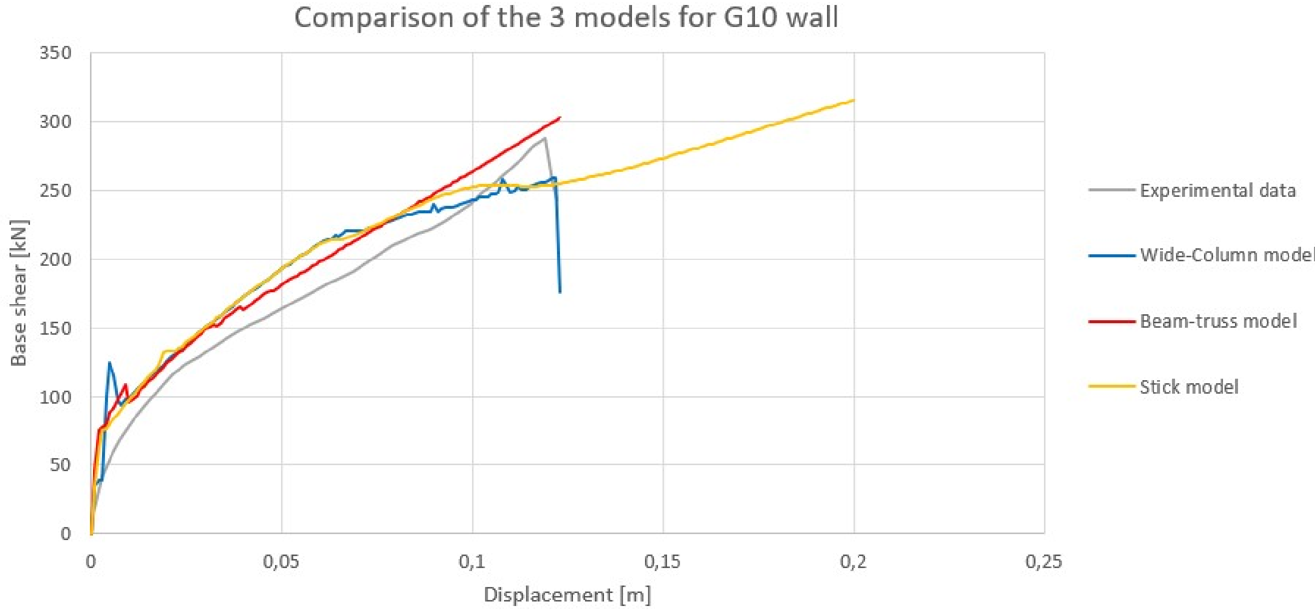

Figure 3.8: Force-displacement curve of stick model, wide-column model and beam-truss model for the G10 wall

The models remain similar up to a top displacement of around 80mm. Up to this value, the models remain above the experimental curve and therefore overestimate the base shear value. Thereafter, the models diverge and it has been seen that it is the red curve that is closest to the actual behavior given by the grey curve. Indeed, at the point of failure, the beam-truss model exhibits an error of approximately 5% for the base shear and 3% for the displacement. While the Wide-column model and stick model, in contrast, demonstrate errors on the order of 10% for the base shear. It is also observed that the stick model completely overshoots the experimental results, which doesn't seem surprising since it is the simplest model and therefore presumably the least accurate. Hence, there is a tendency to believe that the beam-truss model is better suited for the numerical representation of such walls. This is why, in the remainder of this work, all the walls will be modeled in this way.

3.3 Types of materials chosen on Seismostruct

Seismostruct provides different types of materials to represent their non-linear behaviour. In this report, the Mander & al [12] non-linear concrete model is always used with the corresponding mechanical properties of each wall.

2 models of FRP bars will be discussed and compared: Trilinear FRP model (Table 3.5) and Elastic material model (Table 3.6). To illustrate the influence of these two models, the results obtained for the G10 wall are presented and compared later in this section.

3.3.1 Trilinear FRP model

This first model consists of a uniaxial model which considers that there is no compressive strength. It is defined by the following 3 parameters:

- Tensile strength f_t of the FRP material, its value usually oscillates between 1900 and 4800 MPa for glass fibers. The default value is 3000 MPa [3].
- Initial stiffness E_1: initial elastic stiffness of the FRP confining material. Its value usually oscillates between 70 and 90 GPa for glass fibers and the default value is 300 GPa [3].
- Post-peak stiffness E_2, the default value is -500 GPa.

Table 3.5 shows the values for the GFRP rebars used for the G10 wall [13].

	Symbol	value
Tensile strength	f_t	1412 MPa
Initial stiffness	E_1	66,9 GPa
Post-peak stiffness	E_2	-500 GPa

Table 3.5: Material properties of G10 wall

Figure 3.9 shows the behavior of the material. The model aims to represent the mechanical properties of FRP rebars in a simplified manner. This is why its shape might not necessarily reflect a trilinear behavior, despite the implications of its name.

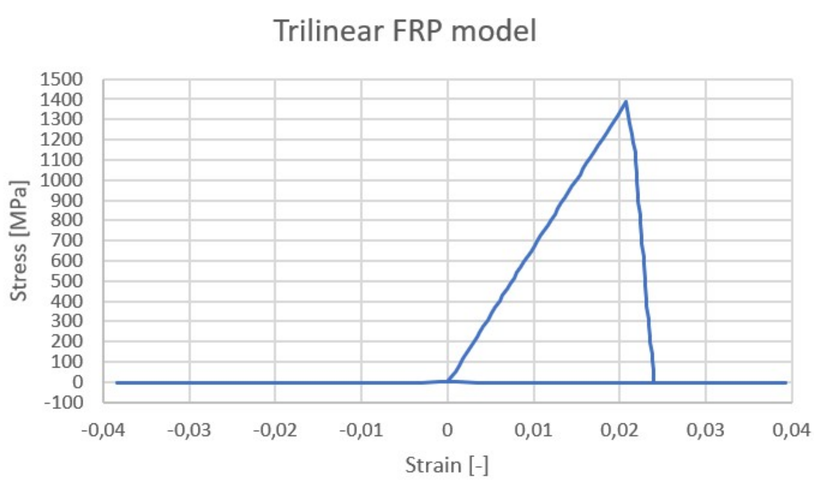

Figure 3.9: Trilinear FRP model for G10 wall

3.3.2 Elastic material model

The second model is an uniaxial model which considers a symmetrical behaviour in tension and compression. It is defined by the following two parameters:

- Modulus of elasticity E_s: the default is 200 GPa [3].
- Tensile/compression strength

In the case of wall G10, here are the following values:

	Symbol	value
Modulus of elasticity	E_s	66,9 GPa
Tensile/compression strength	$f_{t,c}$	1412 MPa

Table 3.6: Material properties of G10 wall

The curve of the material behavior is shown in figure 3.10.

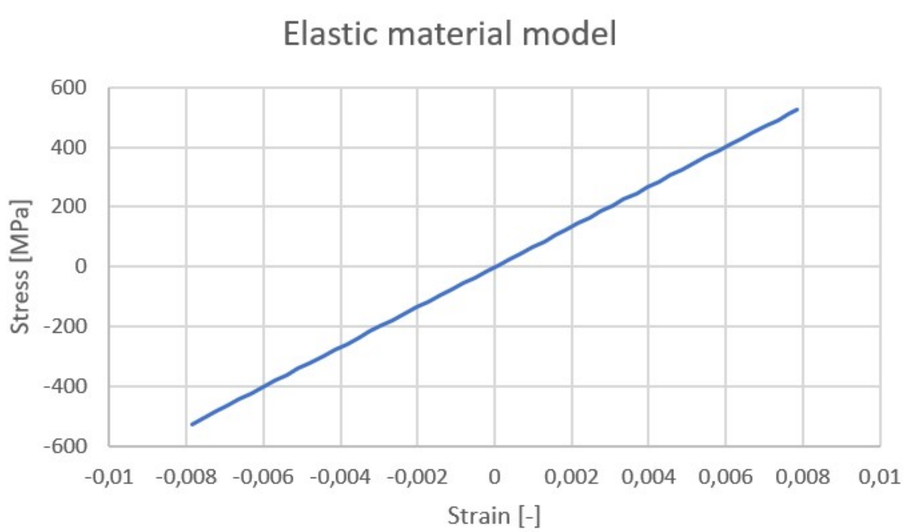

Figure 3.10: Elastic material model for G10 wall

3.3.3 Comparison

Figure 3.11 shows the use of these 2 models in the modeling of wall G10. The grey curve represents the experimental results obtained by Mohamed & al [13].

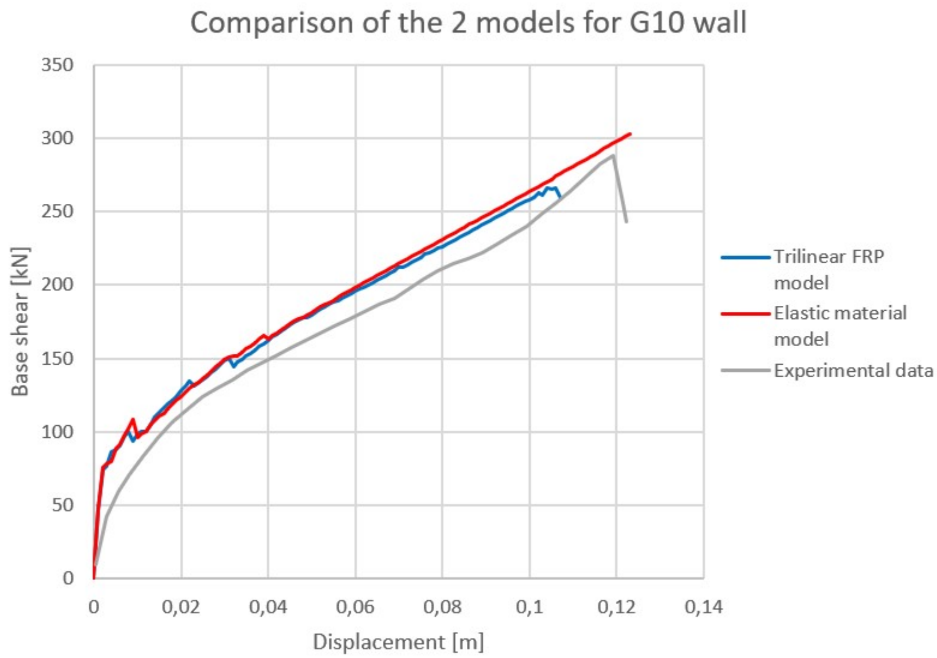

Figure 3.11: Trilinear FRP model versus elastic material model for G10 wall

As can be seen from the comparison graphic, the start of the curves for the two models is fairly similar. However, the end of the curves differ. On the one hand, the trilinear FRP model seems to underestimate the base shear capacity, which could be because this model considers that FRP bars have no compressive strength. On the other hand, the elastic model appears to somewhat overestimate the base shear value, probably because it assumes a compressive strength equal to the tensile strength, whereas, in reality, it is of the order of 50% of the tensile strength for GFRP bars.

For the rest of this thesis, all the walls will then be modeled with the elastic material model since it seems to be closer to the experimental results and to the real behavior of the rebars.

3.4 Simulation of wall response with SeismoStruct

In this section, the elastic material model and beam-truss model are applied to the four presented walls. The results will confirm or not the accuracy of our model.

3.4.1 Mohamed & al (2013): G10, G12, G15

The figures 3.12, 3.13, 3.14 show the plan views of the beam-truss models. The wall section is divided into 7, 9, and 11 parts for walls G10, G12, and G15 respectively. In all three cases, the sections representing the extremities are the same and have the following dimensions: 200 mm x 200 mm. The proportions of the other parts inside the section vary according to the wall and the position of the reinforcement.

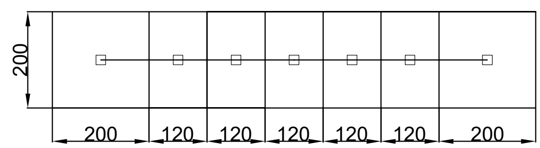

Figure 3.12: Beam-truss model: plan view of G10

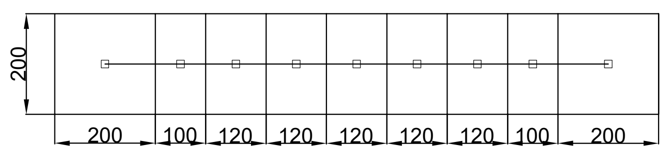

Figure 3.13: Beam-truss model: plan view of G12

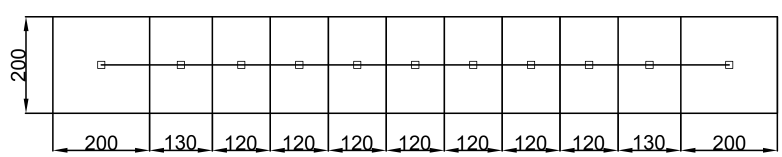

Figure 3.14: Beam-truss model: plan view of G15

Figure 3.15 shows elevation views of the beam-truss models for the 3 walls. They are all divided into 15 pieces along the height. The vertical and horizontal elements are inelastic displacement-based frame elements, while the diagonals are inelastic truss elements.

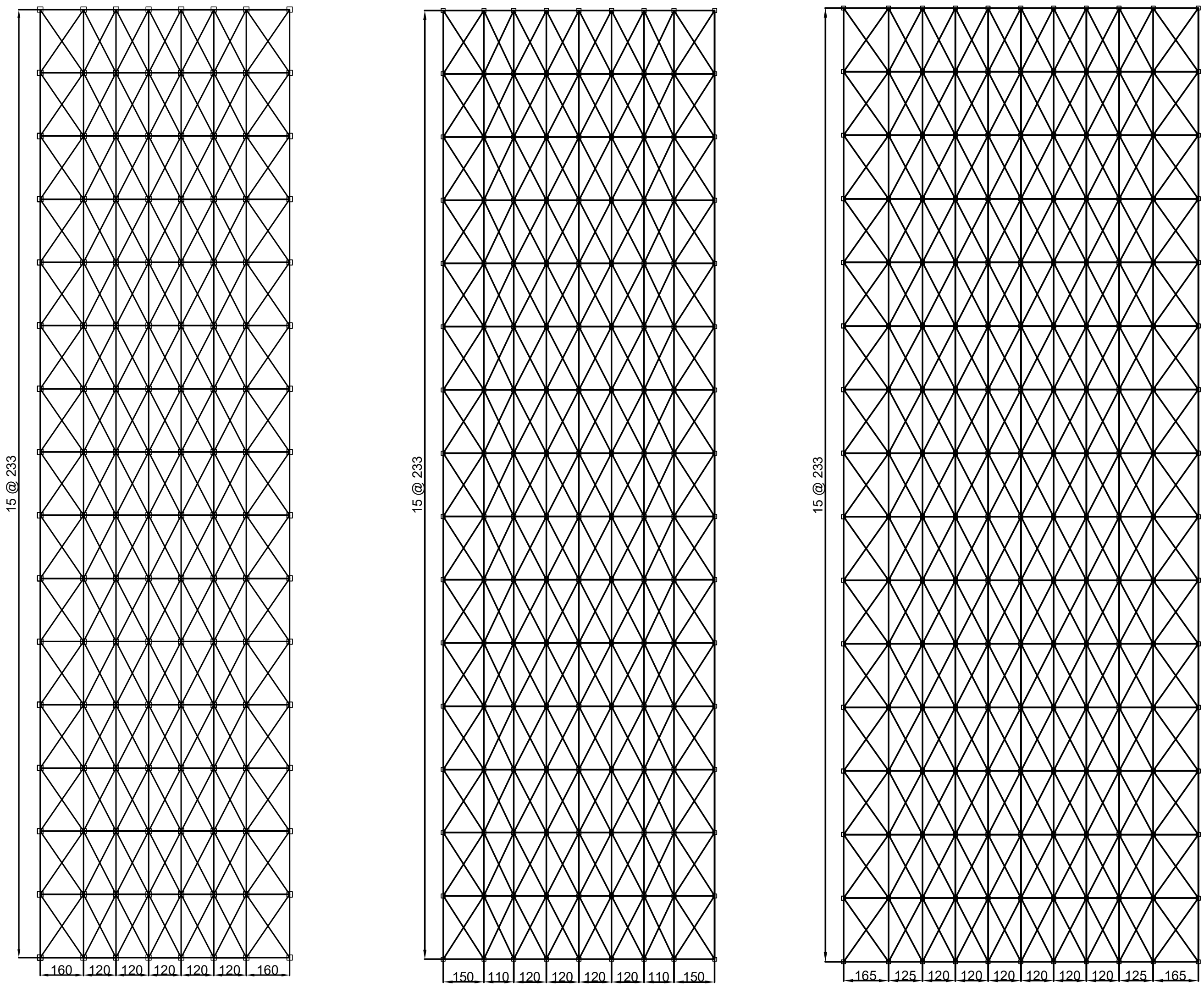

(a) Beam-truss model: elevation view of G10

(b) Beam-truss model: elevation view of G12

(c) Beam-truss model: elevation view of G15

Figure 3.15: Elevation views of the 3 beam-truss models

The axial loads applied to the walls during the experiments by Mohamed & al [13] are defined in the table 3.7. These axial loads are distributed to all the upper nodes of our model.

Walls	G15	G12	G10
Axial loads [kN]	838	672	560

Table 3.7: Axial load (7% of the axial capacity) applied on each wall. $N = 0,07 \cdot b_w \cdot l_w \cdot f_c$ [kN] [13].

G10: simulation results

A static pushover analysis was performed on the beam-truss model of the G10 wall. The force-displacement curve was obtained where the displacements correspond to those of the top of the wall.

Figure 3.16: G10: Force-displacement curve

In Figure 3.16, the blue curve corresponds to the results of the beam-truss model, while the grey curve corresponds to the experimental results. It can be seen that the blue curve is above the grey one all along and therefore overestimates the base shear values. This may be due to the use of the elastic material model which assumes a compressive strength equal to the tensile strength, whereas, in reality, it is of the order of 50% of the tensile strength for GFRP bars. However, the two curves always remain fairly close. At failure, the numerical model predicts a base shear value of 303 kN, whereas Mohamed & al [13] measured a value of 289 kN. This gives an error of around 5%.

G12: simulation results

In Figure 3.17, the blue curve corresponds to the results of the beam-truss model, while the grey curve corresponds to the experimental results. It can be seen that the blue curve is higher than the grey curve up to around 80 mm and therefore overestimates the shear values from the base up to this point. Then the trend reverses and the beam-truss model underestimates the base shear. However, the two curves always remain fairly close. At

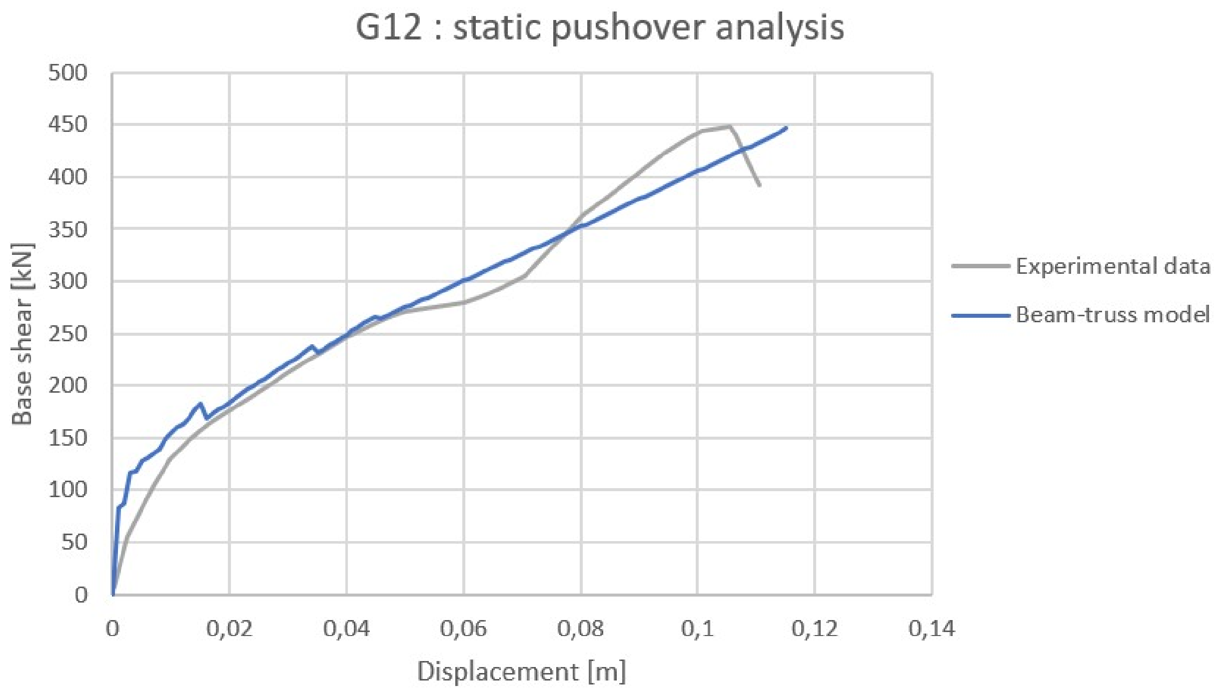

Figure 3.17: G12: Force-displacement curve

failure, the numerical model predicts a base shear value of 447 kN, whereas Mohamed & al [13] measured a value of 449 kN. This gives an error of around 0,5%.

G15: simulation results

In Figure 3.18, the blue curve corresponds to the results of the beam-truss model, while the grey curve corresponds to the experimental results. It can be seen that the blue curve is above the grey one all along and therefore overestimates the base shear values. However, the two curves always remain fairly close. At failure, the numerical model predicts a base shear value of 618 kN, whereas Mohamed & al [13] measured a value of 586 kN. This gives an error of around 5,5% (see Table 3.8).

Table 3.8 groups together the values obtained during the simulations and compares them with those obtained experimentally.

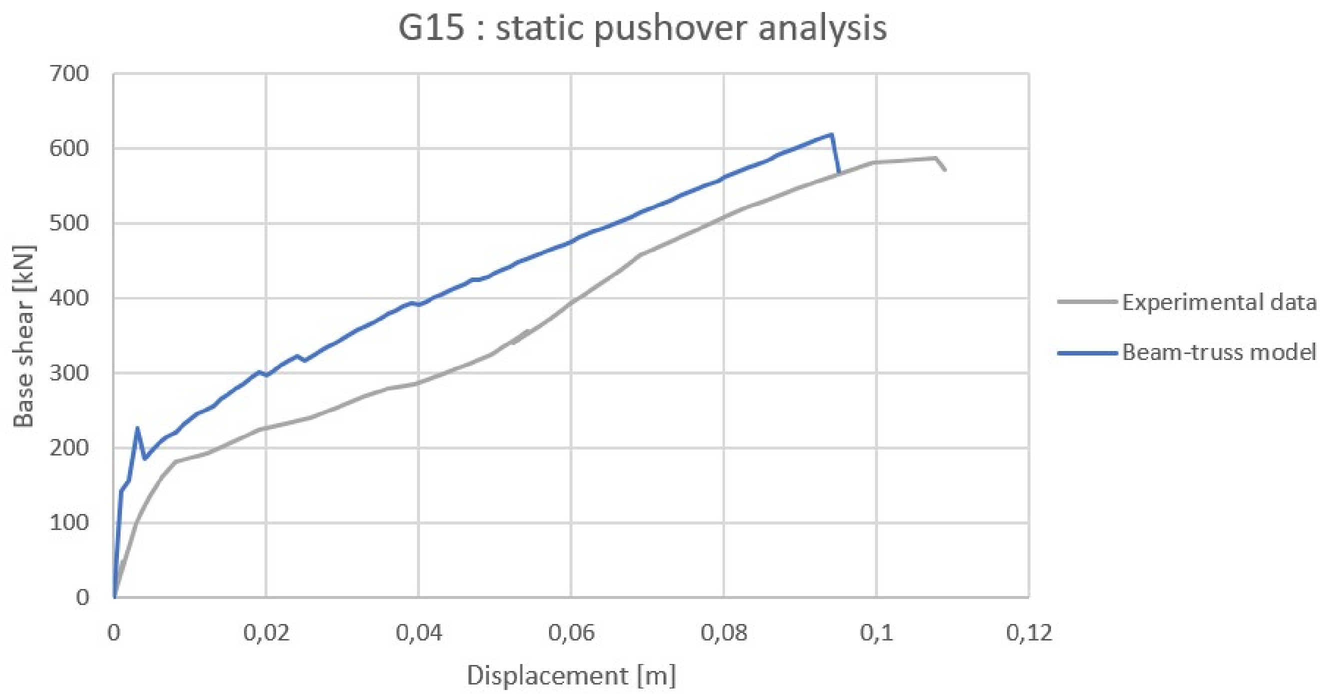

Figure 3.18: G15: Force-displacement curve

		G10	G12	G15
Ultimate lateral load measured	V	289 kN	449 kN	586 kN
Predicted base force at concrete crushing failure	V_b	303 kN	447 kN	618 kN
Error		5,14%	0,45%	5,51 %

Table 3.8: Comparison between the measured ultimate lateral load at concrete crushing and the predicted base force at failure.

3.4.2 Zhang & al (2019): GNW

Figure 3.19a shows the plan view of the beam-truss model. The wall section is divided into 8 parts. The sections representing the extremities are the same and have the following dimensions: 200 mm x 100 mm. The other parts of the section have dimensions of 120 mm x 100 mm.

Figure 3.19b shows the elevation view of the beam-truss model. It is divided into 14 pieces along its height. The vertical and horizontal elements are inelastic displacement-based frame elements, while the diagonals are inelastic truss elements.

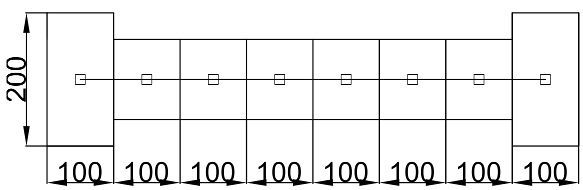

(a) Beam-truss model: plan view of GNW

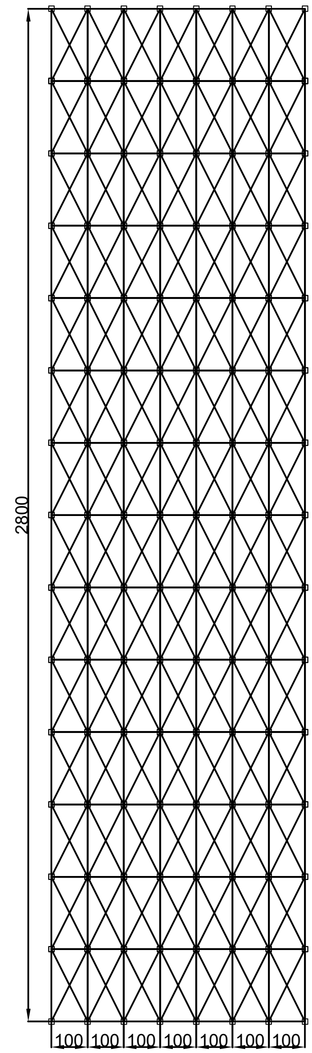

(b) Beam-truss model: elevation view of GNW

Figure 3.19: Elevation and plan views of the beam-truss model

The axial load applied to the wall during the experiments by Zhang & al [23] is defined in the table 3.9. This axial load is distributed to all the upper nodes of our model.

Wall	GNW
Axial load [kN]	672

Table 3.9: Axial load (24% of the axial capacity) applied on the wall. $N = 0,24 \cdot b_w \cdot l_w \cdot f_c$ [kN] [23]

.

GNW: simulation results

A static pushover analysis was performed on the beam-truss model of the GNW wall. The force-displacement curve was obtained where the displacements correspond to those of the top of the wall.

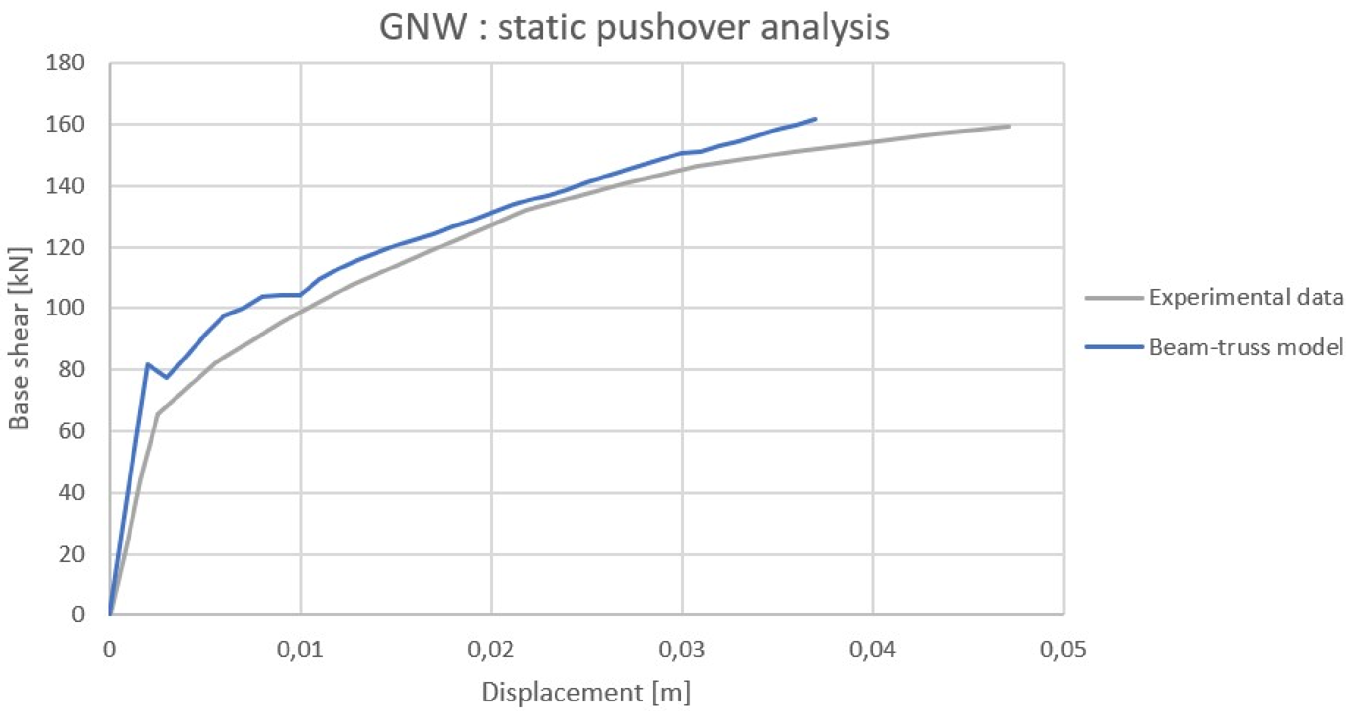

Figure 3.20: GNW: Force-displacement curve

In Figure 3.20, the blue curve corresponds to the results of the beam-truss model, while the grey curve corresponds to the experimental results. It can be seen that the blue curve is above the grey one all along and therefore overestimates the base shear values. However, the two curves always remain fairly close. At failure, the numerical model predicts a base shear value of 162 kN, whereas Zhang & al [23] measured a value of 159 kN. This gives an error of around 1% (see Table 3.10).

		GNW
Ultimate lateral load measured	V	159 kN
Predicted base force at concrete crushing failure	V_b	162 kN
Error		1,37%

Table 3.10: Comparison between the measured ultimate lateral load at concrete crushing and the predicted base force at failure.

3.5 Simulation of wall response with Response 2000

3.5.1 Response 2000 software

The Response 2000 software has been used mainly to predict the resisting moment of the modeled wall. This program performs a sectional analysis of the model. The material's properties, the section of the wall, the position, and the diameter of the rebars have to be implemented. With this information and the loads applied on the specimen, Response 2000 can provide predictions on the structure response, namely on the moment, the strain, and stress evolution during the loading.

For instance, Figure 3.21b illustrates the moment prediction provided by Response 2000 for the G10 wall from the study conducted by Mohamed & al. in 2013 [13].

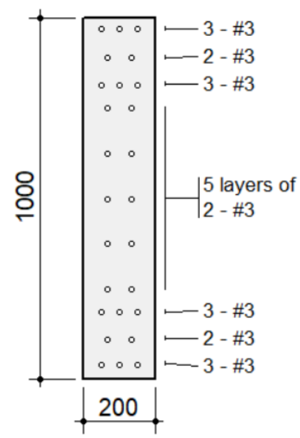

(a) Shape of wall G10. Introduced data in Response 2000.

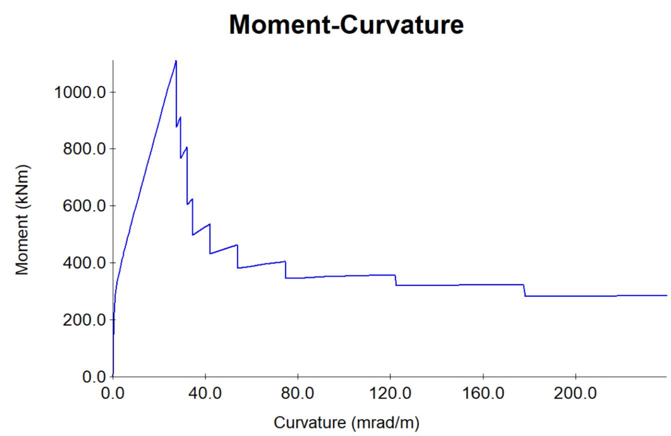

(b) Moment curvature diagram of G10 predicted by Response 2000 by performing the sectional analysis.

Figure 3.21: Results from Response 2000 for G10

3.5.2 Application to walls G10, G12, G15 (Mohamed & al, 2013) and GNW (Zhang & al, 2019)

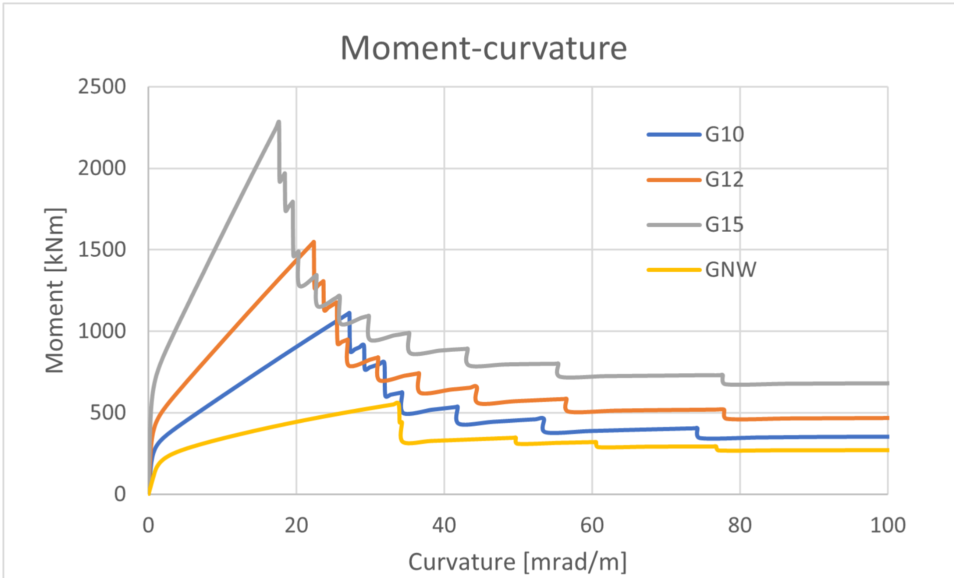

Figure 3.22: Moment curvature curve from Response 2000 for walls G10, G12, G15 and GNW. The moments predicted at failure of the rebars are respectively: 1112 kNm, 1550 kNm, 2280 kNm, and 556 kNm.

As depicted in Figure 3.22, according to Response 2000, the failure mode for G10, G12, and G15 is brittle, suggesting a failure occurring within the GFRP rebars. However, during the experimental tests of Mohamed & al (2013) [13], the actual failure is observed to occur due to concrete crushing. This discrepancy can be attributed to the simple definitions of ultimate compressive and tensile strains utilized by Response 2000, which may diverge significantly from the observed strain values. Particularly, a concrete failure can be complicated to determine with a sectional analysis due to its ductile behavior.

For GNW, the failure mode is predicted to be concrete crushing. Indeed, approaching the ultimate strength, the response seems to become ductile. Moreover, the strain in the concrete at failure (8,9 mm/m) is above the ultimate strain of the concrete (4,2mm/m)[1]. The Response 2000 prediction agrees with the mode of failure observed during the experimentation test of Zhang & al (2019) [23].

[1]These data are calculated by Response 2000

Wall	Base shear	Measured base shear	Error
G10	318 kN	289 kN	+9%
G12	443 kN	449 kN	-1%
G15	651 kN	486 kN	+25%
GNW	232 kN	158 kN	+32%

Table 3.11: The base shear derived from Response 2000 (see figure 3.22), the base shear measured during the tests of Mohamed & al (2013) [13] and Zhang & al (2019) [23] and the percentage of error between the two. The base shear is obtained by dividing the resisting moment given by Response 2000 by the height of the walls (L = 3,5m for G10, G12, and G15 and L= 2,4m for GNW).

As highlighted in Table 3.11, Response 2000 generally provides a base shear value that is relatively (+16% on average) close to the experimentally measured limit strength but tends to overestimate it. Nevertheless, when employing simple definitions for the ultimate tensile and compressive strains in GFRP and concrete, respectively, Response 2000 failed to accurately predict the failure modes of rupture.

Chapter 4

Design methods following the codes

The purpose of this section is to follow guidelines in codes to design a structure with FRP reinforcement. Several codes already exist. Notably, the next generation of Eurocode 2 will incorporate an annex dedicated to FRP design [6]. The Association Française de Génie Civil (AFGC) has formulated a scientific and technical document on the application of FRP as reinforcement [7]. These two references will primarily serve as the basis for developing the flexural and shear design. Subsequently, these methods will be applied on experimentally tested walls: G10, G12, and G15 from the study by Mohamed et al. (2013) [13], as well as GNW from the study by Zhang et al. (2019) [23].

4.1 Pure bending design

4.1.1 General method

This section follows the AFGC guide [7] and S. Singh (2014) [19] concerning the development of the methods. A priori, this method mainly concerns beams. However, the AFGC guide [7] performs this method on an embedded wall where it is used to determine the specifications of one layer of reinforcement needed in a wall. In this work, the method is extended to fully reinforced walls, by making some adjustments. The main differences between a wall design and a beam design are the consideration of longitudinal reinforcement and confinement. To account for all the longitudinal reinforcements that act in tension, the value of the effective depth (d) will be manually calculated based on the stress state of the section (see Excel file, access in section 1.3). Regarding confinement, the stress-strain curve will be adjusted for confined concrete using the Mander method [12] (see section 4.1.2)

Here are the assumptions for the flexural design of RC members using the ultimate stress design method [7]:

- **H1** Plain section remains plain after deformation (Bernoulli-Euler assumption). The strain is proportional to the distance from the neutral axis.

- **H2** There is a perfect bond between the concrete and the rebars such that they incur the same deformation.

- **H3** The tensile strength of the concrete is neglected.

- **H4** The total sectional area of the rebars can be reduced to an equivalent area situated in the center of gravity of all the rebars.

- **H5** The concrete attains failure when it reaches maximum compressive strain ε_{cu2}. The concrete is considered elastic-plastic and follows the known behavior law described on Figure 4.1.

- **H6** The displacement of the FRP is limited to the design rupture strain ε_{fRd}. The behavior of GFRP is assumed to be elastic, see Figure 4.2

Note that the reinforcing material does not influence the first five assumptions [15].

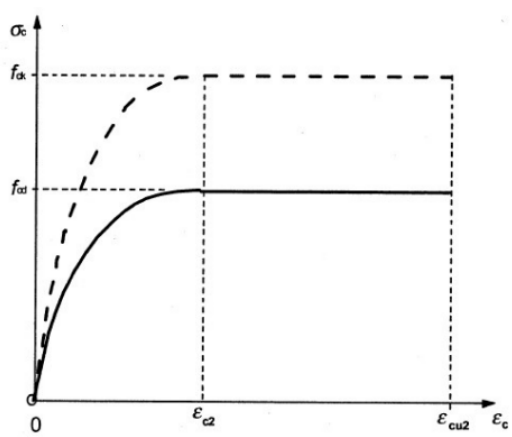

Figure 4.1: Strain-stress relation of concrete in compression [7]. The dashed curve pertains to confined concrete.

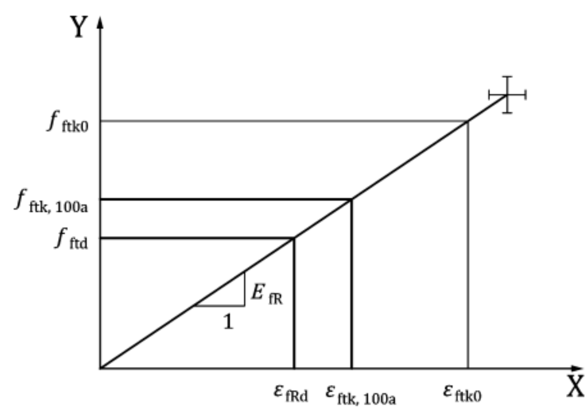

Figure 4.2: Strain-stress relation of FRP [6]

Due to the flexion, a part of the section will be under tension and the other under compression. The concrete will endure compression and the reinforcement will work in tension because of their mechanical properties. At failure, either the concrete will crush in compression or the GFRP rebars will break in tension[1]. To control the failure mode, the area of GFRP rebars that balance the compression concrete zone has to be determined [7]. At

[1]These two situations can also occur at the same time.

failure, the capacity of the element is unable to withstand the demand, so our condition for the design is:

$$M_{Rd} > M_{Ed} \tag{4.1}$$

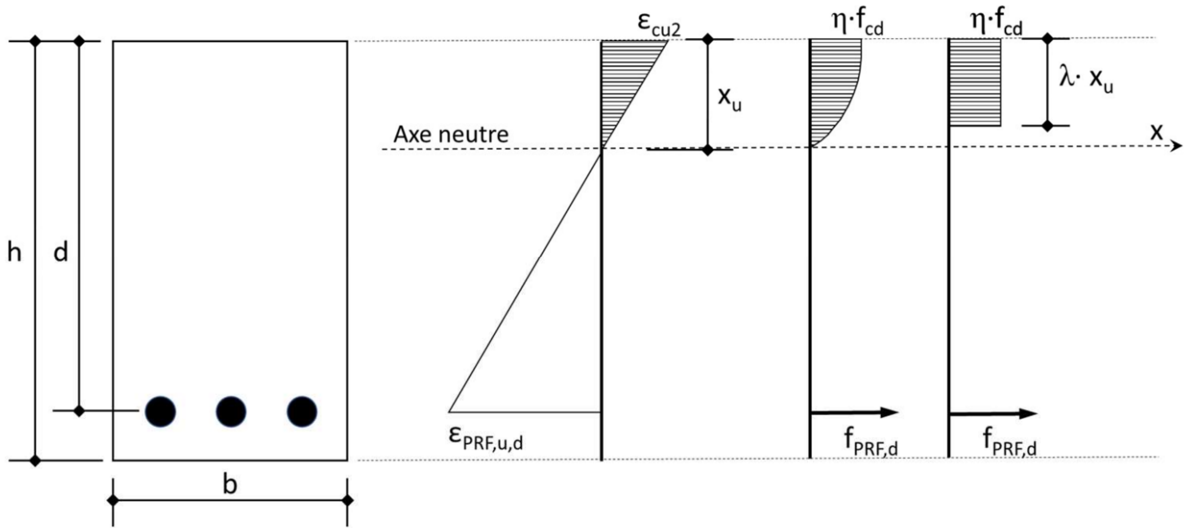

Figure 4.3: Balanced section of RC beam [7]

The ratio of reinforcement is defined as:

$$\rho_f = \frac{A_f}{A_{c,red}} \tag{4.2}$$

with

A_f	:	Area of longitudinal GFRP reinforcement
$A_{c,red}$	:	Reduced area of concrete ($= bd$)

It is also possible to define a *balanced reinforcement ratio*: $\rho_{f,b}$. Looking at the configuration of the balanced section (Figure 4.3), considering the inner forces, **H1** and **H2** can be computed:

$$\rho_{f,b} = \frac{\eta f_{cd} \lambda x_u}{d f_{f,d}} \tag{4.3}$$

where

η : $= 1$

λ : $= 0{,}8$

d : the effective depth, the distance between the extreme compressed fiber and the center of gravity of the rebars in tension.

x_u : the neutral axis at ultimate state.

$f_{f,d}$: the design GFRP tensile strength.

f_{cd} : the design concrete compression strength.

x_u is easily computed:

$$x_u = \frac{\varepsilon_{cu2}}{\varepsilon_{cu2} + \varepsilon_{f,u,d}} d \tag{4.4}$$

With this relation, the expression 4.3 can be re-written as:

$$\rho_{f,b} = \frac{\eta f_{cd} \lambda}{f_{f,d}} \frac{\varepsilon_{cu2}}{\varepsilon_{cu2} + \varepsilon_{f,u,d}} \tag{4.5}$$

Case 1: concrete crushing failure $\rho_f > \rho_{f,b}$ The section is over-reinforced. The failure will occur in the concrete in compression when the deformation reaches ε_{cu2}. By **H2**, the resisting moment can be expressed as:

$$M_{Rd} = A_f \cdot E_f \cdot \varepsilon_f \left(d - \frac{\lambda}{2} x\right) = \lambda \cdot x \cdot \eta \cdot f_{cd} \cdot b \left(d - \frac{\lambda}{2} x\right) \tag{4.6}$$

To compute this, the deformation of the GFRP needs to be determined when $\varepsilon_c = \varepsilon_{cu,2}$ and the position of the neutral axis.

$$\rho_f = \frac{A_f}{A_{c,red}} > \frac{\eta f_{cd} \lambda}{d E_f \varepsilon_f} \frac{\varepsilon_{cu2}}{\varepsilon_{cu2} + \varepsilon_f} d = \rho_{f,b} \tag{4.7}$$

Knowing this relation 4.7, the expression of ε_f can be deduced:

$$\varepsilon_f^2 + \varepsilon_{cu2} \varepsilon_f - \frac{A_{c,red}}{A_f} \frac{\eta \lambda f_{cd} \varepsilon_{cu2}}{E_f} > 0$$

$$\varepsilon_f = \sqrt{\frac{\varepsilon_{cu2}^2}{4} + \frac{\lambda \eta \varepsilon_{cu2} f_{cd}}{E_f \rho_f}} - \frac{\varepsilon_{cu2}}{2} < \varepsilon_{f,u,d} \tag{4.8}$$

The position of the neutral axis is now also known:

$$x = \frac{\varepsilon_{cu2}}{\varepsilon_{cu2} + \varepsilon_f} d \tag{4.9}$$

Case 2: failure due to GFRP rupture $\rho_f < \rho_{f,b}$. The section is under-reinforced. The failure will occur in the rebars in tension when the deformation reaches $\varepsilon_{f,u,d}$. By **H2**, the resisting moment can be expressed as:

$$M_{Rd} = \lambda \cdot x \cdot \eta \cdot f_{cd} \cdot b(d - \frac{\lambda}{2}x) = A_f \cdot f_{f,d}(d - \frac{\lambda}{2}x) \tag{4.10}$$

The position of the neutral axis is still unknown as well as the deformation of the concrete. If assuming that:

$$\varepsilon_{cu2} \geq \varepsilon_c = \left(\frac{\varepsilon_{f,u,d}}{\lambda \frac{\eta f_{cd}}{f_{f,d}\rho_f} - 1} \right) \geq \varepsilon_{c2} \tag{4.11}$$

Then the expression of the neutral axis is:

$$x = \frac{\varepsilon_c}{\varepsilon_c + \varepsilon_{f,u,d}} d \tag{4.12}$$

Conclusion With the value of the resisting moment, it is possible to determine if the element will resist or not to the applied forces.

4.1.2 Application to G10, G12, G15 and GNW

As for the numerical modeling, our method has been tested on specimens already tested in labs. Our design estimations will be compared here with the measured results of the test. Those specimens were already presented in chapter 3, see section 3.1 for the description of the specimens.

Note that in the context of an experiment, the safety factors linked to the degradation of materials over time or applied to reduce the value of the resistance were not taken into account (per security). Therefore, the resistance values used for the design are simply the average of the resistances obtained on a sample set f_c and $f_{f,u}$.

Mohamed & al (2013): G10, G12, G15 [13]

In these walls, the concrete is confined thanks to the boundary ties. Confinement will increase the compressive strength of the concrete. To consider the positive effect on the concrete, it has been decided to use the Mander stress-strain curve for confined concrete [12][2]. Therefore, the confined compressive strength of the concrete f_{cc} for G10, G12, and G15 is 83 MPa (see Figure 4.4).

[2]For more details about the applied Mander method, see Excel files available on the Drive (see section 1.3).

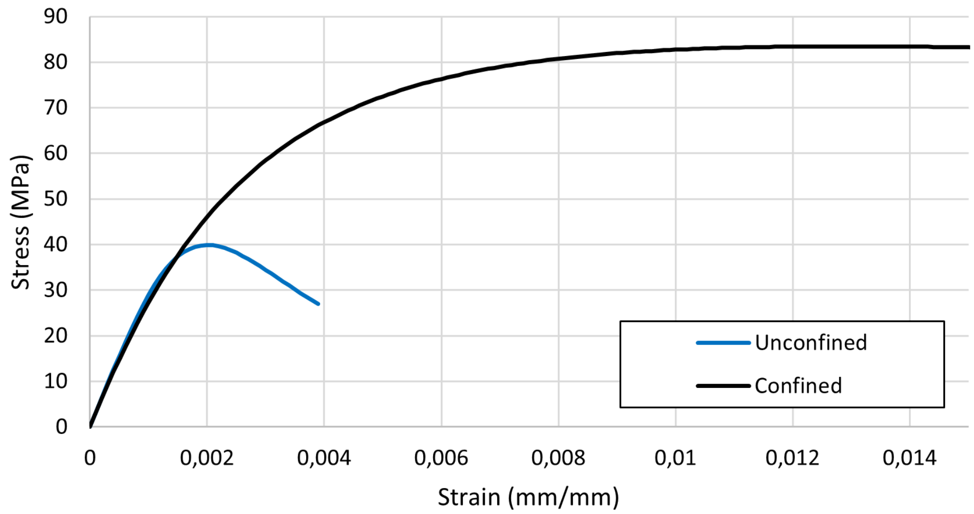

Figure 4.4: Mander stress-strain model for confined concrete G10, G12 and G15

G10 The ratio of reinforcement:

$$\rho_f = \frac{A_f}{A_{c,red}} = \frac{1414}{200 \cdot 10^3} = 0,71\%$$

The balanced reinforcement ratio:

$$\rho_{f,b} = \frac{\eta f_{cc} \lambda}{f_{f,u}} \frac{\varepsilon_{cu2}}{\varepsilon_{cu2} + \varepsilon_{f,u,d}} = \frac{1 \cdot 83 \cdot 0,8}{1412} \frac{0,35}{0,35 + 2,1} = 0,67\%$$

Since $\rho_f > \rho_{f,b}$, the failure will be dominated by concrete crushing. The strain at failure for the GFRP's rebars is:

$$\varepsilon_f = \sqrt{\frac{\varepsilon_{cu2}^2}{4} + \frac{\lambda \eta \varepsilon_{cu2} f_{cc}}{E_f \rho_f}} - \frac{\varepsilon_{cu2}}{2} = \sqrt{\frac{0,35^2}{4} + \frac{0,8 \cdot 1 \cdot 0,35 \cdot 83}{66,8 \cdot 0,71}} - \frac{0,35}{2} = 2,05\%$$

The position of the neutral axis is:

$$x = \frac{\varepsilon_{cu2}}{\varepsilon_{cu2} + \varepsilon_f} d = \frac{0,35}{0,35 + 2,03} 0,61 = 0,089m$$

The resisting moment will be:

$$M_{Rd} = \lambda \cdot x \cdot \eta \cdot f_{cc} \cdot b(d - \frac{\lambda}{2} x) = 0,8 \cdot 0,089 \cdot 1 \cdot 83 \cdot 0,2(0,61 - \frac{0,8}{2} 0,089) = 671kNm$$

At concrete crushing failure, the base shear equals:

$$V_b = \frac{M_{Rd}}{L} = \frac{671}{3,5} = 192kN$$

G12 The ratio of reinforcement:

$$\rho_f = \frac{A_f}{A_{c,red}} = \frac{1729}{240 \cdot 10^3} = 0,72\%$$

The balanced reinforcement ratio:

$$\rho_{f,b} = \frac{\eta f_{cc} \lambda}{f_{f,u}} \frac{\varepsilon_{cu2}}{\varepsilon_{cu2} + \varepsilon_{f,u,d}} = \frac{1 \cdot 83 \cdot 0,8}{1412} \frac{0,35}{0,35 + 2,1} = 0,67\%$$

Since $\rho_f > \rho_{f,b}$, the failure will be dominated by concrete crushing. The strain at failure for the GFRP's rebars is:

$$\varepsilon_f = \sqrt{\frac{\varepsilon_{cu2}^2}{4} + \frac{\lambda \eta \varepsilon_{cu2} f_{cc}}{E_f \rho_f}} - \frac{\varepsilon_{cu2}}{2} = \sqrt{\frac{0,35^2}{4} + \frac{0,8 \cdot 1 \cdot 0,35 \cdot 83}{66,8 \cdot 0,72}} - \frac{0,35}{2} = 2,03\%$$

The position of the neutral axis is:

$$x = \frac{\varepsilon_{cu2}}{\varepsilon_{cu2} + \varepsilon_f} d = \frac{0,35}{0,35 + 2,03} 0,71 = 0,104m$$

The resisting moment will be:

$$M_{Rd} = \lambda \cdot x \cdot \eta \cdot f_{cc} \cdot b(d - \frac{\lambda}{2} x) = 0,8 \cdot 0,104 \cdot 1 \cdot 83 \cdot 0,2(0,71 - \frac{0,8}{2} 0,104) = 926kNm$$

At concrete crushing failure, the base shear equals:

$$V_b = \frac{M_{Rd}}{L} = \frac{926}{3,5} = 265kN$$

G15 The ratio of reinforcement:

$$\rho_f = \frac{A_f}{A_{c,red}} = \frac{2042}{300 \cdot 10^3} = 0,68\%$$

The balanced reinforcement ratio:

$$\rho_{f,b} = \frac{\eta f_{cc} \lambda}{f_{f,u}} \frac{\varepsilon_{cu2}}{\varepsilon_{cu2} + \varepsilon_{f,u,d}} = \frac{1 \cdot 83 \cdot 0,8}{1412} \frac{0,35}{0,35 + 2,1} = 0,67\%$$

Since $\rho_f > \rho_{f,b}$, the failure will be dominated by concrete crushing. The strain at failure for the GFRP's rebars is:

$$\varepsilon_f = \sqrt{\frac{\varepsilon_{cu2}^2}{4} + \frac{\lambda \eta \varepsilon_{cu2} f_{cc}}{E_f \rho_f}} - \frac{\varepsilon_{cu2}}{2} = \sqrt{\frac{0,35^2}{4} + \frac{0,8 \cdot 1 \cdot 0,35 \cdot 83}{66,8 \cdot 0,68}} - \frac{0,35}{2} = 2,09\%$$

The position of the neutral axis is:

$$x = \frac{\varepsilon_{cu2}}{\varepsilon_{cu2} + \varepsilon_f} d = \frac{0,35}{0,35 + 2,09} 0,95 = 0,136m$$

The resisting moment will be:

$$M_{Rd} = \lambda \cdot x \cdot \eta \cdot f_{cc} \cdot b(d - \frac{\lambda}{2} x) = 0,8 \cdot 0,136 \cdot 1 \cdot 83 \cdot 0,2(0,95 - \frac{0,8}{2} 0,136) = 1620kNm$$

At concrete crushing failure, the base shear equals:

$$V_b = \frac{M_{Rd}}{L} = \frac{1620}{3,5} = 463kN$$

Zhang & al (2019): GNW [23]

In order to consider the positive effect of the confinement on the concrete resistance, the Mander stress-strain curve is also used for this wall [12]. Now, the confined compressive strength of the concrete f_{cc} for GNW is 30,8 MPa (see Figure 4.5).

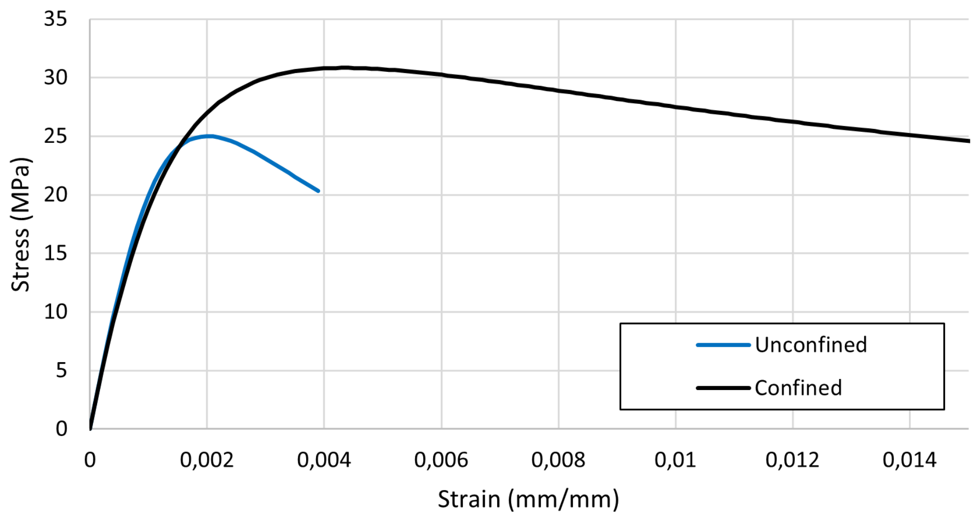

Figure 4.5: Mander stress-strain model for confined concrete GNW

GNW To obtain the moment of resistance analytically, the method exposed before is followed.

The ratio of reinforcement:

$$\rho_f = \frac{A_f}{A_{c,red}} = \frac{1012}{112 \cdot 10^3} = 0,90\%$$

The balanced reinforcement ratio:

$$\rho_{f,b} = \frac{\eta f_{cc} \lambda}{f_{f,u}} \frac{\varepsilon_{cu2}}{\varepsilon_{cu2} + \varepsilon_{f,u,d}} = \frac{1 \cdot 30,8 \cdot 0,8}{794} \frac{0,35}{0,35 + 1,8} = 0,50\%$$

Since $\rho_f > \rho_{f,b}$, the failure will be dominated by concrete crushing. The strain at failure for the GFRP's rebars is:

$$\varepsilon_f = \sqrt{\frac{\varepsilon_{cu2}^2}{4} + \frac{\lambda \eta \varepsilon_{cu2} f_{cc}}{E_f \rho_f}} - \frac{\varepsilon_{cu2}}{2} = \sqrt{\frac{0,35^2}{4} + \frac{0,8 \cdot 1 \cdot 0,35 \cdot 30,8}{45,8 \cdot 0,50}} - \frac{0,35}{2} = 1,28\%$$

The position of the neutral axis is:

$$x = \frac{\varepsilon_{cu2}}{\varepsilon_{cu2} + \varepsilon_f} d = \frac{0,35}{0,35 + 1,28} 0,59 = 0,126m$$

The resisting moment will be:

$$M_{Rd} = \lambda \cdot x \cdot \eta \cdot f_{cc} \cdot b_f(d - \frac{\lambda}{2}x) = 0,8 \cdot 0,126 \cdot 1 \cdot 30,8 \cdot 0,12(0,59 - \frac{0,8}{2}0,126) = 201kNm$$

The force at the base of the wall will be at concrete crushing failure:

$$V_b = \frac{M_{Rd}}{L} = \frac{201}{2,4} = 84kN$$

Comparison

Table 4.1 compares the calculated base force with the measured ultimate load for all the tested walls. It highlights the accuracy of the values calculated analytically.

		G10	G12	G15	GNW
Ultimate lateral load measured	V	289 kN	449 kN	586 kN	158 kN
Calculated base force at concrete crushing failure	V_b	192 kN	265 kN	463 kN	84 kN
Error		-34%	-41%	-21%	-47 %

Table 4.1: Comparison between the measured ultimate lateral load at concrete crushing and the calculated base force at concrete crushing failure.

The mode of failure is well predicted for all walls. But the method always underestimates the resisting moment with a quite large error (mean = 36%). This can be explained by the fact that the axial force that is applied on each wall was not considered. Indeed, the axial force subjects the concrete to compression, which in turn delays the occurrence of tensile concrete failure. This results in an increased resisting moment. To take into account the axial force, the bending with an axial force method must be developed (see section 4.2).

4.2 Bending with axial load design

4.2.1 General method

This section follows the AFGC guide [7] and the next generation of the EN2 [6] concerning the development of the method.

The assumptions for the bending with axial force are the same as for the flexural design (see section 4.1). There are assumptions that have to be added for the flexural design with an axial force of RC members using an interaction diagram:

- **H7** GFRP rebars are not considered in compression reinforcement.

- **H8** The axial load is assumed to act at the geometric centroid of the section.

Constructing the diagram of interaction has two principles: first determining all possible states of failure and then the resisting efforts N_{Rd} and M_{Rd} for each mode of rupture[7].

Table 4.2 enumerates all 5 possible states of rupture as well as the corresponding deformations of the concrete and of the GFRP bars:

Mode of failure	Deformation of the concrete	Deformation of the GFRP
1. Section entirely in tension	$\varepsilon_c < 0$	$\varepsilon_f = \varepsilon_{f,d}$
2. Section partially in tension with the GFRP pivot	$0 \leq \varepsilon_c < \varepsilon_{cu2}$	$\varepsilon_f = \varepsilon_{f,d}$
3. Section at the concrete and GFRP balanced pivot	$\varepsilon_c = \varepsilon_{cu2}$	$\varepsilon_f = \varepsilon_{f,d}$
4. Section partially in tension with the concrete pivot	$\varepsilon_c = \varepsilon_{cu2}$	$0 \leq \varepsilon_f < \varepsilon_{f,d}$
5. Section entirely in compression	$\varepsilon_c = \varepsilon_{cu2}$	$\varepsilon_f < 0$

Table 4.2: Models of rupture and the corresponding deformation of each material

Here are the expression of the resisting moment and the normal force [7]:

$$\begin{cases} N_{Rd} = F_c - F_f \\ M_{Rd} = M_c + M_f \end{cases} \tag{4.13}$$

$$\begin{cases} F_c = \begin{cases} f_{cd}\left[1 - \left(1 - \frac{\varepsilon_c}{\varepsilon_{c2}}\right)^2\right] b \cdot h_c & \text{if } 0 \leq \varepsilon_c < \varepsilon_{c2} \\ f_{cd} \cdot b \cdot h_c & \text{if } \varepsilon_{c2} \leq \varepsilon_c < \varepsilon_{cu2} \end{cases} \\ F_f = \sum_{i=1}^{n} E_f \cdot A_f \cdot \varepsilon_{f,i} \end{cases} \tag{4.14}$$

$$\begin{cases} M_c = F_c \cdot z_c \\ M_f = \sum_{i=1}^{n} F_f \cdot z_{f,i} \end{cases} \tag{4.15}$$

where

h_c: Depth of the concrete in compression $h_c = \lambda \cdot x$.

n: The number of rebar layers.

z_c: Distance between the center of gravity of the section and the application point of F_c [m].

$z_{f,i}$: Distance between the center of gravity of the section and the position of the rebar layer i [m].

4.2.2 Application to G10, G12, G15 and GNW

Following the method explained before, a diagram of interaction representing an envelope of the limit states of the walls can be created.

Interaction diagrams of Mohamed & al (2013): G10, G12, G15 [13] and Zhang et al (2019) [23]: GNW

Walls	G10	G12	G15	GNW
Axial loads [kN]	560	672	838	672
Axial load ratio ALR [%]		7%		25%

Table 4.3: Axial load applied on each wall. $N = ALR \cdot b_w \cdot l_w \cdot f_c$ [kN]

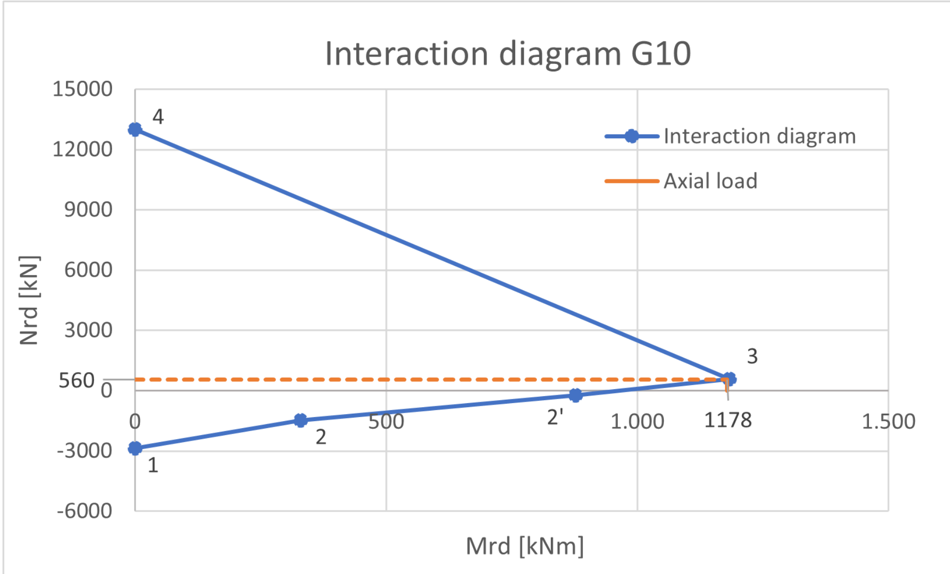

(a) Interaction diagram of G10. $M_{Rd} = 1178$ kNm for an axial force of 560 kN.

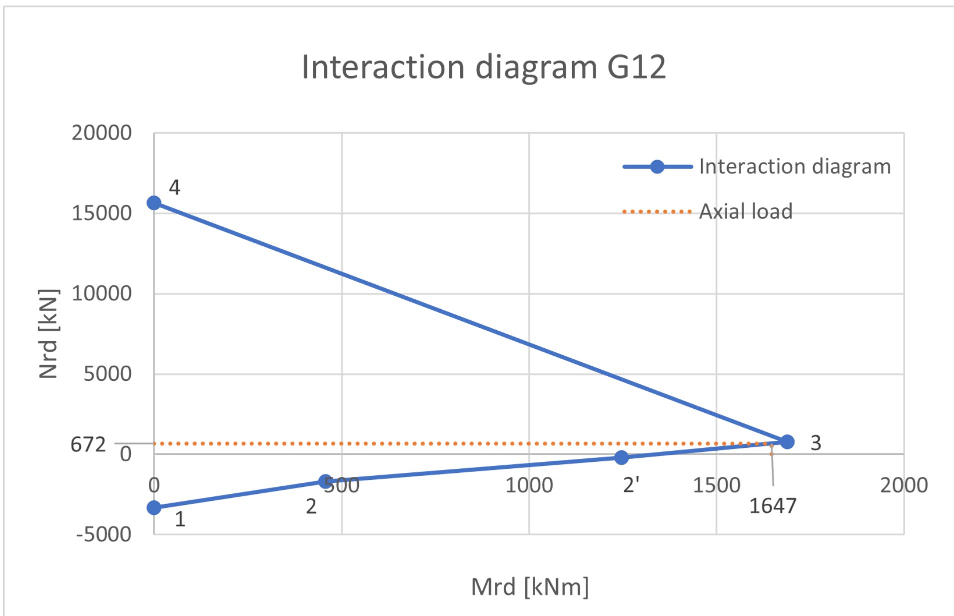

(b) Interaction diagram of G12. $M_{Rd} = 1647$ kNm for an axial force of 672 kN.

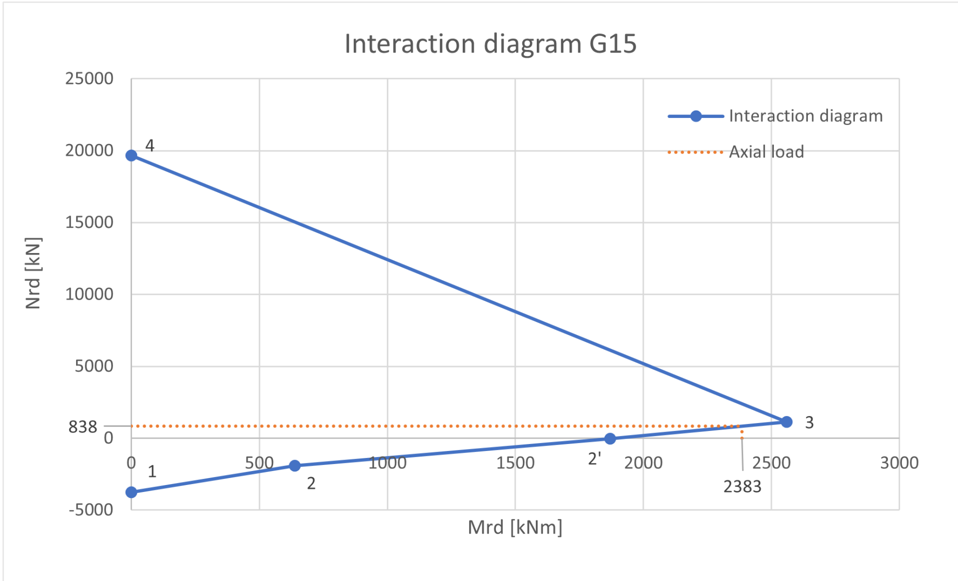

(c) Interaction diagram of G15. $M_{Rd} = 2383$ kNm for an axial force of 838 kN.

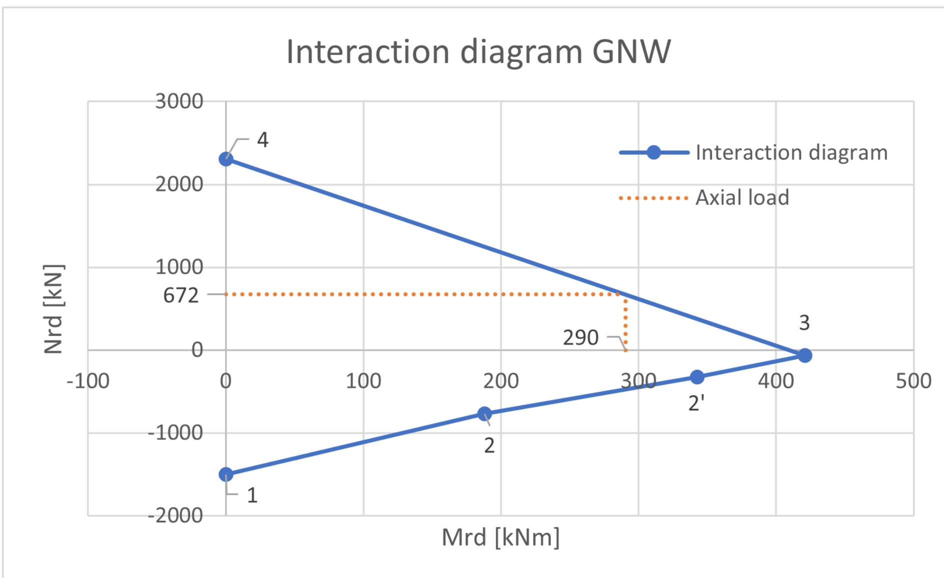

(d) Interaction diagram of GNW. $M_{Rd} = 290$ kNm for an axial force of 672 kN.

Figure 4.6: 1: section entirely in tension; 2: section partially in tension with GFRP pivot ($\varepsilon_c = 0$); 2': section partially in tension with GFRP pivot ($\varepsilon_c = \varepsilon_{c2}$); 3: section at balanced concrete and GFRP pivot; 4: section partially in tension with concrete pivot.

Comparison

		G15	G12	G10	GNW
Ultimate lateral load measured	V	586 kN	449 kN	289 kN	158 kN
Calculated base force at failure	V_b	681 kN	471 kN	337 kN	121 kN
Error		+16%	+5%	+17%	-23%

Table 4.4: Comparison between the measured ultimate lateral load and the predicted base force at failure derived from the calculated moment. $V_{rd} = \frac{M_{rd}}{L}$

It has to be noticed that the predicted base shear is now more accurate (the mean error is 15%) than in section 4.1.2 (the mean error was 36%). The value was overestimated, except for the wall GNW. The mode of failure predicted for GNW is concrete crushing, although for the other walls (G12 and G10) the failure can be in the rebars or the concrete since the section is at the balanced pivot (point 3 on the graphs 4.6b 4.6a) at failure. For G15, a failure is obtained in the rebars although experimentally it was concrete crushing. For the same reason as in section 3.5, the sectional analysis does not perform well in the prediction of the mode of failure.

4.3 Shear design

4.3.1 General method

This section will mainly follow the development of the Eurocode 2 [6] and the AFGC guide [7].

The objective is to obtain an expression for the resisting shear strength V_{Rd} to compare this value with the actual applied force V_{Ed}. To do so, the following expression has to be respected:

$$V_{Rd} > V_{Ed} \tag{4.16}$$

Shear strength without shear reinforcement First, it is useful to verify if shear reinforcement is needed. To consider the effect of the concrete and the longitudinal GFRP reinforcement, the codes rely on expressions applicable to steel-reinforced concrete. This is the expression of the shear strength from Eurocode 2 [6] for steel-reinforced concrete:

$$V_{Rd,c} = \frac{0,66}{\gamma_v} \sqrt[3]{100 \cdot \frac{d_{dg}}{d} \cdot f_{ck}} \cdot (b_w d) \tag{4.17}$$

However, this expression does not take into account the presence of GFRP reinforcement. The proposed solution is to add a reduction factor $\frac{E_f}{E_s}$ which corresponds to the ratio of rigidity of the both materials: GFRP and steel. [6]

$$V_{Rd,c} = \frac{0,66}{\gamma_v} \sqrt[3]{100 \cdot \rho_l \cdot \frac{E_f}{E_s} \cdot \frac{d_{dg}}{d} \cdot f_{ck}} \cdot (b_w d) \tag{4.18}$$

where

γ_v: the partial factor for shear resistance without shear reinforcement. $\gamma_v = 1,4$ at ULS.

ρ_l: $\frac{A_{sl}}{b_w d}$

A_{sl}: the area of FRP tensile reinforcement.

d_{dg}: is a size parameter referring to the aggregate size and depends on the concrete type

for a $f_{ck} < 60MPa$: $d_{dg} = 16mm + D_{lower}$

where D_{lower} is the minimum value of the largest sieve size D.

b_w: is the width of the cross-section.

d: the effective depth, the distance between the extreme compressed fiber and the center of gravity of the rebars in tension.

If the value of $V_{Rd,c}$ is smaller than V_{Ed}, then shear reinforcement is needed.

Shear strength with shear reinforcement In the case where shear reinforcement is required, the expression of the shear strength has to take into account the effect of the shear rebars. The new version of the Eurocode 2 [6] proposes for the shear resistance when yielding occurs in the shear reinforcement this expression:

$$V_{Rd,f} = V_{Rd,c} + \rho_w \cdot f_{fwRd} \cdot cot\theta \cdot b_w z \leq 0,17 f_{cd} \cdot b_w z \tag{4.19}$$

where

ρ_w: the shear reinforcement ratio $\frac{A_{sw}}{b_w s}$.

f_{fwRd}: the design value of the tensile strength $\frac{f_{fwk,100a}}{\gamma_{FRP}}$.

γ_{FRP}: the partial factor, $\gamma_{FRP} = 1,5$ at ULS.

θ: the angle between the compression field (struts) and the longitudinal reinforcement (see Figure 4.7). The next generation of EN2 recommends $cot\theta = 0,8$.

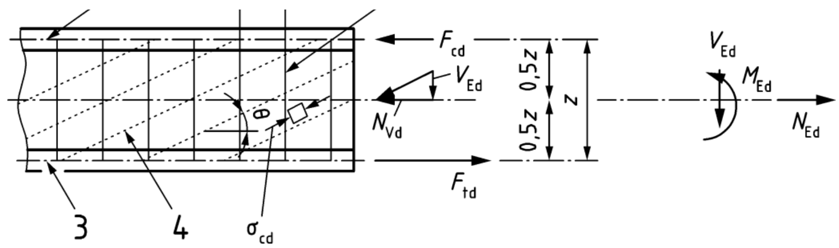

Key

1 axis of compression chord

2 shear reinforcement

3 axis of tension chord

4 struts (compression field)

Figure 4.7: Model for the design of shear reinforcement [6].

4.3.2 Application to G10, G12, G15 and GNW

The method was applied on each wall, but since the mode of failure was in flexion, there were no measurements of the shear capacity. It was not possible to verify our values for shear. Although it can be verified if the computed shear resistance is superior to the measured values at failure.

		G15	G12	G10	GNW
Ultimate lateral load measured	V	586 kN	449 kN	289 kN	158 kN
Predicted base force at shear failure	V_{Rd}	1116 kN	841 kN	721 kN	517 kN

Table 4.5: Comparison between the measured ultimate lateral load at concrete crushing and the predicted base force at shear failure.

These shear resistances computed with the method described above are highly superior to the ultimate load measured.

Chapter 5

I shaped wall design

The objective of this chapter is to present and justify the design of the wall, namely the cross-sectional shape and the reinforcement detailing. A first arbitrary design is proposed and its demand at failure is predicted by applying the analytical and numerical design procedures developed in chapters 3 and 4. Then, the values are compared with the practical limitations of the future experiment (i.e. the horizontal actuator can apply a maximum force of 1000kN on the top part of the wall) to show its feasibility.

5.1 General overview of the specimen

This wall was designed to be a scaled specimen of a possible realistic wall. For example, a wall in the central core of a building with lifts between the flanges on each side of the web.

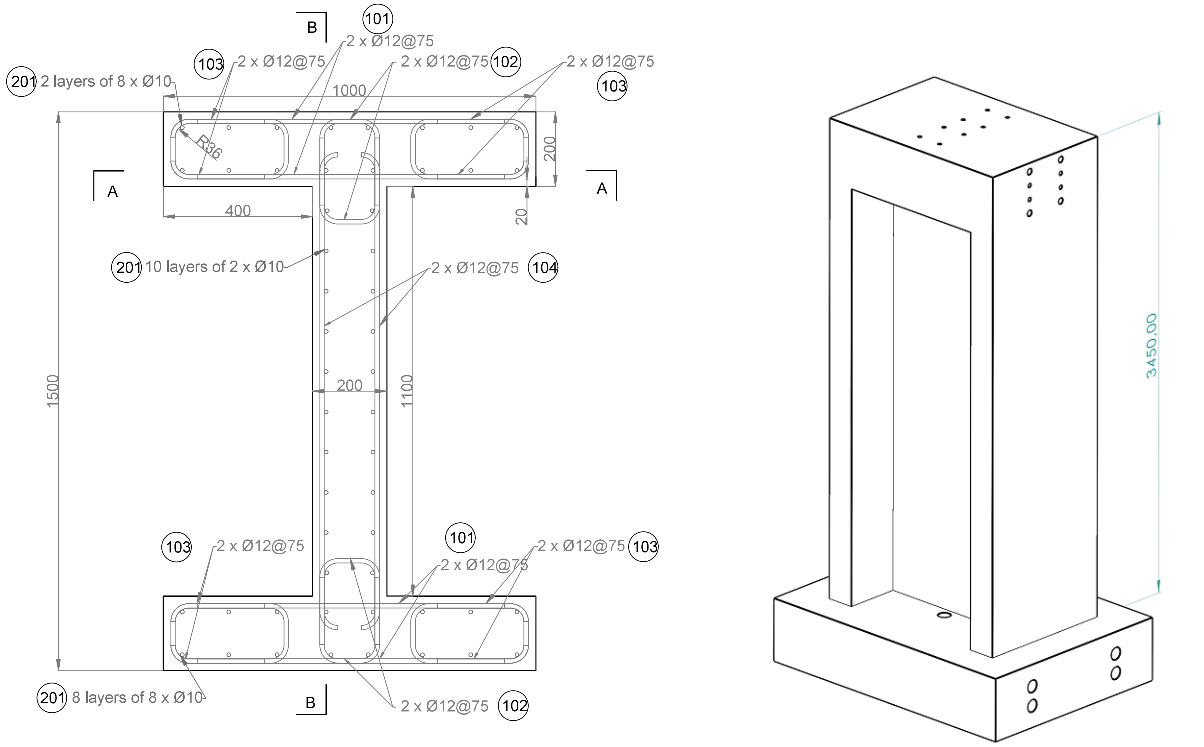

(a) Plan view of the GFRP reinforcement

(b) Elevation view of the I-shaped wall

Figure 5.1: Plan and elevation view of the I-shaped wall

This wall has an I-shape cross-section (see Figure 5.1a) of dimension 1000 mm x 1500mm (width B x length H). To the authors' knowledge, it is the first I-shaped RC wall test detailed with GFRP rebars. The flanges have a thickness and a height (b_f and h_f) of respectively 200 mm and 1000mm and the web has a thickness and a height (b_w and h_f) of 200mm and 1100mm. The aspect ratio of this wall is 2,3. The longitudinal reinforcement is GFRP rebars of diameters 10mm. The GFRP shear reinforcements have a diameter of 12mm. As seen on the elevation (Figure 5.1b), the total height (L) of the wall is 3450mm. The top part of the wall, the slab, has a height (L_c) of 450mm and the height of the specimen (L_s) is 3000mm (see Figures 5.2a and 5.2b). The actuators will be fixed in the slab at L_{eff} 3,25m height. The wall is fixed to a foundation base of dimensions 1500 x 2040 x 450mm (width b_b, length l_b, height h_b). Further discussion on foundation and slab design will take place in section 5.6.

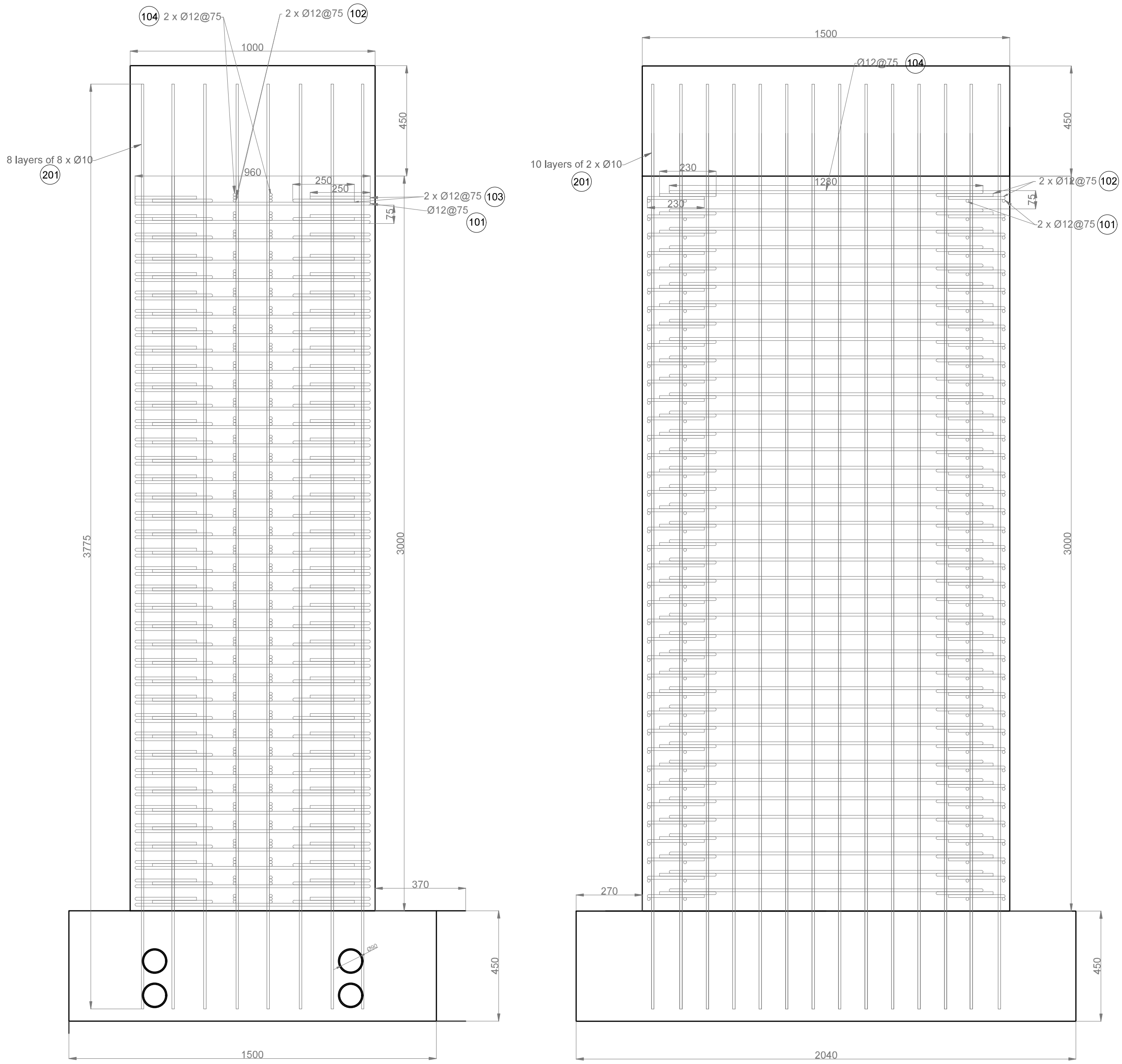

(a) Section AA of the GFRP reinforcement (b) Section BB of the GFRP reinforcement

Figure 5.2: Section AA and BB

5.2 Material properties

5.2.1 GFRP rebars properties

The GFRP rebars that will be used for the specimens are made by Sireg ®. These rebars are formed through a pultrusion process and are made with acrylic resin. Table 5.1 provides the mechanical properties of the GFRP rebars provided by Sireg [20]. It is worth noting that these values have been provided by the supplier and represent mean values and not characteristic design values.

Properties	ϕ	**10**	**12**	Units
Bending radius	r_b	>50	> 60	mm
Average tensile strength	$f_{f,t}$	1044	1033	MPa
Average tensile modulus of elasticity	E_f	53	53	GPa
Average ultimate strain	$\varepsilon_{f,t}$	0,0198	0,0196	mm/mm

Table 5.1: GFRP properties [20]

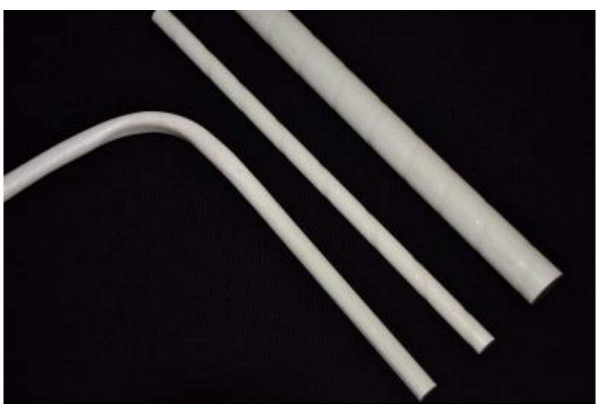

(a) Appearance of a GFRP rebar from Sireg

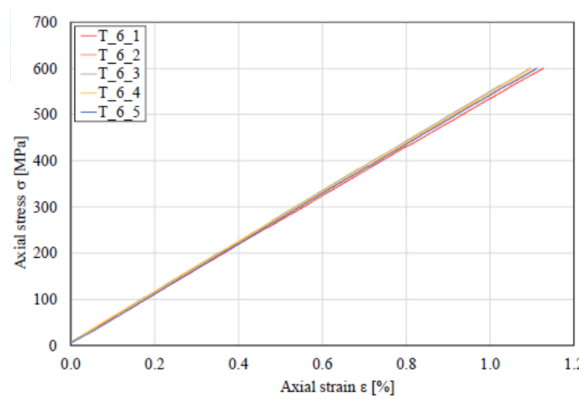

(b) Example of stress-strain curve for one batch from Sireg

Figure 5.3: Datas from Sireg [20]

5.2.2 Concrete properties

Since the concrete is not cast yet, a value of the concrete resistance can only be assumed. A C40/50 concrete is expected, which gives a compressive strength f_c = 40 MPa, see Table 5.2.

Properties	Symbols	Value	Units
Supposed compressive strength	f_c	40	MPa
Supposed modulus of elasticity	E_c	32	GPa
Supposed ultimate strain at peak stress	$\varepsilon_{c,2}$	0,02	mm/mm

Table 5.2: Concrete properties

5.3 Design verification

The values of material properties cited before will be used in the design and no safety factor will be applied to it. In this way, the resisting value of the tested wall will not be overestimated. An axial load of 900 kN is applied vertically at the top of the wall, and a lateral force of up to 1000 kN is applied at the center of the slab at 3,25m height.

5.3.1 Pure bending design

In this wall, the concrete is confined thanks to the boundary ties situated in the intersection between the flange and the web. To consider this confinement, as in section 4.1.2, the Mander stress-strain curve will be computed (see Figure 5.4)[12]. Therefore, the confined compressive strength of the concrete f_{cc} is 46 MPa.

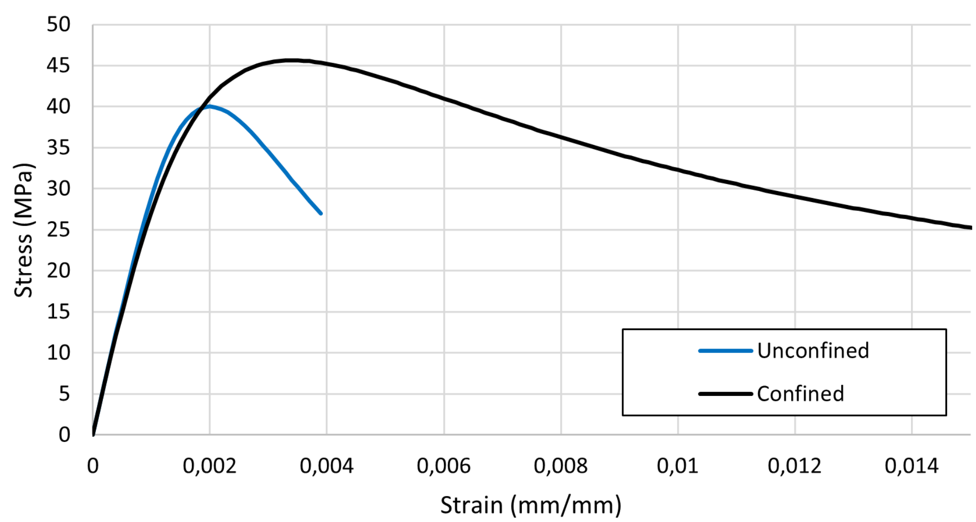

Figure 5.4: Mander stress-strain model for confined concrete I-shaped wall

To obtain the moment of resistance analytically, the method exposed in section 4.1 is applied.

The ratio of reinforcement:

$$\rho_f = \frac{A_f}{A_{c,red}} = \frac{2827}{620 \cdot 10^3} = 0,46\%$$

The balanced reinforcement ratio:

$$\rho_{f,b} = \frac{\eta f_{cc} \lambda}{f_{f,u}} \frac{\varepsilon_{cu2}}{\varepsilon_{cu2} + \varepsilon_{f,u,d}} = \frac{1 \cdot 46 \cdot 0,8}{1044} \frac{0,35}{0,35 + 2,1} = 0,53\%$$

Since $\rho_f < \rho_{f,b}$, the failure will be dominated by the rupture of the GFRP rebars. The strain at failure in the concrete is:

$$\varepsilon_c = \left(\frac{\varepsilon_{f,t}}{\lambda \frac{\eta f_{cc}}{f_{f,t} \rho_f} - 1} \right) = \left(\frac{1,98}{0,8 \frac{1 \cdot 46}{1044 \cdot 0,0046} - 1} \right) = 0,29\%$$

$$\varepsilon_{cu2} \geq \varepsilon_c \geq \varepsilon_{c2}$$

$$0,35\% \geq 0,29\% \geq 0,20\%$$

The position of the neutral axis is:

$$x = \frac{\varepsilon_c}{\varepsilon_c + \varepsilon_{f,t}} d = \frac{0,29}{0,29 + 1,98} 1,04 = 0,134m \tag{5.1}$$

The resisting moment will be:

$$M_{Rd} = A_f \cdot f_{f,t} \left(d - \frac{\lambda}{2} x \right) = 2827 \cdot 1044 \left(1,04 - \frac{0,8}{2} 0,134 \right) = 2908kNm$$

The force at the base of the wall will be at the rebars failure:

$$V_b = \frac{M_{Rd}}{L_{eff}} = \frac{2908}{3,25} = 894kN$$

Due to its I-shape the wall has a different mode of failure compared to the other wall studied before (see chapter 4). Indeed, the failure occurs first in the GFRP rebar. This is probably explained by the large area of concrete present in the flange. The area of concrete is directly linked with the resistance of the concrete. Therefore, even if it is preferable to have a concrete crushing failure to observe more elasticity, it has been decided to keep this mode of failure (rebars failure) to conserve a realistic I-shape.

Then the amount and the diameter of longitudinal armatures have been chosen to obtain a base force at failure smaller than the possible applicable force from the actuators which is 1000kN. Indeed, the purpose of the test is to observe the behavior of the wall at failure, thus it has to reach failure.

5.3.2 Bending with axial load design

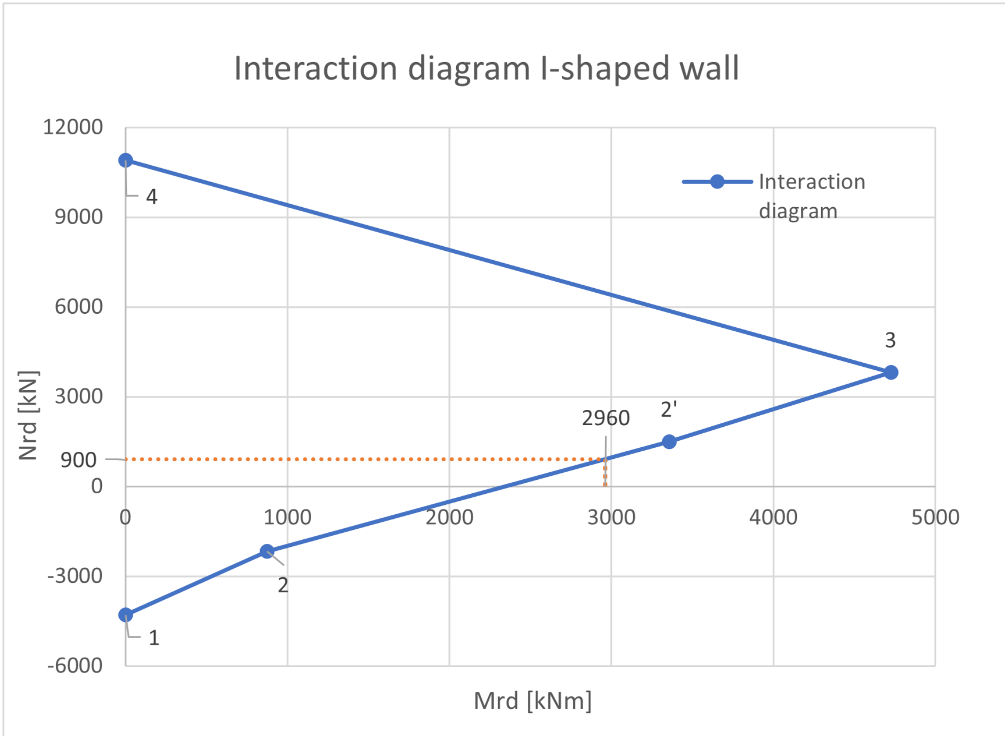

Figure 5.5: Interaction diagram of I-shaped wall. $M_{Rd} = 2960$ kNm for an axial force of 900 kN. 1: section entirely in tension; 2: section partially in tension with GFRP pivot ($\varepsilon_c = 0$); 2': section partially in tension with GFRP pivot ($\varepsilon_c = \varepsilon_{c2}$); 3: section at balanced concrete and GFRP pivot; 4: section partially in tension with concrete pivot.

The interaction diagram shows the same mode of failure as the method without axial load: governed by the failure in the rebars. This strongly supports the previous prediction of rupture mode.

By considering the axial load, a larger resisting moment ($M_{Rd} = 2960$ kNm) is obtained compared to 2908kNm obtained in section 5.3.1 , which gives a larger base force at failure: $V_b = \frac{2960}{3,25} = 911$ kN. This difference was expected. Indeed, the axial load put the section in compression, delaying the failure in tension. Still, the values are quite close to each other.

5.3.3 Shear design

The shear resistance has to be verified because it has to be certain that the rupture will be due to bending. Indeed, a shear rupture is fragile and sudden. It is preferable to have the most plastic rupture possible to observe the evolution of the failure.

To obtain the shear resistance, the design procedure explained in chapter 4 is applied.

Shear strength without shear reinforcement

$$
\begin{aligned}
V_{Rd,c} &= \frac{0,66}{\gamma_v}\sqrt[3]{100\cdot\rho_l\cdot\frac{E_f}{E_s}\cdot\frac{d_{dg}}{d}\cdot f_{ck}}\cdot(b_w d)\\
&= \frac{0,66}{1,4}\sqrt[3]{100\cdot\frac{2827\cdot10^{-6}}{0,2\cdot1,04}\cdot\frac{53}{200}\cdot\frac{0,02}{1,04}\cdot46}\cdot(0,2\cdot0,935)\cdot10^3\\
&= 60kN
\end{aligned}
$$

Shear reinforcement is needed here. Indeed 60 kN is much smaller than the bending resistance of the wall which is around 900 kN.

Shear strength with shear reinforcement The shear reinforcements ($\phi12$) are spaced by 75mm (see on Figures 5.2a, 5.2b and 5.1a).

$$
\begin{aligned}
V_{Rd,f} &= V_{Rd,c}+\rho_w\cdot f_{fwRd}\cdot cot\theta\cdot b_w z\\
&= 60+\frac{0,007}{0,2}\cdot cot(51)\cdot169\cdot0,2\cdot0,935\cdot10^3\\
&= 940kN
\end{aligned}
$$

The wall has a predicted flexion resistance of 911 kN and since this shear resistance is higher. It should be sufficient to avoid shear failure.

5.4 Numerical prediction of force-displacement response

5.4.1 Response 2000

Figure 5.6c shows that the GFRP reaches its maximum stress at failure whereas concrete (see Figure 5.6d) does not. In Figure 5.6b, when the curve reaches the resisting moment, it collapses quickly, corresponding to a fragile rupture. It can be deduced that the rupture occurs in traction in the reinforcement. The resisting moment $M_{Rd} = 3226$ kNm, which gives a base shear at failure $V_b = 993$ kN.

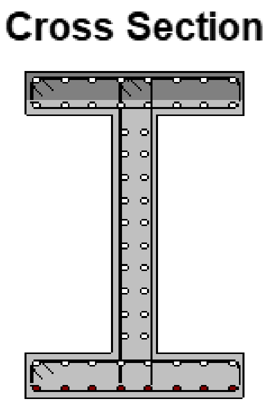

(a) I-shaped wall (thickness 200mm, width 1000mm)

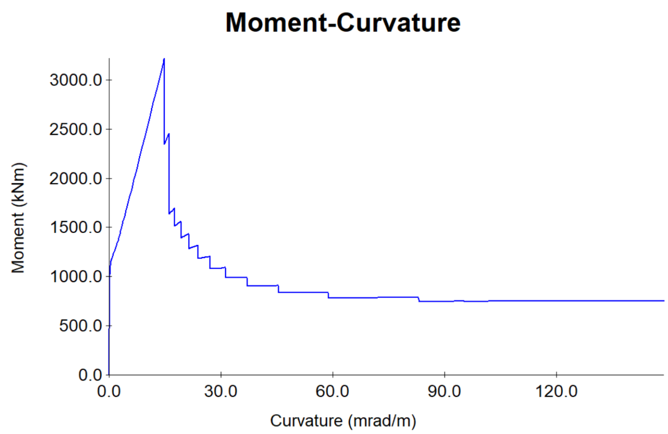

(b) Moment curvature curve. The rebars failure at 3226,5 kNm

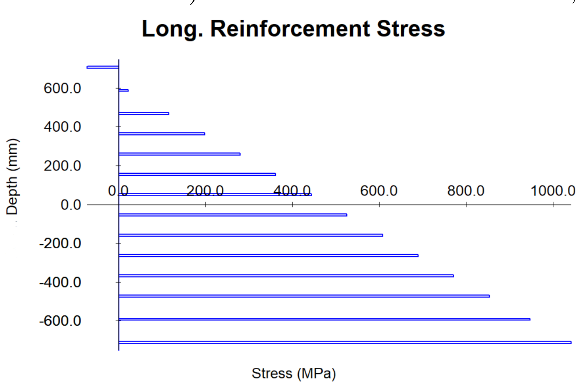

(c) Longitudinal reinforcement stress at failure. In the most solicited part, $f_{gfrp} = 1040MPa$. Recall: the tensile strength is $f_{f,u} = 1044MPa$

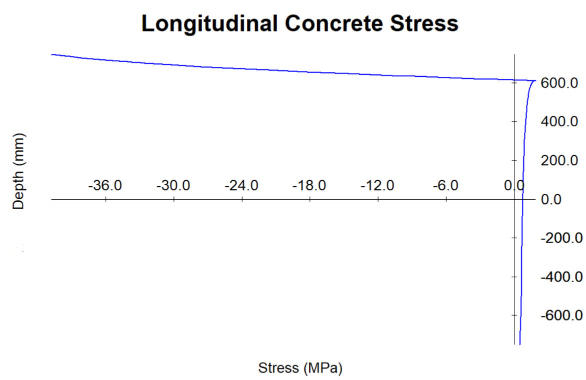

(d) Concrete stress at failure. In the most solicited part, $f_c = 40,8MPa$. Recall: the confined compressive strength is $f_{cc} = 46MPa$

Figure 5.6: Response 2000 results of the final design of the I-shape wall

5.4.2 Seismostruct

In this section, a numerical analysis of the I-shaped wall will be carried out to determine its base shear capacity using Seismostruct software. This analysis will help complete and confirm the results obtained in the previous section using Response 2000. The same method discussed in Chapter 3 will also be used here. Therefore, a beam-truss model will be employed with an elastic model for the materials.

The geometry of this wall is described earlier in section 5.1. Figure 5.7a shows the plan view of the beam-truss model. The wall section is divided into 7 parts where the ones on the extremities are the same and have the following dimensions: 1000 mm x 200 mm. The other parts of the section have dimensions of 220 mm x 200 mm.

Figure 5.7b shows the elevation view of the beam-truss model. It is divided into 15 pieces along its height. The wall itself is divided into 10 pieces, each 300mm high. The slab, on the other hand, is divided into 5 pieces, of 100mm height. The vertical and horizontal elements are inelastic displacement-based frame elements, while the diagonals are inelastic truss elements.

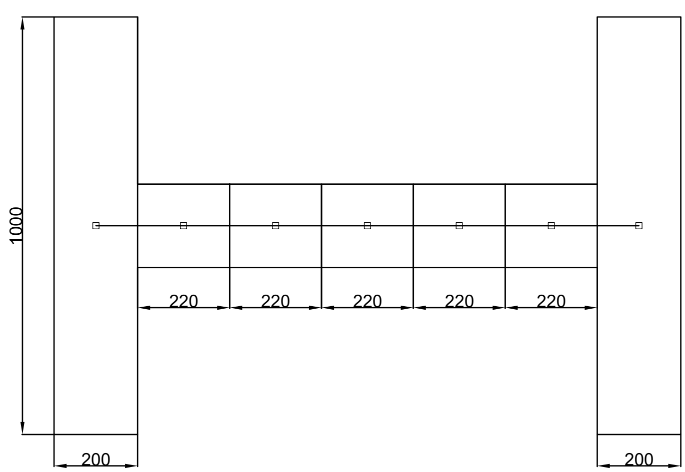

(a) Beam-truss model: plan view of I-shaped wall

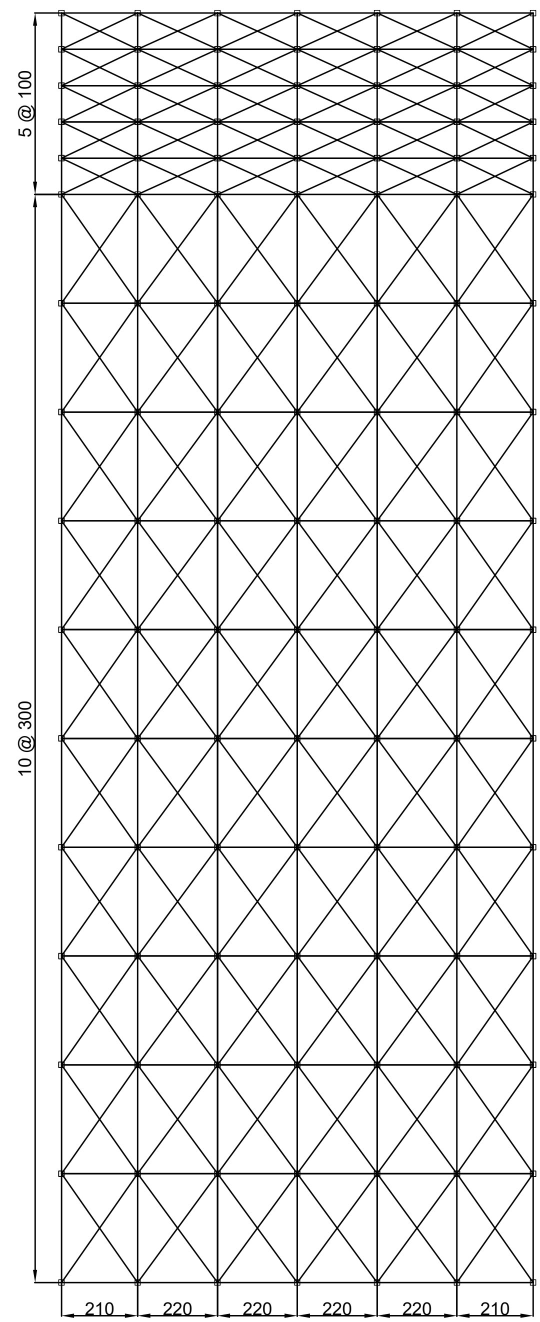

(b) Beam-truss model: elevation view of I-shaped wall

Figure 5.7: Elevation and plan views of the beam-truss model

An axial load is applied to the wall and distributed over the top nodes of the model.

Wall	I-shaped
Axial load [kN]	900

Table 5.3: Axial load (3,6% of the axial capacity) applied on the wall. $N = 0,036 \cdot A \cdot f_c$ [kN] (see section 6.1).

A static pushover analysis was performed on the beam-truss model of the I-shaped wall. The force-displacement curve was obtained where the displacements correspond to those of the top of the wall.

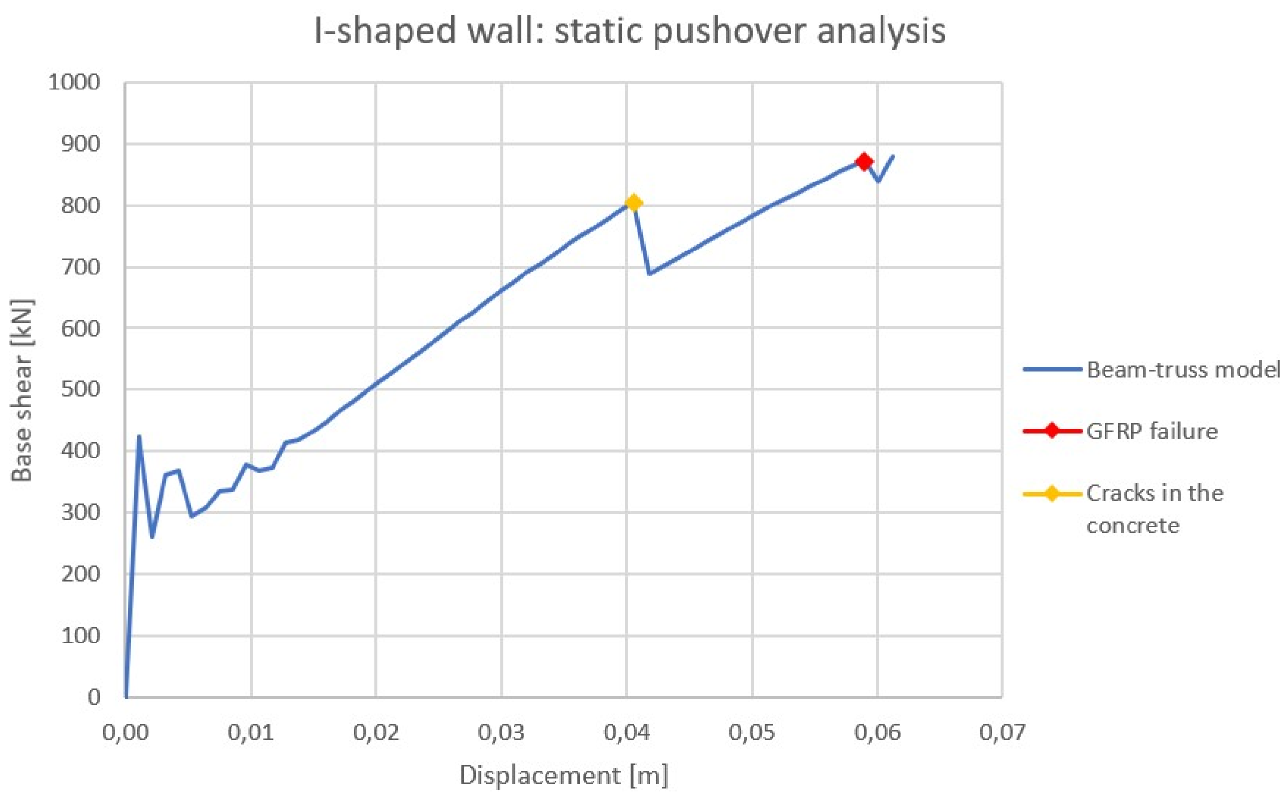

Figure 5.8: I-shaped wall: Force-displacement curve

There are 2 key elements in the force-displacement curve (Figure 5.8). Firstly, there is an initial drop in the curve, more or less towards a displacement of 4 cm. At this point, the base shear drops by around 120 kN which corresponds to about 13% of the maximum strength. Typically, a drop of 20% of the maximum strength is required for it to be regarded as a global failure. As this initial drop does not constitute a global failure, the loading of the wall continues until the second drop occurs, close to the wall's maximum strength.

To analyze the behavior of the wall in greater depth, it is valuable to focus on the deformations of both the concrete and FRP reinforcements.

Concrete strain

Figure 5.9 illustrates the strains of the confined concrete as a function of the load factor. These strains belong to an element located at the base of the flange which is directly connected to the actuator. The load factor is a coefficient utilized to gradually apply increasing lateral loads to the structure.

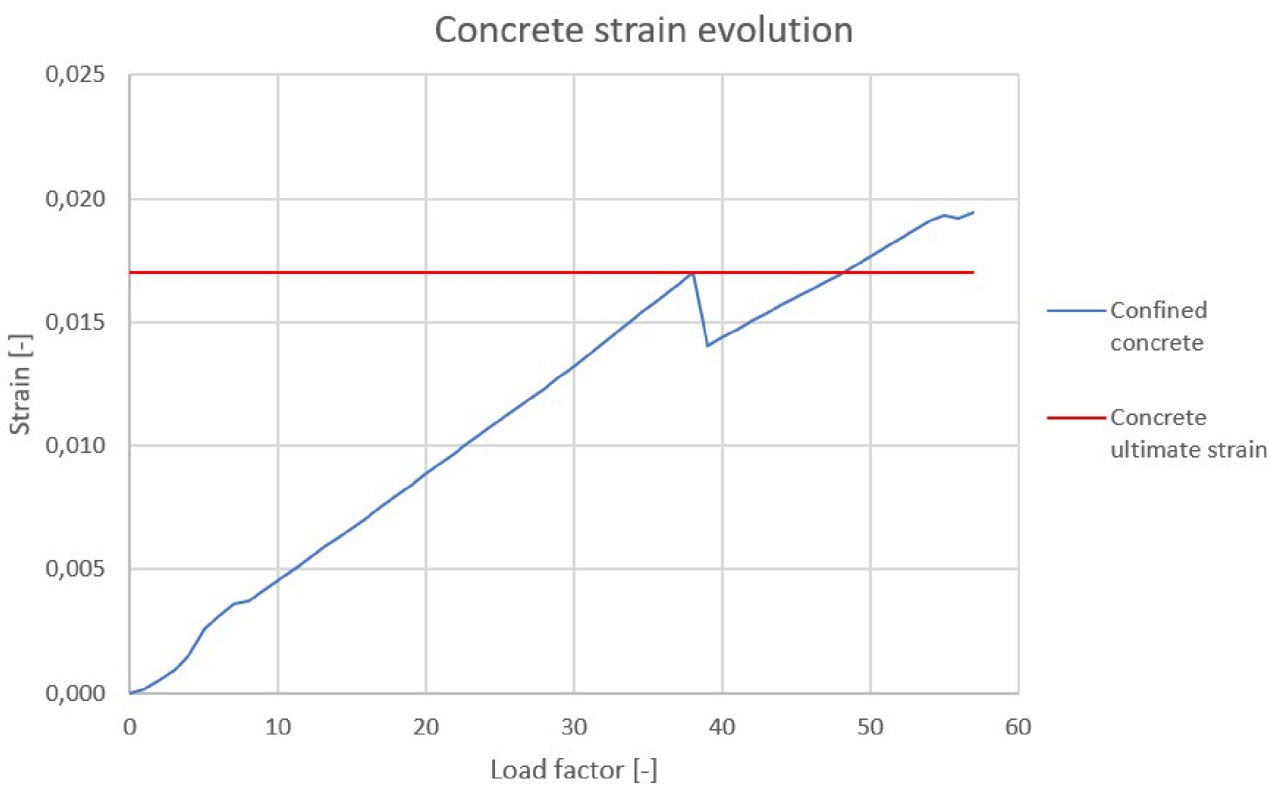

Figure 5.9: I-shaped wall: concrete strain versus load factor

To determine the failure, strain limits have to be implemented into Seismostruct to highlight some failure criteria such as concrete crushing. The applied limit strains are derived from comparable values found in the existing literature. For concrete, an initial value of $\varepsilon = 0,015$ is proposed. Once this value is reached, the software signals to the user that the limits have been attained. However, it does not stop loading beyond these thresholds [8].

Once the static pushover analysis has been carried out, we see that the first drop appeared when the strain is 0,017. This value is very close to the one proposed in the literature ($\varepsilon = 0,015$). Furthermore, it is known that the value of the ultimate strain is influenced by factors such as confinement and is challenging to predict. It, therefore, seems realistic to consider that the value of $\varepsilon = 0,017$ is the actual ultimate strain for our wall. This would imply that the first drop corresponds to the initial concrete failure. Cracks can thus be expected to appear in this area.

Also, as the loss of strength due to this drop is only 13% of the maximum strength, the appearance of cracks in the concrete does not signify a complete wall failure. Consequently, the loading of the wall continues, and it's now the reinforcements that are taking over the stresses at this point.

GFRP strain

Figure 5.10 illustrates the strains of one GFRP rebar as a function of the load factor. These strains belong to a longitudinal rebar located in the corner of the flange which is directly connected to the actuator (Rebar 1 see Figure 5.11).

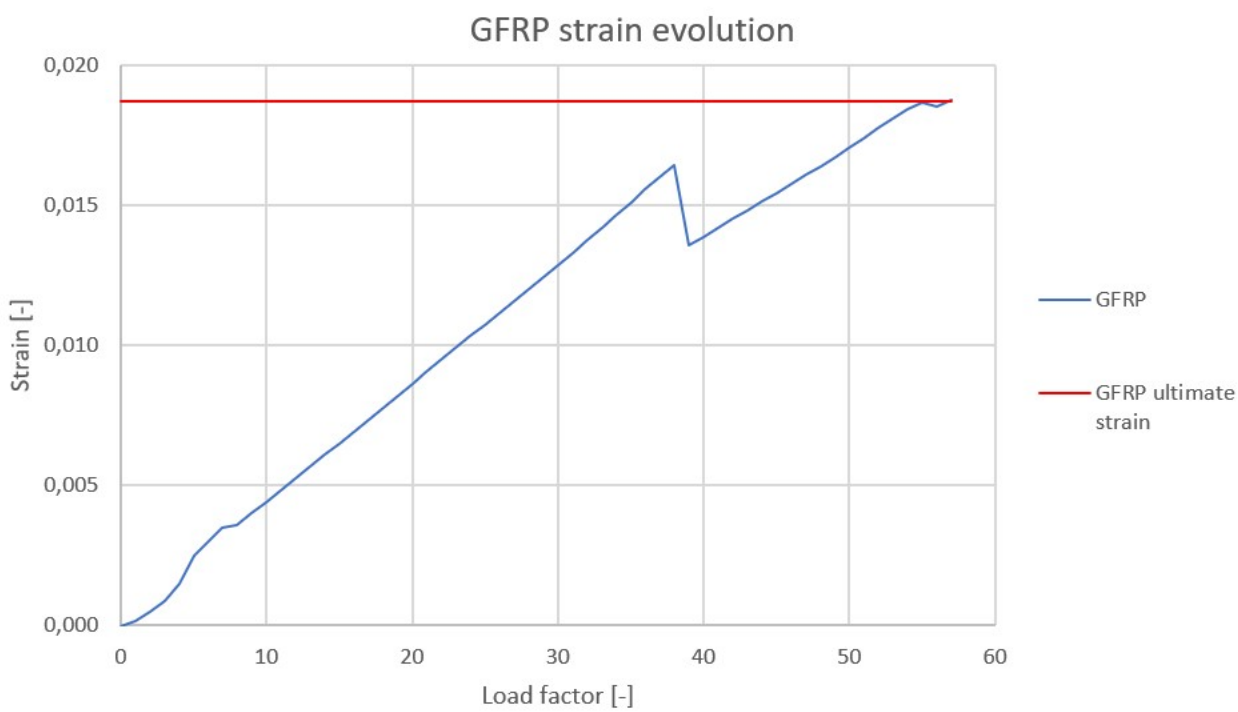

Figure 5.10: I-shaped wall: GFRP strain versus load factor

To determine the failure, strain limits have to be implemented into Seismostruct to highlight some failure criteria such as GFRP failure. The ultimate strains chosen for the longitudinal and transverse reinforcements correspond to those provided by the manufacturer of these bars, Sireg (see Table 5.4).

Sireg	ϕ 10 (longitudinal reinforcement)	ϕ 12 (transverse reinforcement)
Ultimate strain	0,0187	0,0185

Table 5.4: GFRP ultimate strains from Sireg [20]

Once the static pushover analysis has been carried out, it can be observed that the second drop occurs when the strains in the bar reach the ultimate limit ($\varepsilon = 0,0187$). This results in the failure of this longitudinal reinforcement (Rebar 1, Figure 5.11). As this strength drop still does not lead to the complete failure of the wall, the loading continues until a second bar (Rebar 2, Figure 5.11), in the web this time, once again reaches the ultimate limit. The failure of the first bar, closely followed by the second one, then leads to the global failure of the wall.

Based on these results, it can be concluded that the failure of the wall is due to the failure of the GFRP bars. This confirms the results obtained with Response 2000 and the analytical methods. The rebars affected are longitudinal rebars located in the flange and in the web near the side where the displacement was applied, as can be seen in Figure 5.11.

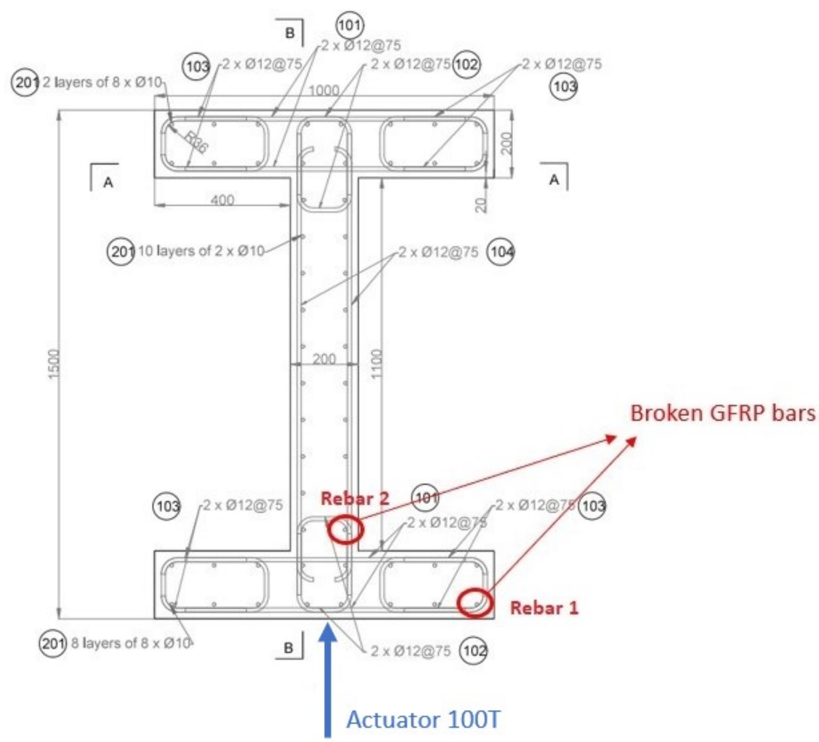

Figure 5.11: I-shaped wall: broken GFRP rebars

At failure, the numerical model predicts a base shear value of 878 kN (see Table 5.5). This value is of the same order of magnitude as the results obtained analytically.

Beam-truss model results	I-shaped wall
Predicted base shear	878 kN
Displacement capacity	61 mm

Table 5.5: Summary of the results for the I-shaped wall from Seismostruct

5.4.3 Sensitivity analysis

To gain a deeper understanding of the wall behavior, a sensitivity analysis is conducted using the Response 2000 model. The influence of three parameters is investigated: the dimension of the wall, the characteristics of the GFRP rebars, and the concrete properties. To do so, a comparison is made between 4 configurations of the I-shaped wall, which are described in Table 5.6

Wall	Parameter	Thickness [mm]	Width [mm]	ϕ [mm]	f_c [MPa]	ε_{cu2} [mm/m]
A	Baseline	200	1000	10	46	3,7
B	Wall dimensions	**150**	**700**	10	46	3,7
C	Rebars diameter	200	1000	**12**	46	3,7
D	Concrete resistance	200	1000	10	**40**	**2,1**

Table 5.6: Walls configurations for the sensitivity analysis. ϕ corresponds to the diameter of the rebars. f_c corresponds to the concrete resistance. ε_{cu2} corresponds to the theoretical ultimate strain of the concrete given by Response 2000.

The sensitivity analysis focuses on the dependence between the parameter values and two important features: the resisting moment and the concrete strain at failure.

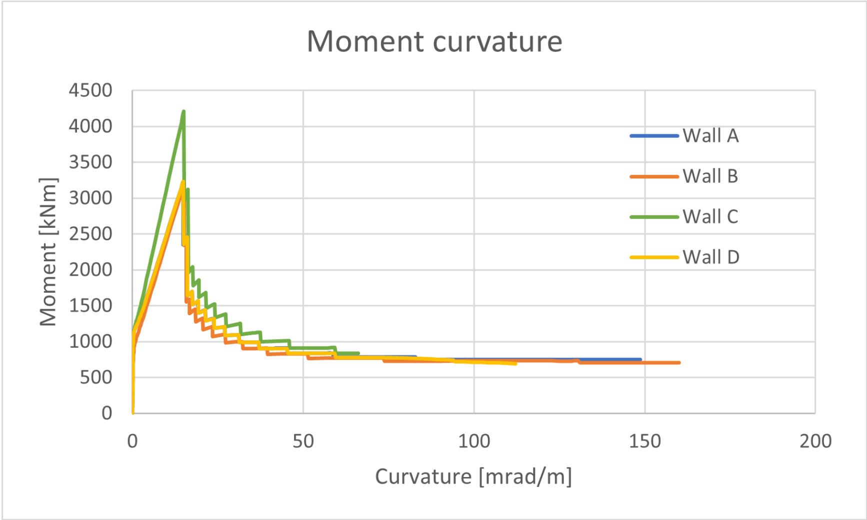

Figure 5.12: Moment curvature resulting from the sensitive analysis. Wall A corresponds to the Baseline. Wall B corresponds to wall dimensions variation. Wall C corresponds to rebars characteristics variation. Wall D corresponds to the concrete resistance variation.

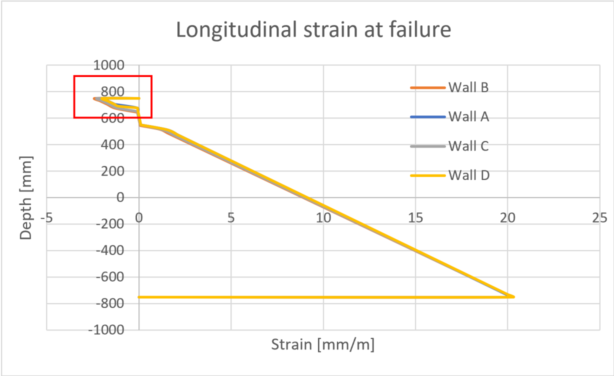

(a) Longitudinal strain at failure

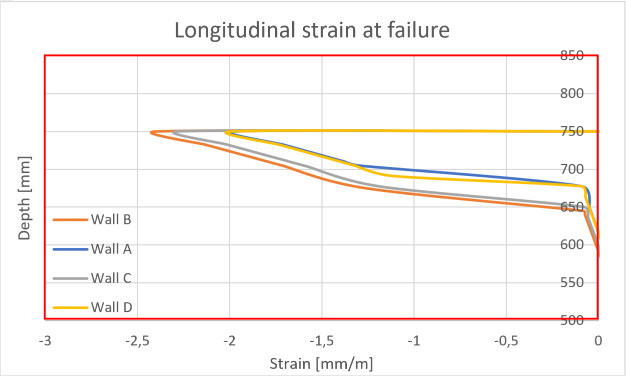

(b) Zoom on the concrete zone

Figure 5.13: Longitudinal strain at failure resulting from the sensitive analysis. Wall A corresponds to the Baseline. Wall B corresponds to wall dimensions variation. Wall C corresponds to rebars characteristics variation. Wall D corresponds to the concrete resistance variation.

Wall	Parameter	Moment at failure	Strain at failure	Concrete strain ratio
A	Baseline	3226 kNm	1,97 mm/m	53,2%
B	Wall dimensions	3200 kNm	2,4 mm/m	**64,9** %
C	Rebars characteristics	**4200** kNm	2,3 mm/m	62%
D	Concrete Resistance	3350 kNm	2 mm/m	**95,2** %

Table 5.7: Results of the sensitivity analysis. The concrete strain ratio is the ratio between the concrete strain at failure and the theoretical ultimate strain of the concrete. This ratio represents how close the concrete is to its ultimate value (possible failure of the concrete).

It can be observed that a reasonable change in dimensions only minimally affects the moment resistance (see Table 5.7 or Figure 5.12). This is not surprising, as the rupture mode (within the GFRP bars) remains the same. However, as expected, the concrete strain ratio has slightly increased to 64,9 % (see Table 5.7 or Figure 5.13). This is due to a reduced concrete area having to bear the same load, resulting in an increase in the concrete strain. In supplementary analyses, the width of the flanges was drastically reduced to approach a rectangular wall shape [1]. Here, a high concrete strain ratio is observed, which might indicate a rupture of the wall due to concrete crushing, as reported in the existing literature.

By increasing the diameter of the bars, a notable rise in the resisting moment is observed. This increased demand was also noticed in supplementary analyses when the tensile strength of the reinforcements was increased. Given that the predicted rupture mode is located within the reinforcements, it becomes quite evident that amplifying the strength or diameter of the rebars leads to an augmentation in wall resistance. However, this increase in strength needs to be considered carefully, as practical challenges may arise. In particular, the rupture of the wall could be impossible to reach due to the technical limitations of the experimental setup. The failure of the wall could require a demand exceeding the capacity of the actuators (100T).

Another practical consideration is the potential decrease in concrete compressive strength. As shown in Table 5.7, it can be observed that in this scenario, the concrete strain ratio increases significantly and closely approaches the point of rupture. This could lead to the occurrence of a concrete crushing failure of the wall.

[1]These results are not presented as they violate the I-shaped wall geometry.

5.5 Summary of the predictions

The previous sections analyzed the I-shaped wall in different ways. The aim of these analyses was to cross-check the results in order to be confident about them. Table 5.8 shows the base shear values obtained using the 3 approaches: bending with axial load design, Seismostruct, and Response 2000. In chapter 3 and 4, these approaches were applied on the tested wall. It's noteworthy from this analysis that all these models tended to overestimate the demand compared to reality.

	Analytical design	Seismostruct	Response 2000
Base shear	911 kN	878 kN	993 kN

Table 5.8: Summarize of the predictions

The values obtained are relatively similar. The mean base shear value is 929 kN with a standard deviation of 28 kN. These results allow us to be quite confident about our predictions. Finally, it is essential to note that the mode of failure is the same for the 3 approaches. In each case, it is the GFRP bars that fail in tension.

5.6 Foundation and wall slab design

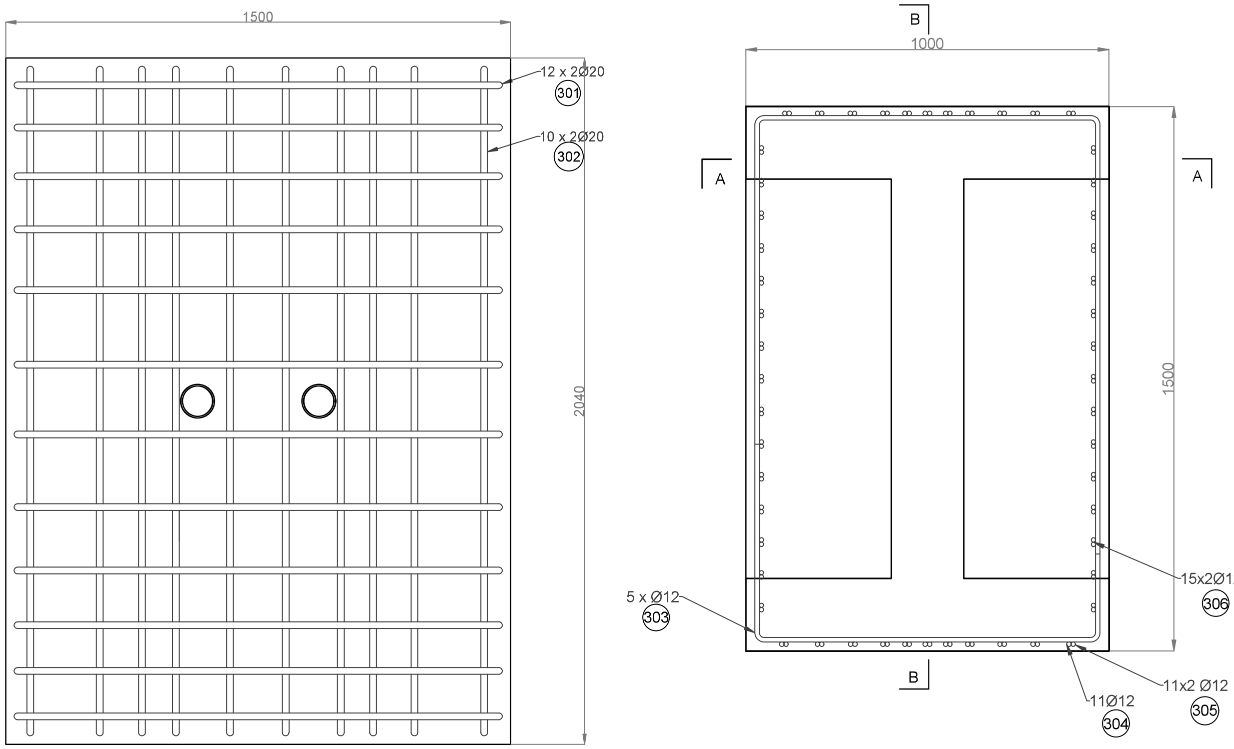

Figure 5.14: Plan view of the steel reinforcement respectively in the foundation and in the slab

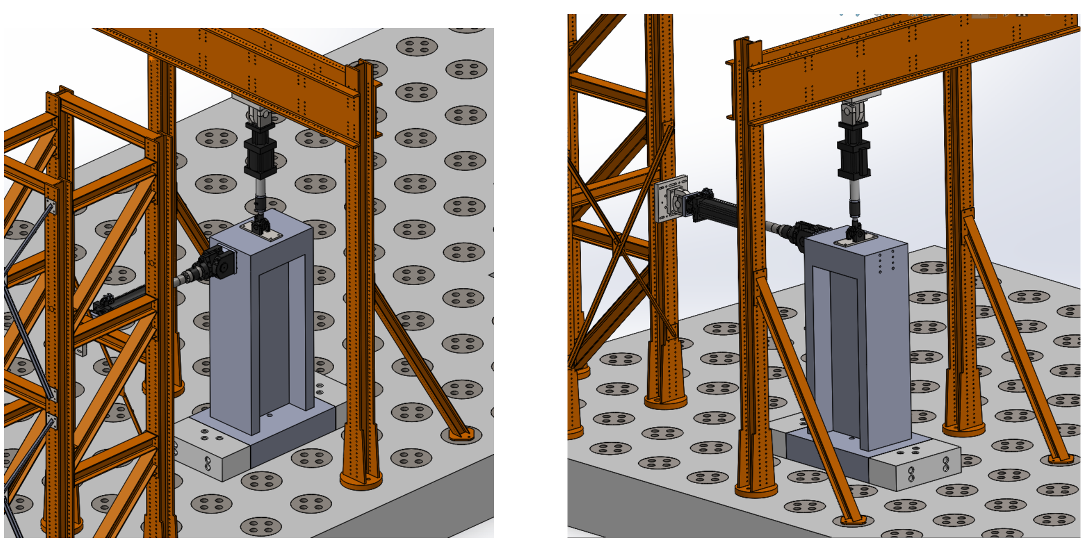

Figure 5.15: 3D view of the specimen in the lab

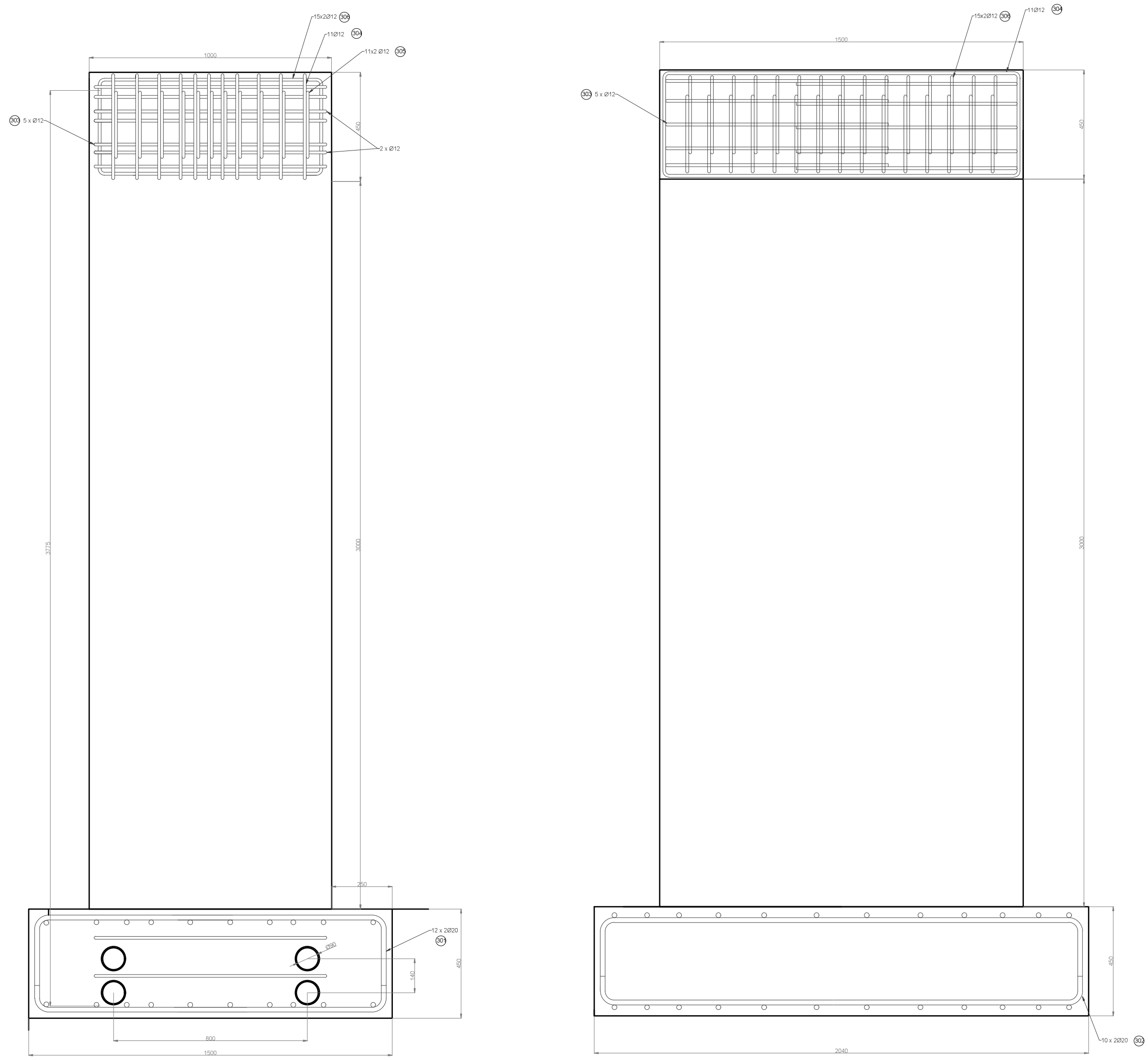

(a) Section AA of the steel reinforcement (b) Section BB of the steel reinforcement

Figure 5.16: Section AA and BB of steel reinforcements in slab and foundation

The purpose of the experiment is to test the GFRP reinforcement reaction in a wall. Thus, the rupture is required to occur in the wall and not in the foundation or in the slab. Therefore, the use of steel as reinforcement was decided as it is well-known and it assures a well-reinforcement of the slab and the foundation. The height of the foundation and the collar is 450mm to assure a sufficient anchorage length of minimum 351 mm[2].

The foundation itself is anchored (with Dywidag rebars ϕ 40) to the floor of the lab.

[2]This has been determined following the guidelines of the next generation of the Eurocode 2 [6], see Excel file

There are two Dywidag rebars in the center of the foundation (see Figure 5.14) and 6 others in the isometric blocks (3 in each see Figure 5.15). Each rebar can retain 250kN. To verify stability against overturning, an equilibrium of moments is established around point O (see Figure 5.17).

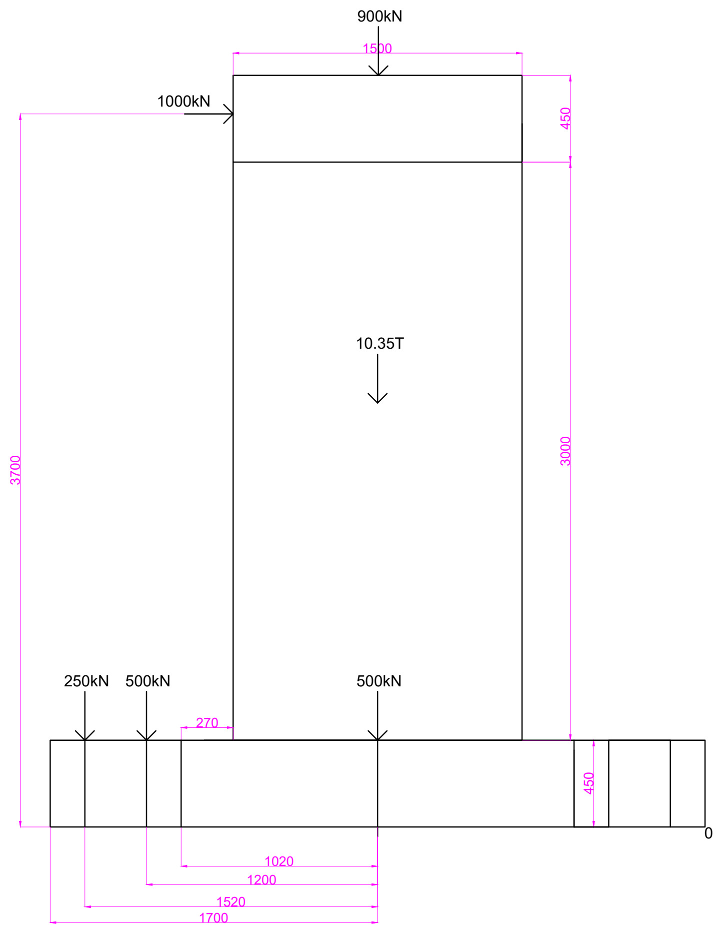

Figure 5.17: Summary of the forces acting on the wall

$$\begin{aligned}\sum M_0 : 1000 \cdot 3,7 < 1,7m \cdot 10,35T \cdot 9,81m/s^2 + 500kN \cdot 2,9m + 250kN \cdot 3,22m \\ + 500kN \cdot 1,7m + 900kN \cdot 1,7m \\ 3700kNm < 4808kNm \\ \text{Respected}\end{aligned}$$

The anchorages are sufficient to withstand the maximal applied bending moment of 3700kNm.

Chapter 6

Experimental Programme at LEMSC, UCLouvain

The goal of this work is to design a wall in preparation for a future experimental test. This chapter will browse the proposed solution to complete this future test. One of the main challenges is the position and the configuration of the wall in the lab (LEMSC). A Solidworks file was made to fit precisely the wall in the experimental setup. As mentioned previously, two actuators of 100T will apply forces on the wall. A proposed loading protocol has been made for one of the actuators. Finally, a proposition of instrumentation is given to measure and collect all the data needed in order to analyze the results later.

6.1 Test setup

There are 2 actuators of 100T that apply forces on the wall (see Figures 6.1). The horizontal actuators are connected to the wall at a height of 3,7m in the slab. It can induce a moment of 3700 kNm (maximal capacity of the actuator: 100T at 3,7m height) at maximum. The wall was designed to break for a moment of around 3000 kNm. The vertical actuator will apply an axial load of 900 kN which corresponds to an axial load ratio (ALR) of 3,6%:

$$ALR = \frac{N}{f_c A} \tag{6.1}$$

with A the area of the cross-section (0,62m^2) and f_c the compression strength of the concrete (40MPa).

The foundation is composed of two isometric blocks and a central foundation beneath the wall (see Figure 6.1). The isometric blocks are maintained to the wall thanks to four post-tensioned threaded rods. Each block is maintained to the strong floor with 3 post-tensioned threaded robs. The wall itself is also connected to the wall with two Dywidag rebars in the central foundation.

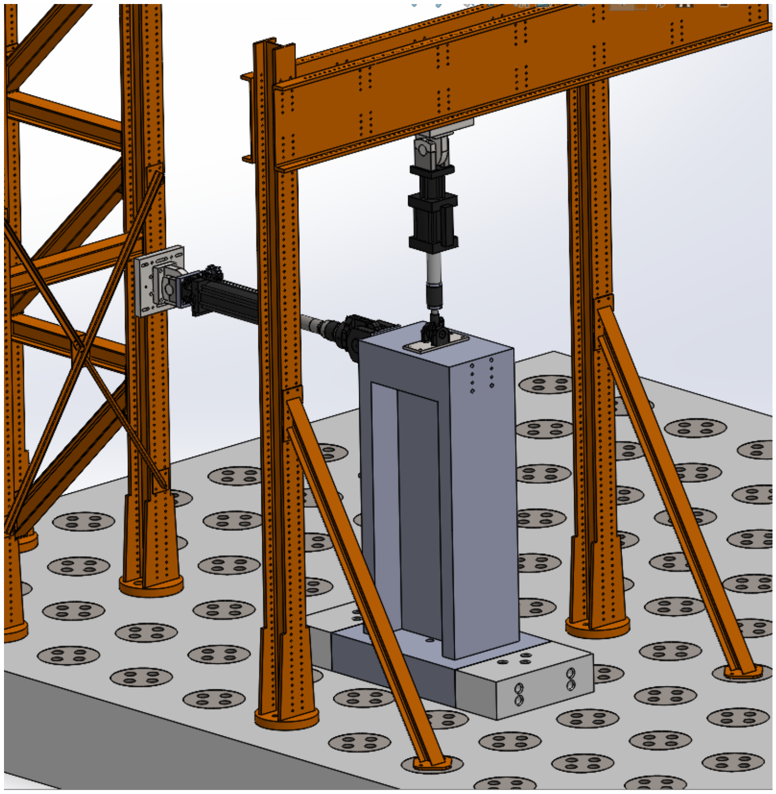

Figure 6.1: 3D view on Solidworks of the specimen in the LEMSC

6.2 Loading protocol

The loading protocol has to reflect the actions that a building wall can endure during a seismic event. The fully-reversed cyclic quasi-static protocol [22] will be applied on the wall thanks to the horizontal actuators (see Figure 6.2). For one amplitude, the cycle is repeated twice. After two repetitions the amplitude increases by $+0{,}25\Delta y$.

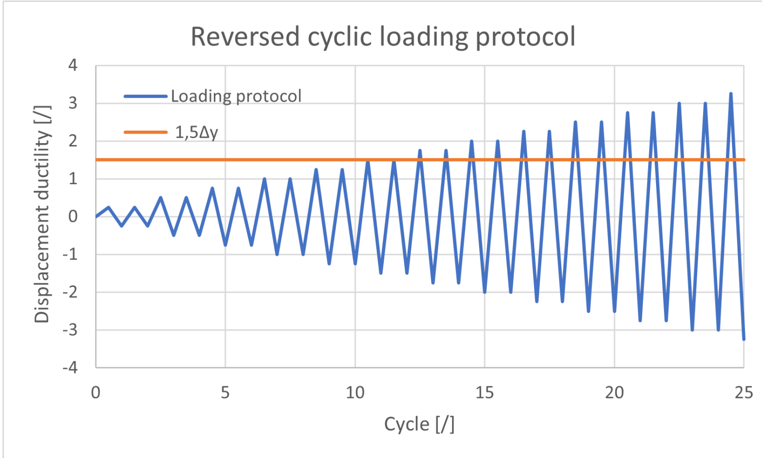

Figure 6.2: Fully-reversed cyclic quasi-static loading protocol.

In order to obtain the value of Δy, a bilinearization of the force-displacement curve [18](obtained with Seismostruct, see Figure 5.8) was computed (see figure 6.3). The "nominal yield" obtained is 0,04m. Therefore the wall is predicted to have a displacement ductility of 1,5Δy, since the ultimate deformation is 0,06mm (1,5= $\frac{0{,}06mm}{0{,}04mm}$). Meaning that, before the first 12 cycles, the wall has not reached its maximal displacement capacity of $1,5\Delta y$.

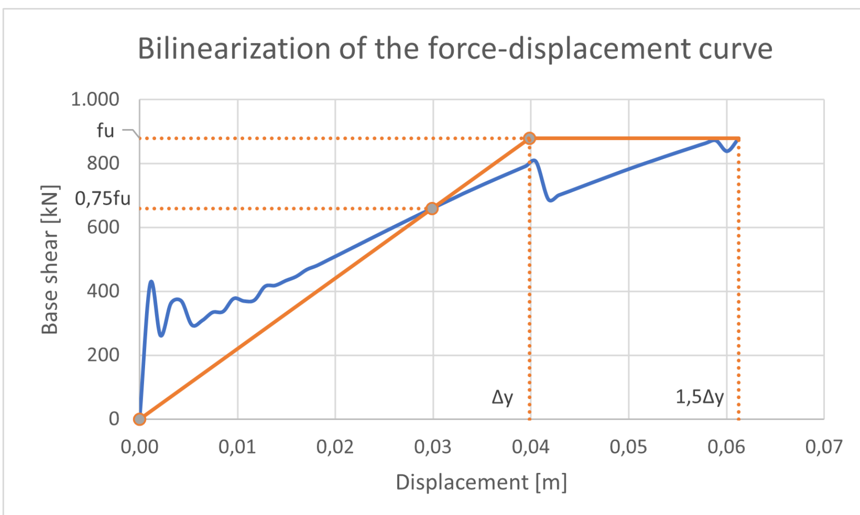

Figure 6.3: Bilinearization of the force-displacement curve obtained in Seismostruct.

6.3 Instrumentation

6.3.1 Digital Image Correlation

Digital Image Correlation (DIC) is a measurement technique that detects displacements, deformations, and even stresses that appear during the test in the structure. The system compares two images taken at a different time of the experiment and determines also the cracks that are not visible [17]. The advantage of this technique is that it has not to be directly in contact with the specimen. Two cameras will be placed on two sides of the wall (see Figure 6.4).

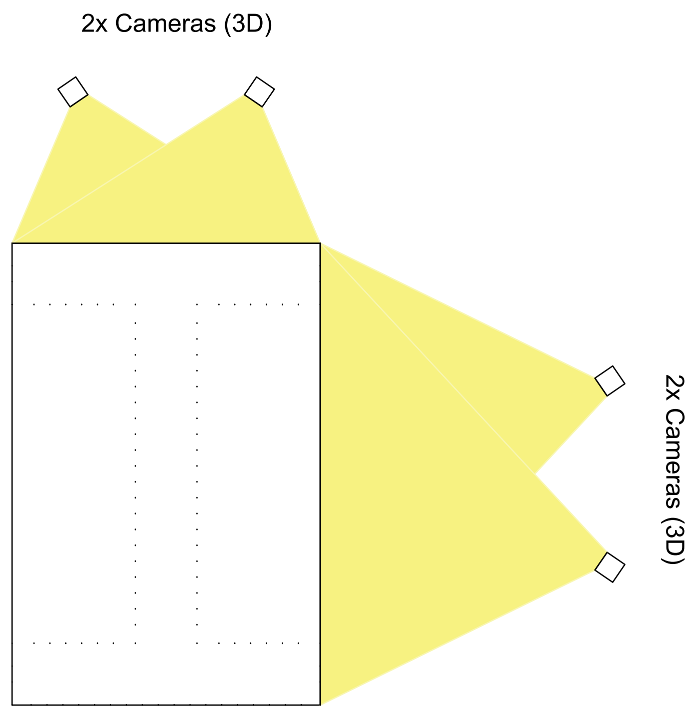

Figure 6.4: Setup of the DIC

6.3.2 Optical Fibers

Distributed Fibre Optic Sensing (DFOS) allows to measure the deformation of an embedded rebar. These measurements permit to confirm design hypotheses or predictions. DFOS are placed directly on the rebars (see Figure 6.5a) and in strategic places, namely, on the longitudinal rebars located at the extreme of the wall (see Figure 6.5b). One rebar at each corner of the flange will be equipped with DFOS because these rebars are likely to undergo the most deformation.

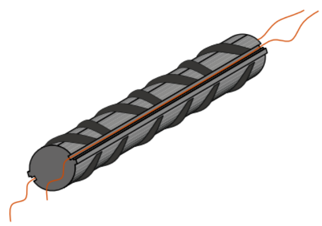

(a) Representation of a DFOS system on steel rebar [10]

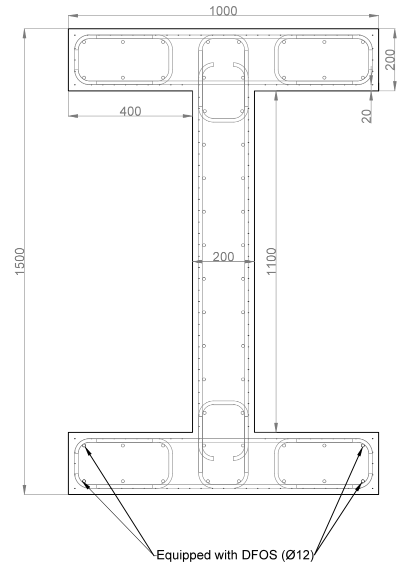

(b) Position of DFOS installed on GFRP's rebars

Figure 6.5: Setup of DFOS

6.3.3 Extensometers

LVDTs

Linear Variable Differential Transformers (LVDTs) transmit information on linear displacements. They are used to determine the extension between two points. The LVDTs will be placed over the full height of the flanges. They will be fixed to the wall with glue to avoid damaging the concrete [22].

Figure 6.6: Exemple of the setup of LVDTs on a concrete wall from a previous test at the LEMSC [22]

Potentiometers

Potentiometers are another type of sensor for linear displacement. There will be four potentiometers placed on the wall, two along the vertical of flanges and two in the diagonal of the web (see Figure 6.7). The two vertical potentiometers will have the same objectives as the LVDTs to still collect data if the last one fails during the test [22].

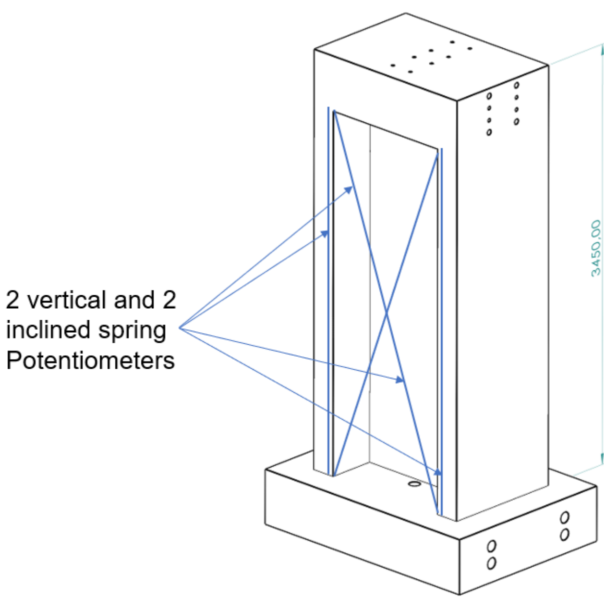

Figure 6.7: Position of the four spring Potentiometers on the wall

6.3.4 Inclinometers

Inclinometers allow to measure the inclination of the specimen in one direction over time. Two sensors will be fixed on the top of the wall, above the flanges. They will be placed in the direction of the bending.

6.3.5 Micrometers

These sensors are located at the base of the wall. Micrometers collect data on small linear deformation. These allow us to quantify the cracks at the base of the wall. Ten sensors will be placed on the center foundation block, at the base of the wall. There will be 2 along each flange (4 in total) and 6 along the web (see Figure 6.8). Micrometers will be placed on the same side of the wall as the potentiometers to facilitate the installation.

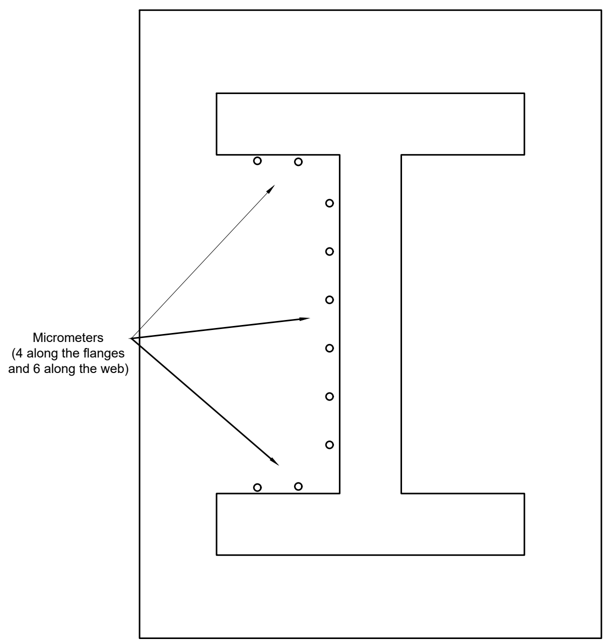

Figure 6.8: Setup of the micrometers on the base of the wall

Chapter 7

Conclusions and Future Developments

7.1 Conclusion

This work aims to conduct an experimental test to enhance the understanding of the seismic behavior of Glass Fiber Reinforced Polymer (GFRP) as reinforcement within a wall. Indeed, the use of GFRP in RC structures offers many advantages, not least the longer service life of the structure. However, GFRP is not yet widely used in the construction industry. One of the reasons for this is a lack of knowledge about its reaction during a seismic event. Hence, conducting experimental tests on this subject is crucial and has the potential to possibly reshape the future of buildings.

In this study, we designed an I-shaped wall reinforced with GFRP, which could represent a scaled model of the central core wall of a building. To achieve this, we employed two design methods: the numerical method and the analytical method. The numerical method primarily involves creating a wall model within a software program (Seismotruct and Response 2000), specifying the structural features and the material properties. Subsequently, the software provides predictions regarding the wall's response under specific loading conditions. Concerning the analytical method, several codes in the literature encompass the design of GFRP. We particularly adhered to the sectional analyses developed by the AFGC and by the next version of Eurocode 2. By following these novel dimensioning expressions, we were able to ascertain the failure mode and the strength of the wall.

These two methods were initially applied to walls that had already been tested, where the displacements and forces on the walls were known. The objective was to compare the results obtained from analytical and numerical methods with the outcomes observed during the experiments. In practice, data from four walls (G10, G12, G15, and GNW) from two different studies (respectively Mohamed & al, 2013 [13] and Zhang & al, 2019 [23]) were used. This approach enabled us to gain confidence in the reliability of our methods.

So far, the literature has predominantly focused on walls with rectangular shapes. This work stands out from prior literature due to the selection of an I-shaped wall. With the assurance of an effective method, the wall's response could be predicted. The challenge now was to ensure that the wall's failure under the load (maximum 1000kN) and displacement (maximum 13cm) conditions were possible during testing. Indeed, in order to observe, understand, and analyze material behavior during an earthquake, reaching the structural failure point is crucial. Therefore, the wall was designed to withstand a force of approximately 930 kN (depending on the prediction methods) and the top displacement would be 6cm.

The failure mode of the wall was also predicted. Due to the I-shaped design of the wall, the concrete area is substantial in the flanges, resulting in significant compressive strength of the concrete. Consequently, the failure is predicted to occur in the GFRP elements. Typically, this brittle failure mode of the reinforcements is often avoided to take advantage of the ductility of concrete. Indeed, in the literature, since tested walls are mainly rectangular this rupture issue does not arise. However, in this case, the mode of rupture in the rebars is imposed by the unique geometry of the wall.

The objective of this study was to formulate a design for a wall in preparation for an upcoming experimental test. This research delves into the suggested approach to effectively conduct this forthcoming experiment. One of the primary challenges lies in determining the optimal position and configuration of the wall within the laboratory (LEMSC). To do so, a Solidworks file was generated to ensure a seamless fit of the wall within the experimental setup. Two actuators, one vertical (for the axial load) and one horizontal (for the moment), will apply forces to the wall. A proposed loading protocol has been developed for the horizontal actuator. Lastly, a recommendation for instrumentation is provided to enable the measurement and collection of all the necessary data, facilitating the subsequent analysis of the results.

7.2 Future developments

This work primarily serves as preparation for an experimental test aimed at analyzing the seismic behavior of GFRP as reinforcement. As such, there is a logical sequence of steps that must be undertaken to achieve this goal.

The setup preparation will need refinement. Some details within the setup have not been fully addressed. For instance, plans for the fabrication of new plates for the feet of the actuators or the assembly of a 35T actuator's head onto a 100T actuator need to be considered. These various subtlety could impede progress in practice. The instrumentation of the wall may also need adjustments if practical issues arise.

Following the completion of this preparatory phase, the wall will have to be fully built and material strength tests will have to be conducted. Subsequently, the wall will have to be positioned within the testing setup and instrumented. Once the testing is completed, the analysis of the collected data could be performed.

More generally, this work represents just an initial stride towards a more comprehensive understanding of the seismic response of GFRP. Numerous types of walls could be investigated, such as U-shaped or L-shaped walls. Additionally, GFRP reinforcements could be incorporated into the foundation to study the seismic behavior of an entirely GFRP-reinforced structure.

Bibliography

[1] Pultrusion Process for Composite Materials.

[2] *FRP reinforcement in RC structures: technical report prepared by a working party of Task Group 9.3 FRP (Fibre Rweinforced Polymer) reinforcement for concrete structures.* Bulletin - FIB. FIB, Lausanne, 2007. OCLC: 454648558.

[3] Seismostruct 2021 User Manual ENG, 2021.

[4] American Concrete Institute. ACI CODE-440.11-22: Building Code Requirements for Structural Concrete Reinforced with Glass Fiber-Reinforced Polymer (GFRP) Bars—Code and Commentary, 2022. Citatio key: ACI.

[5] K. Beyer, A. Dazio, and M. Priestley. Inelastic Wide-Column Models for U-Shaped Reinforced Concrete Walls. *Journal of Earthquake Engineering*, 12, Apr. 2008.

[6] CEN (European Committee for Standardization). Eurocode 2: Design of concrete structures - Part 1-1: General rules and rules for buildings, bridges and civil engineering structures (Working Draft), Oct. 2022.

[7] E. FERRIER, S. Chataigner, L. Michel, K. Benzarti, E. GHORBEL, P. JANDIN, A. PRUVOST, M. Quiertant, A. Rolland, B. BENMOKRANE, Y. FALAISE, A. Feraille, A. Nanni, C. TESSIER, S. BOUTEILLE, T. Desbois, A. JUNES, C. MEYER, J. ROTH, and R. WIRTH. *Utilisation d'armatures composites (à fibres longues et à matrice organique) pour le béton armé*. Jan. 2022.

[8] R. Hoult, A. Correia, and J. Pacheco Almeida. Beam-Truss Models to Simulate the Axial-Flexural-Torsional Performance of RC U-Shaped Wall Buildings. *CivilEng*, 4:292–310, Mar. 2023.

[9] João P. FIRMO, Inês C. ROSA, João R. Correia, Tommaso D'ANTINO, Wallace SOUZA. Fibre-reinforced polymer reinforcement for durable concrete structures. Dec. 2023.

[10] Y. Lemcherreq, T. Galkovski, J. Mata-Falcón, and W. Kaufmann. Application of Distributed Fibre Optical Sensing in Reinforced Concrete Elements Subjected to Monotonic and Cyclic Loading. *Sensors*, 22(5):2023, Jan. 2022. Number: 5 Publisher: Multidisciplinary Digital Publishing Institute.

[11] Y. Lu, M. Panagiotou, and I. Koutromanos. *Three-Dimensional Beam-Truss Model for Reinforced-Concrete Walls and Slabs Subjected to Cyclic Static or Dynamic Loading.* Jan. 2015.

[12] J. B. Mander, M. J. N. Priestley, and R. Park. Theoretical Stress Strain Model for Confined Concrete. *Journal of Structural Engineering*, 114(8):1804–1826, Sept. 1988.

[13] N. Mohamed, A. Farghaly, B. Benmokrane, and K. Neale. Experimental Investigation of Concrete Shear Walls Reinforced with Glass Fiber–Reinforced Bars under Lateral Cyclic Loading. *Journal of Composites for Construction*, May 2013.

[14] N. A. A.-R. Mohamed. Strength and drift capacity of GFRP-reinforced concrete shear walls. 2013. Accepted: 2015-02-23T18:18:42Z Publisher: Université de Sherbrooke.

[15] A. Nanni, A. Luca, and H. Jawaheri Zadeh. *Reinforced Concrete with FRP Bars: Mechanics and Design.* Mar. 2014.

[16] K. Pelletier and P. Léger. Nonlinear seismic modeling of reinforced concrete cores including torsion. *Engineering Structures*, 136:380–392, Apr. 2017.

[17] S. Roux, J. Réthoré, and F. Hild. Digital Image Correlation and Fracture: An Advanced Technique for Estimating Stress Intensity Factors of 2D and 3D Cracks. *Journal of Physics D Applied Physics*, 42, Nov. 2009.

[18] Saraiva Esteves Pacheco De Almeida João. Cours : LGCIV2046 - Earthquake engineering.

[19] S. Singh. *Analysis and Design of FRP Reinforced Concrete Structures.* Jan. 2014.

[20] Sireg. Straight and bent GFRP bars Sireg Glaspree test results according to EAD 260023-00-0301. Technical report, May 2023.

[21] B. Stafford-Smith and A. Girgis. Deficiencies in the Wide Column Analogy for Shearwall Core Analysis. *Concrete international*, Apr. 1986. Citatino key: Stafford.

[22] T. Wyckmans and M. Steinmetz. Conception d'un dispositif expérimental pour des essais cycliques d'unités à grande échelle au LEMSC, 2019.

[23] Q. Zhang, J. Xiao, Q. Liao, and Z. Duan. Structural behavior of seawater sea-sand concrete shear wall reinforced with GFRP bars. *Engineering Structures*, 189:458–470, June 2019.

List of Figures

List of Tables

UNIVERSITÉ CATHOLIQUE DE LOUVAIN
École polytechnique de Louvain
Rue Archimède, 1 bte L6.11.01, 1348 Louvain-la-Neuve, Belgique | **www.uclouvain.be/epl**